MUSE View of the Circumgalactic Medium around a z $\sim$ 4.5 Radio Galaxy

— Das zirkumgalaktische Medium einer hoch rotverschobenen Radiogalaxie mit z $\sim$ 4.5 aus Sicht des MUSE Instruments

Wuji Wang

München 2020

MUSE View of the Circumgalactic Medium around a z $\sim$ 4.5 Radio Galaxy

— Das zirkumgalaktische Medium einer hoch rotverschobenen Radiogalaxie mit z $\sim$ 4.5 aus Sicht des MUSE Instruments

Wuji Wang

Dissertation
an der Fakultät für Physik
der Ludwig–Maximilians–Universität
München

vorgelegt von
Wuji Wang
aus China

München, den May 26th 2020

Erstgutachter: Dr. Benjamin Moster
Zweitgutachter: —
Tag der mündlichen Prüfung: —

Contents

Abstract **xi**

Declaration **xiii**

1 Introduction **1**
1.1 Galaxy and its Evolution 1
1.2 CGM 3
1.3 HzRGs 6
1.3.1 HzRGs in general 6
1.3.2 CGM of HzRGs 6
1.3.3 HzRGs Absorption 8
1.4 HzRGs Sample 9
1.5 4C04.11 10
1.6 Thesis Structure 11

2 Observations and Data Reduction **13**
2.1 MUSE Observation 13
2.2 Data Reduction 13
2.2.1 Pipeline Reduction 14
2.2.2 Cube Creation 14
2.2.3 Self-Calibration Check 16
2.2.4 Performance Comparison 17
2.2.5 Astrometry Correction 19

3 Spectrum Extraction and Line Fitting **23**
3.1 Spectrum Extraction 23
3.2 Emission Line Fitting 23
3.2.1 Fitting Procedure 23
3.2.2 HeII 27
3.2.3 Lyα 31

4 Spatial Mapping **37**
4.1 Spatial Tessellation 37

4.1.1 Voronoi Bin 37
4.1.2 Swinbank et al. (2015) Tessellation 38
4.2 Fitting Procedure 39
4.3 Mapping Results 40
4.4 Interpretation 42

5 Summary and Outlook **45**
5.1 Summary 45
5.2 Outlook 46

A Individual Exposure Correction **47**

B Zoom-in Comparison **57**

Danksagung **78**

List of Figures

1.1 SFRD Evolves with Redshift 2
1.2 Galaxy Luminosity Function with Feedback 3
1.3 CGM 5
1.4 Absorption Maps in Swinbank et al. (2015) 7
1.5 MUSE Lyα halos of sample HzRGs 10

2.1 Auto Calibrations Check 20
2.2 Spectra Performance Comparison 21

3.1 Spectrum Extraction Region 24
3.2 Full MUSE Spectra 25
3.3 Best HeII Fitting Result 27
3.4 Corner Plot of HeII Line Fitting 28
3.5 Lyα Gaussian Fit & First Four Absorber Fit 30
3.6 Best Lyα Fitting Result 33
3.7 N_H - b Degeneracy Check 35

4.1 Tessellation Map 38
4.2 Spatial Morphology and Dynamic 41
4.3 N_H and Δv Maps for Absorber 1 and 2 42
4.4 N_H and Δv Maps for Absorber 3 and 4 43
4.5 N_H Maps for Absorber 5, 6, 7 and 8 44

A.1 AUTOCAL_FACTORS in Exposure 1 48
A.2 AUTOCAL_FACTORS in Exposure 2 49
A.3 AUTOCAL_FACTORS in Exposure 3 50
A.4 AUTOCAL_FACTORS in Exposure 4 51
A.5 AUTOCAL_FACTORS in Exposure 5 52
A.6 AUTOCAL_FACTORS in Exposure 6 53
A.7 AUTOCAL_FACTORS in Exposure 7 54
A.8 AUTOCAL_FACTORS in Exposure 8 55

B.1 Spectra Comparison in Band 1 59
B.2 Spectra Comparison in Band 2 60

B.3 Spectra Comparison in Band 3 61
B.4 Spectra Comparison in Band 4 62
B.5 S/N Comparison in Band 1 63
B.6 S/N Comparison in Band 2 64
B.7 S/N Comparison in Band 3 65
B.8 S/N Comparison in Band 4 66
B.9 Three Spectra Comparison in Band 1 67
B.10 Three Spectra Comparison in Band 2 68
B.11 Three Spectra Comparison in Band 3 68
B.12 Three Spectra Comparison in Band 4 69
B.13 Two Spectra Comparison in Band 1 69
B.14 Two Spectra Comparison in Band 2 70
B.15 Two Spectra Comparison in Band 3 70
B.16 Two Spectra Comparison in Band 4 71

List of Tables

2.1 Data Cube Differences 15
2.2 Quantitative S/N Check 18

3.1 Emission Fitting Results 29
3.2 Lyα Fit Constraints 31
3.3 Lyα Absorption Fitting Results 32

Abstract

High-redshift radio galaxies (HzRGs, $L_{500\,\mathrm{MHz}} > 10^{26}$ W Hz^{-1} and z > 2) are hosted by some of the most massive galaxies at any redshift with $M_* > 10^{11} M_\odot$ and are known to reside in overdense (proto-cluster) environments. Given the correlation between the stellar bulge mass and the black hole mass, it is no surprise that the central black holes in HzRGs are supermassive and can power extreme active galactic nuclear (AGN) activity. The observed powerful radio jets and the inferred high star formation and black hole accretion rates show that the extended gaseous environment of HzRGs are actively disturbed by the outflows and inflows. They are basically the only objects in which quasar mode feedback, radio mode feedback AND the host galaxy can be studied simultaneously making them ideal laboratories for providing us with crucial insights into the formation and early evolution of the most massive early-type galaxies in the Universe at (or near) Cosmic Noon (z $\sim$ 3).

Through a combination of matched resolution optical and submm 3D spectroscopy tracing the three different gas phases (neutral, ionized and molecular), a better understanding of these complex physical processes can be tried to be achieved. Our eight sampled HzRGs ($2.9 < z < 4.5$) observed with both ALMA and VLT/MUSE will be used to fulfill this goal.

In this pilot study, we focus on the MUSE observations of one target, 4C04.11, to study the emission and absorption gaseous properties of its circumgalactic medium (CGM). We develop an optimized data reduction procedure through testing different reduction parameters and spectra comparing which can be adopted to following sample objects. We determine the systemic redshift, 4.5079$\pm$0.0001, by fitting the brightest non-resonant line HeII. We identify a narrow and a broad emission components along with eight absorbers through aperture extracted Lyα spectrum fitting using Voigt profile overlapped with two Gaussians. The column densities lie within the range $14.6 - 15.9$ log(N/cm^{-2}). We construct the moment maps of Lyα line based on individual fitting of spatially tessellated signal-to-noise improved target region to study the kinematics and distributions of the emission gas. Preliminary column density maps of absorbers are also obtained to investigate their spatial distribution in which a density gradient of the absorber at v $\sim$ 0 km s^{-1} is seen.

The overall goal is to perform a thorough study of the CGM of HzRGs using MUSE

and ALMA observations with this thesis work as a preliminary exploration. For future procedures, the CIV lines will be examined to study the CGM enrichment and physical properties behind the metal element while ALMA data will be applied to explore the molecular and atomic gas subsequently.

Declaration

Declaration:

I hereby declare that this thesis is my own work, and that I have not used any sources and aids other than those stated in the thesis.

München, May 26th 2020

Author's signature

Chapter 1

Introduction

1.1 Galaxy and its Evolution

Galaxies which consist of stars, gas, dust, black holes and dark matter are gravitationally bound systems serving as building blocks of the Universe. A typical galaxy, like our Milky Way Galaxy, has ten billion stars and a diameter of $\sim$ 30 kpc. Although the number of stars living in a galaxy is enormous, it is commonly believed that galaxies are more fundamental ingredients than stars. Their evolution is accompanied by matter/energy exchange with the surrounding medium and produces the present Universe we observe and the environment we live (Milky Way Galaxy). Hence, it is not surprising that the investigation of galaxy formation and evolution is one of the most attractive field in modern astrophysics.

In the popular cosmology model, ΛCDM (cold dark matter), the Universe consists of dark energy ($\sim$75%), dark matter ($\sim$21%) and remaining baryonic matter which forms the observable objects. In galaxies, the baryonic matter forming stars, gas and dust only accounts for 10%, while most of the galaxy mass is made up of dark matter (See Mo et al., 2010, and references therein) which should be taken into serious consideration in studying the theory of galaxies. According to their morphology, galaxies can be (loosely) categorized into ellipticals (early-type), spirals (late-type) and others (e.g. irregulars). The study of galaxy structure evolution (e.g. Conselice, 2014) is an important part in completing the galaxy evolution theory. Evidence shows that compared to spirals the elliptical galaxies are more often found in clusters or alternatively, surrounded by clusters. Some of the most massive elliptical galaxies may be have been powerful radio galaxies at high-redshift, namely high-redshift radio galaxies, the objects we focus on in this work (Section 1.3).

In the theory of galaxy formation, the initial dark matter and gas collapse due to gravitational instability to form structures. The gas then goes through cooling processes causing further accumulation to form a proto-galaxy. This is the simplest idea behind galaxy formation whose details are far from complete. After the initial formation, galaxies are evolving accompanied by star formation and growth of the central super massive

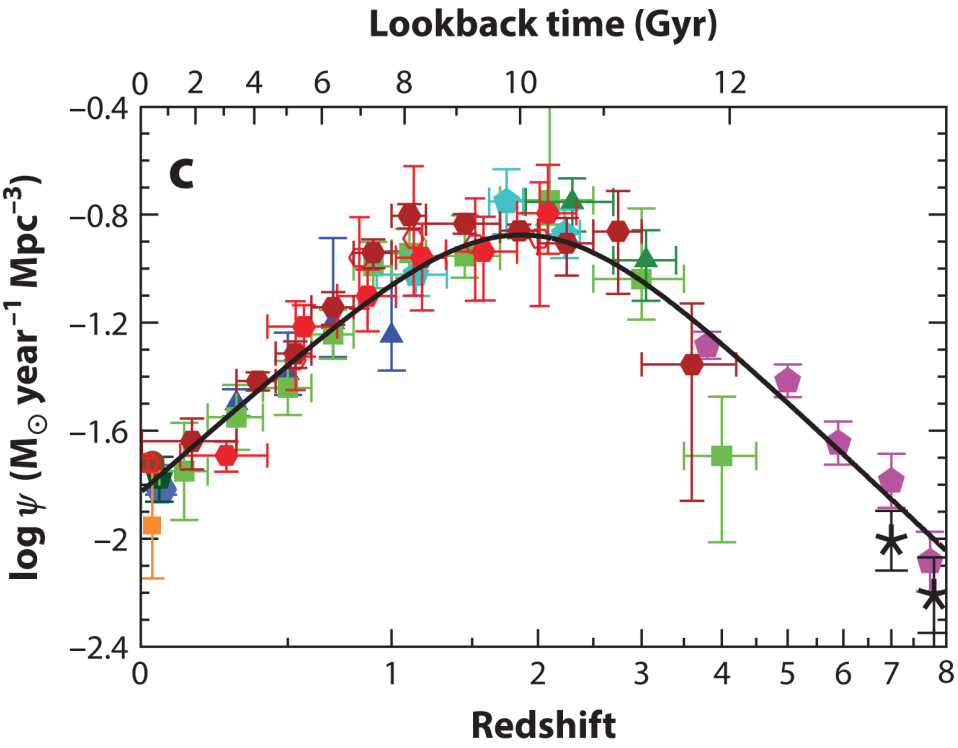

Figure 1.1: The evolution of star formation rate density ($\phi(z)$, which indicates the star formation rate in a given volume at a specific time) with redshift or look-back time. This figure is adapted from Madau & Dickinson (2014).

black hole (SMBH) through accretion of surrounding gas. The current evidence indicates that the SMBH co-evolves with its host galaxy (See Kormendy & Ho, 2013, and references therein) showing in relation found between $M_\bullet$ and M_{bulge} and similar evolution trends of black hole accretion rate and star formation rate density (SFRD) with redshift (See Figure 1.1). Besides, the discovered relations of $M_\bullet - L_{bulge}$ and $M_\bullet - \sigma$, where σ is the velocity dispersion of the stars (Kormendy & Ho, 2013), stress the co-evolution. However, these relations are more dispersed in active galaxies than "normal" galaxies which implies that the actively accreting SMBH (active galactic nulceus: AGN) may play an important role in regulating the co-evolution.

The regulation mechanisms are believed to be in the form of feedback (stellar or/and AGN) which has an impact on the matter/energy of the galaxy and is important to reproduce the current galaxy luminosity function (Figure 1.2). The AGN feedback which is focused in this work can be taken in many modes, e.g. outflow through winds and radio jets. These activities are believed to be effective in exchanging energy and matter between the host galaxy and its environment and regulating the host evolution (positive and negative). The objects in which we can basically study both radio-mode and quasar-mode feedback are high-redshift radio galaxies (Section 1.3) which is the motivation of this thesis

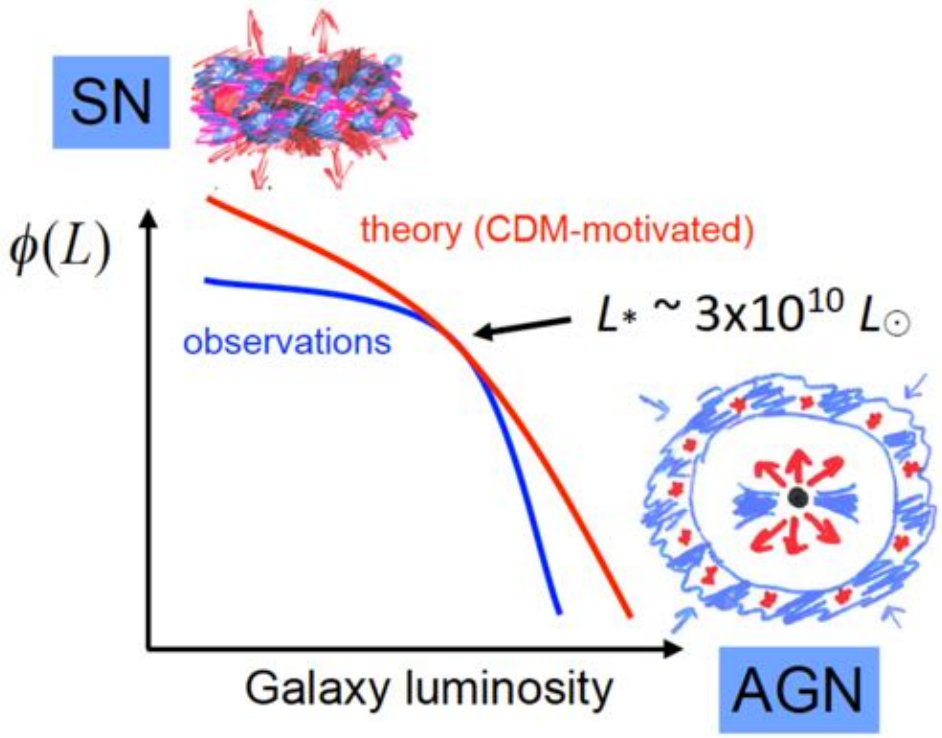

Figure 1.2: This schematic figure adopted from Silk & Mamon (2012) shows the impact of (supernovae and AGN) feedback mechanism on reproducing the observed galaxy luminosity function (blue). The current cosmological simulation without feedback (red) will overproduce both the number of bright (big) and faint (small) galaxies.

work.

1.2 Circumgalactic Medium

The gravitationally bounded gaseous halos beyond the interstellar medium (ISM) scope (10-20 kpc) of galaxies are known as Circumgalactic Medium (CGM) which can reach hundreds of kpc from the galactic nuclei. Further than the range of the CGM, it is the tens of Mpc scale intergalactic medium (IGM): the space between groups of galaxies. Hence, the CGM acts as a bridge which links the gas from IGM and ISM. Due to the upgrade of observational techniques and development of simulation methods, the understanding of CGM has been increasing over the recent decades. It is now believed to be the venue of complex gas motions (see Figure 1.3) regulating galaxy formation and evolution which makes it an essential component of galaxies (see Tumlinson et al., 2017, for further review). The CGM is particularly interesting for studying feedback processes especially at high redshift, since both gas accretion from the cosmic web and feedback from the galaxy can be probed

together giving insights into how galaxies built up in the early Universe.

The detection of CGM is preferentially through absorption: (i) absorption against bright background sources (e.g. Rubin et al., 2015; Bowen et al., 2016); (ii) stacking of massive faint spectra from large survey (e.g. Steidel et al., 2010; Peek et al., 2015); (iii) use the galaxy's own emission as background source (e.g. Cantalupo et al., 2014; Heckman et al., 2015). Some of the halos have been detected in emission through X-ray Observatory (e.g. $XMM-Newton$ Anderson et al., 2016). Though in low surface brightness, during the past 30 years, more works have been done in observations for the CGM around AGN focusing on their Lyα or other UV emission lines (e.g. NV, CIV) using narrow-band image, long-slit spectroscopy and integral field spectrographs (e.g. Heckman et al., 1991a,b; Reuland et al., 2003, 2007; Gullberg et al., 2016a; Vernet et al., 2017). It is reported in Wisotzki et al. (2018) that emission from the circumgalactic atomic hydrogen has been discovered to a large amount and the extended Lyα nebulae have a sky coverage close to unity. The CGM gas in molecular phase surrounding high-redshift radio galaxies (HzRGs, see Section 1.3) has also been reported (e.g. Gullberg et al., 2016b; Emonts et al., 2016, 2018). Recent work of Burchett et al. (2020) using KCWI/Keck data shows that the study of CGM can also be done through observation of MgIIλ2796,2803 Å and FeII/FeII$^*\lambda$ 2586, 2600, 2612, 2626, 2632 Å multiplet lines other than the aforementioned Lyα, CIV and HeII. These observations reveal that the scale of CGM gas is extended and it is in multi-phases of ionization states and complex kinematics.

In Figure 1.3, different gas components and motions in CGM is shown clearly: (i) the cold gas accteted to the central galaxy from IGM (blue); (ii) The gas outflows dreiven by star formation and/or AGN feedback (orange); (iii) gas which has $v < v_{esc}$ (escape velocity of the gravitational potential of the galaxy) is recycled back into the ISM of the galaxy (pink); (iv) surrounding diffused large scale lower surface luminosity gas (purple).

Gas accretion and feedback through inflows and outflows regulate galaxy formation and evolution. The cold gas is accreted from large scale IGM through CGM into ISM to fuel the star formation in the galaxy. This process has been predicted and tested in numerical and observational works(e.g. Bond et al., 1996; Umehata et al., 2019). The feedback mechanism can, in theory, have negative effects on the galaxy star formation through cosmic time. These processes may result in the observed relation between star formation rate density and redshift (Madau & Dickinson, 2014) and the bimodal classification of galaxies (Schiminovich et al., 2010) in terms of stellar mass (M_*) and specific star formation rate (sSFR) seen today. But more works needed to be done before we can relate the proposed explanation to observations.

The other two interesting questions related to the study of CGM are:

- **"Missing baryons" :** In observations, the baryon mass contained in stars and ISM of galaxies are much lower than the fraction of halos predicted by ΛCDM model,

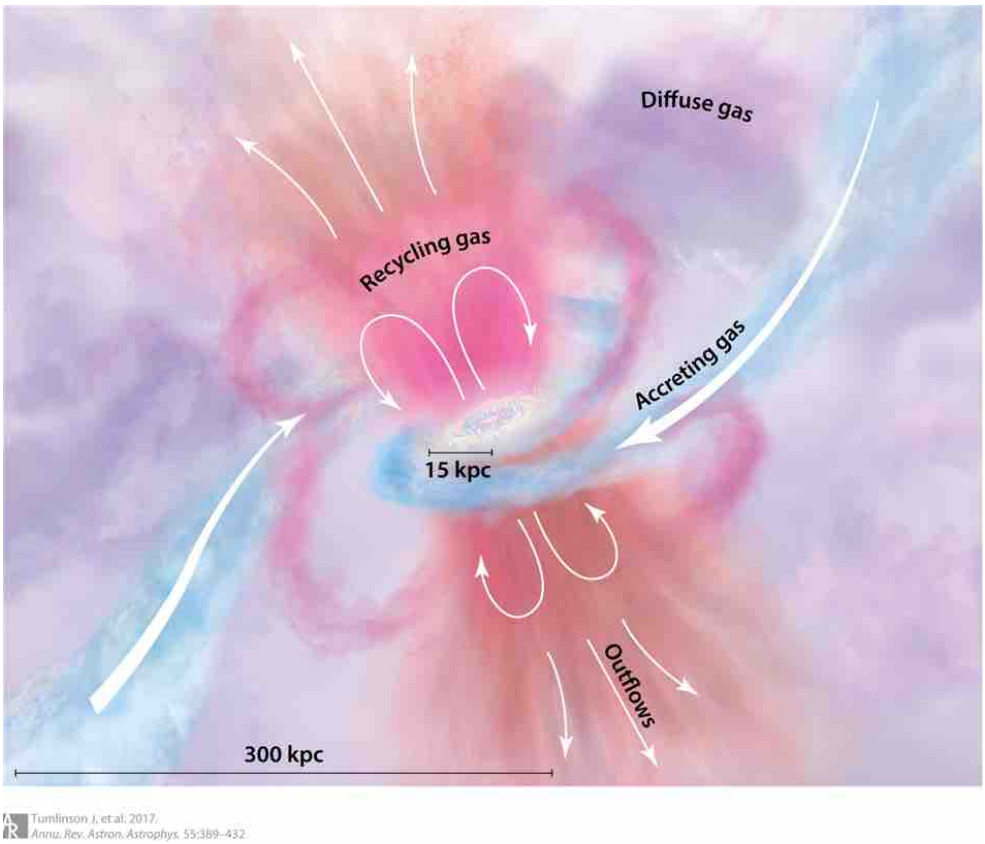

Figure 1.3: An artist's view showing the CGM and motions of gas embedded in it. This figure is adapted from Tumlinson et al. (2017).

with $M_b \ll (\Omega_b/\Omega_m)M_h$, where M_b is the total baryon mass and M_h being the halo mass (e.g. Behroozi et al., 2010). There are several hypothesis which may explain the inconsistency (Tumlinson et al., 2017). All of these suggest that CGM will be a key part in understanding this problem.

- **Metal loss:** The metal elements are produced mainly through the star formation process within the galaxies. They may leave the galaxy through outflows or recycle into the CGM and back to ISM (Figure 1.3). The mysteries are still unclear how to scale the outflow with galaxy mass and how to produce a flat metal fraction over 3 decades in stellar mass (Peeples et al., 2014). Through the study of CGM metallicity, we may obtain an answer to these questions.

The concept of CGM did not catch the attention of the astronomical community until recently. It will be an important puzzle of understanding the process of galaxy formation and evolution. Given the fact that the the CGM surrounding the HzRGs (See Section 1.3) can be studied into details, it will provide us a remarkable laboratory to address the aforementioned questions.

1.3 High-redshift radio galaxies

1.3.1 HzRGs in general

The mark of the beginning of this field (high-redshift radio galaxies) is the work of Minkowski (1960) done with 3C295. Since then, many radio surveys in 1980s and 1990s have successfully discovered a number of radio galaxies, and new efficient finding techniques have been implemented since the mid 1990s. Thanks to all the efforts, now we have a wonderful sample of radio galaxies to study their formation and evolution (see McCarthy, 1993; Miley & De Breuck, 2008, for further review). The radio morphological properties have been studied since the beginning (e.g. Miley, 1980). With the upgraded observational techniques, multi-wavelength properties are feasible. When looking back through cosmic time into the younger Universe ($z > 2$), the different components of radio galaxies (gas, dust, stars, quasars and black holes) and processes manipulating the galaxy evolution and formation (e.g. AGN feedback and star formation) revealed by various observations will offer us marvelous opportunity to study these galaxies and larger scale formation and evolution with on-going details.

High-redshift Radio Galaxies (HzRGs, $L_{500MHz} > 10^{26}$ W Hz^{-1} and $z > 2$) are hosted by some of the most massive galaxies at any redshift with $M_* > 10^{11} M_\odot$ and are known to reside in overdense (protocluster) environments (De Breuck et al., 2002, 2010; Miley & De Breuck, 2008; Wylezalek et al., 2013). Given the correlation between the stellar bulge mass and the black hole mass (e.g. Kormendy & Ho, 2013), it is no surprise that the central black holes in HzRGs are supermassive and can power extreme AGN activity. There is believed to be a hidden quasar (Type II AGN) hosted by the HzRG behind the gas and dust (Vernet et al., 2001). Many HzRGs are surrounded large extended gaseous halos (e.g. Van Ojik et al., 1997; Cantalupo et al., 2014; Gullberg et al., 2016a; Vernet et al., 2017). The observed powerful radio jets and the inferred high star formation (Drouart et al., 2014) and black hole accretion rates show that the extended gaseous environment of HzRGs are actively disturbed by the outflows and inflows (Section 1.2, Nesvadba et al., 2006; Humphrey et al., 2007; Vernet et al., 2017). They are basically the only objects where we can study quasar mode feedback, radio mode feedback AND the host galaxy all together which make HzRGs being ideal laboratories providing us with crucial insights into the formation and early evolution of the most massive early-type galaxies in the Universe at (or near) Cosmic Noon of stellar mass assembly and SMBH growth ($z \sim 3$).

1.3.2 CGM of HzRGs

The giant gaseous halos associated with HzRGs are often reaching out to several 100 kpc from the nucleus, well into the CGM (see Section 1.2). The halos are observed in all strong emission lines from Lyα to Hα (McCarthy, 1993) and they are metal-enriched, often detected in Nvλ1240 (NV hereafter) and CIV$\lambda\lambda$15481551 lines (CIV hereafter). Molecular

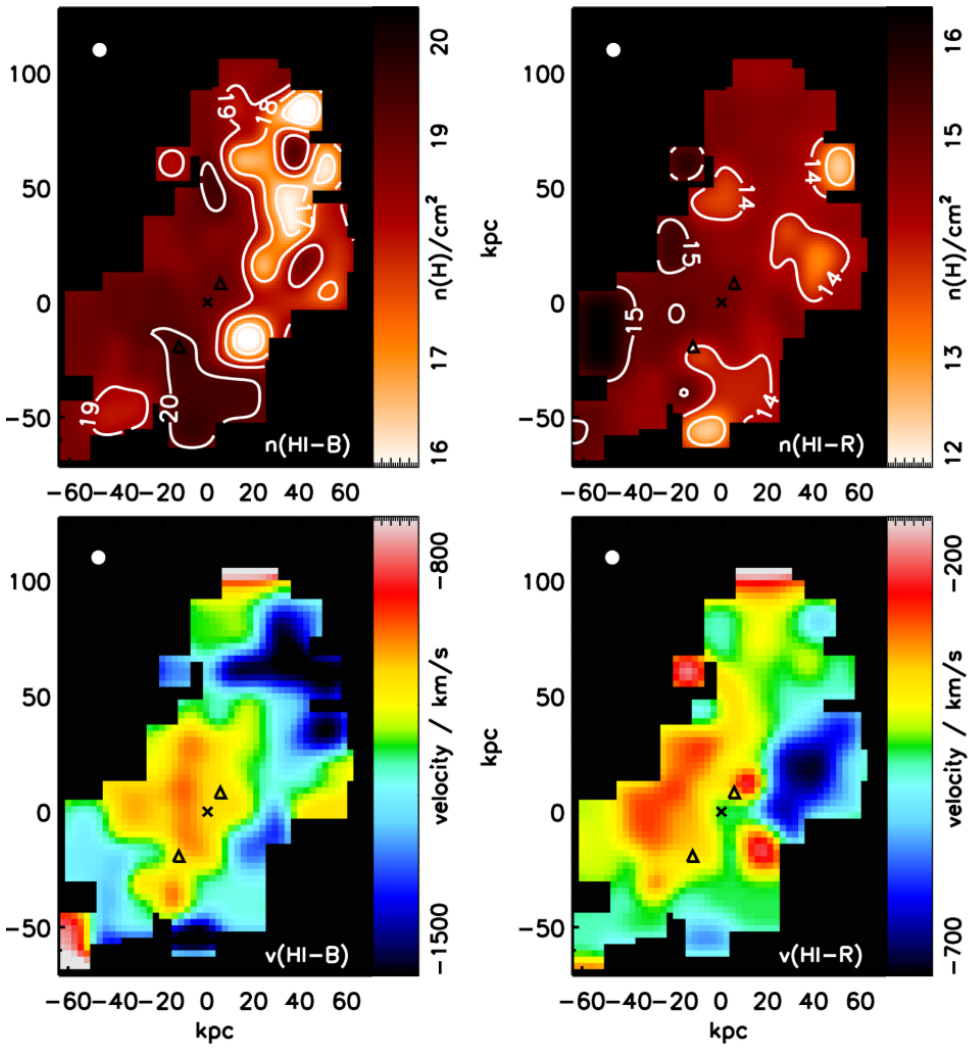

Figure 1.4: The column density (top row) and velocity (bottom row) maps of two absorber (blue and red) identified in TN J1338-1942 from Swinbank et al. (2015) observed with MUSE.

gas emission like [CI] and CO(1-0) have also been observed in the CGM of HzRGs (Emonts et al., 2016; Gullberg et al., 2016b) showing that it is composed of multi-phases. These results show an indication that the in-situ star-formation could be fueled by the molecular gas and provide evidence that the CGM is enriched in metallicity. Within the extent of the radio jets, this gas is strongly disturbed ($\Delta V > 1000$ km s^{-1}), while beyond, more quiescent gas ($\Delta V < 100$ km s^{-1}) is also observed, which links directly to the CGM. Two distinct components of the halos have been identified: (i) the obscured quasar ionized extended emission line region (EELR) (Vernet et al., 2001; Villar-Martín et al., 2003; Humphrey et al., 2006) with high surface brightness in which disturbed gas properties (velocity dispersion $>$ 1000 km s^{-1}) are observed, suggesting strong jet-gas interactions; and (ii) an

extended low surface brightness region with sizes well beyond the radio structures and quiescent gas kinematics (velocity dispersion of a few 100s km s^{-1}, Van Ojik et al., 1997; Sánchez & Humphrey, 2009). The ionization mechanisms behind the emission lines are complicated: photon-ionization by AGN, star formation and jet shock ionization all could be the possible solution(s) (e.g. De Breuck et al., 2000; Vernet et al., 2001; Villar-Martín et al., 2007; Binette et al., 2006; Humphrey et al., 2008a). More effort need to be done on the origin of the ionised photons.

Apart from the evident outflow in the CGM, some works has shown the hints of gas infalling. Humphrey et al. (2007) suggest that the quiescent gas in their sampled HzRGs may be the inflow through CGM to the galaxy. Using the observation of Multi-Unit Spectroscopic Explorer (MUSE, Bacon et al., 2010), the giant gaseous filaments inflow in the CGM has been detected around quasars and HzRGs (e.g. Arrigoni Battaia et al., 2018; Vernet et al., 2017). A remarkable work by Umehata et al. (2019) has mapped the filament gas in three-dimension on Mpc scale of a $z \sim 3.09$ protocluster which provides the evidence supporting the idea of inflow from cosmic web which fuels the star formation and black hole growth. Besides the numerous observations, cosmological hydrodynamic simulations have been done to predict the recycling inflow of previous ejected gas (e.g. Oppenheimer et al., 2010, 2018). Hence the question remains and more research needs to be done to address whether the observed inflows origin from larger scale IGM or it is the recycled gas (See Section 1.2).

1.3.3 Absorption in HzRGs

Lyα halos illuminated by an intense ionizing radiation field are common in the high-z universe (Wisotzki et al., 2018) and have been frequently observed around luminous quasar populations (Arrigoni Battaia et al., 2019). However, unlike Type I AGN, almost every radio-loud type II AGN (= HzRGs) has deep extended absorbers associated with it, possibly because of the strong ionizing radiation when looking directly inside the AGN ionization cone of Type I AGN. These associated absorbers are spatially extended (several tens of kpc) and offer a unique opportunity for probing the neutral CGM, without the requirement of direct ionization by the central AGN (e.g. Van Ojik et al., 1997; Vernet et al., 2001). In addition to the HI absorbers, absorption features have also been identified in CIV and NV (in some cases the Si absorbers have been identified), suggesting that the absorbing material is metal-enriched , and at least some part of it is highly ionized (e.g. Humphrey et al., 2008b; Kolwa et al., 2019).

The absorption has been studied since 1990s (e.g. Rottgering et al., 1995), and some conclusions have been drawn. Van Ojik et al. (1997) reports an correlation between the radio size and the HI absorber which may shed light on the idea that the absorbing gas is confined within the radio jet region. However, Binette et al. (2000) suggests that the metal absorber may be located in a further out shell through its studying of the famous HzRG,

MRC 0943-242. Using high resolution spectroscopy observations, Jarvis et al. (2003) and Wilman et al. (2004) present the HI absorber column density distribution ($> 10^{18}\mathrm{cm}^{-2}$ and $10^{13} - 10^{15}\mathrm{cm}^{-2}$), suggest their possible origins and offer explanations for the metallicity difference seen in the sample. The absorbers associated with the HzRG are often found to be blueshifted to its systemic redshift (Jarvis et al., 2003; Humphrey et al., 2008b). Humphrey et al. (2008b) consider the blueshifted extended absorbers are associated with galactic outflow. Later in Humphrey et al. (2013b), the authors suggest that the nature of the blueshifted absorbers is that they are a relic of powerful feedback events that took place *before* the current phase of HzRG activity began, since the absorbers are quite often substantially larger than the maximum observed extent of the radio source. Swinbank et al. (2015) use the potential of integral field spectrograph (IFS), MUSE, and map the spatial distribution of the HI absorbers in TN J1338-1942 (See Figure 1.4). This indicates an outflow which could be driven by AGN and/or star formation. In a few cases, the more interesting redshifted absorbing features are seen (Jarvis et al., 2003; Kolwa et al., 2019) potentially probing infalling gas accreted from the CGM feeding the central galaxy.

Besides the kinematic study, there are several works which model the ionization and abundances of such absorbers. Binette et al. (2006) explore the photon-ionization process and proposes that the stellar emission could be the possible ionization source of absorber shell. In studying the target – MRC 0943-242, Gullberg et al. (2016a) and Silva et al. (2018) constraint the spatial range and column density of the CIV absorber which is also seen in HI, while Kolwa et al. (2019) implies the AGN radiation is sufficient to produce the CIV and NV column density in the radio galaxy by using photon-ionization model. Humphrey et al. (2013a) study the metallicity and gas infalling rate of the radio-loud quasar TXS 1436+157 (z = 2.54) and discuss the physical mechanisms behind (e.g. starburst-driven superbubbles).

With the IFS as a tool in thesis work, we can move a step forward in studying the neutral CGM of HzRGs with the ability to explore its distribution and kinematics spatially (similar to Swinbank et al., 2015). These absorbers clearly hold important information about the transfer of gas between the HzRG host galaxy and the CGM, including the expulsion of enriched material by feedback activity, and the infall of gas from the CGM making them interesting targets and important parts in studying HzRGs.

1.4 Sampled HzRGs with MUSE observations

In this work, we use a sample of eight HzRGs with MUSE observations with about 4-hour exposure each (See Figure 1.5). This Project (ID: 096.B-0752, PI: J. Vernet) was operated during European Southern Observatory (ESO) telescope run Period 96 from October 2015 to March 2016. The intention of this project is to:

- Map the extended absorption

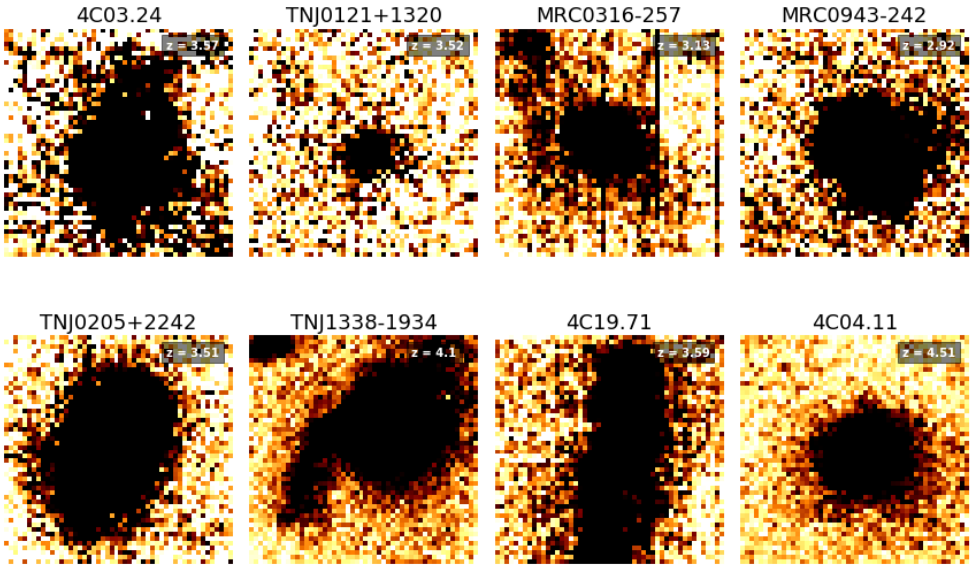

Figure 1.5: The MUSE narrow band images of sampled HzRGs showing their extended Lyα halos. Each side of the narrow band image corresponds to 10 arcsec $\sim$ 74 kpc.

- Map the extended quiescent halo
- Constrain the metallicity and ionization level of the gas
- Study the kinematics of the extended quiescent halo

Our sampled HzRGs with MUSE (as well as ALMA and archived Spitzer) data are perfect targets to study the AGN feedback mechanism at the epoch where the bulk of the stars in the most luminous elliptical galaxies are formed, z = 3 − 5. The feedback is believed to be an important part which prevents the run-away cooling of gas in massive galaxies halos and so match the luminosity function at z = 0. The halos might be the smoking gun of this effect, and the MUSE data will be a key part to study it.

1.5 4C04.11

In this thesis work, we focus on the radio galaxy which has the highest redshift in our sample. Being a bright object at low radio frequency, 4C04.11 was first discovered by Mills et al. (1958) at 85 MHz then confirmed by the large Cambridge interferometer in 178 MHz and registered in the 4C catalogue (Gower et al., 1967). In the early stages of "Big Trio" survey, the radio source closest to 4CO4.11, RC J0311+0507, was observed to have an ultrasteep spectrum (USS, $\alpha = -1.31$, S $\propto \nu^{\alpha}$) between 365 and 4850 MHz using the 600-m diameter ring antenna of the Russian Academy of Sciences (RATAN-600) as the finding survey instrument, the US Very Large Array (VLA) as the imaging instrument, and the Russian 6-m optical telescope (BTA) for photometry and spectroscopy (Goss et al., 1992; Parijskij et al., 1996, 2000). Using the spectroscopic data, Kopylov et al. (2006) report the redshift of RC J0311+0507 is 4.514 by studying its Lyα emission line.

Later on, Parijskij et al. (2013, 2014) use high resolution radio interferometer observations with Multi-Element-Radio-Link-Interferometer-Network (MERLIN) and European Very Long Baseline Interferometer Network (e-EVN) together with multi-band optical and near infrared data and confirm that the source is a FR II (Fanaroff & Riley, 1974) radio galaxy with a central SMBH of mass $\sim 10^9$ $M_\odot$.

1.6 Thesis Structure

In this thesis work, we report the reduction and analysis of the MUSE observation of 4C04.11. The thesis will be structured as: In Chapter 2, the observations and details of data reductions will be discussed including encountered problems. In Chapter 3, the analysis of the MUSE 1D spectrum will be reported, namely line fitting. The spatial analysis which fulfills the merit of MUSE is shown in Chapter 4. Finally, we will summarize this thesis in Chapter 5.
Throughout this work, we use a flat ΛCDM cosmology model with $H_0 = 71$ km s^{-1} Mpc^{-1}, $\Omega_m = 0.27$. At the redshift of our target, 4.5079, 1 arcsec is corresponding to be 6.731 kpc.

Chapter 2

Observations and Data Reduction

In this Chapter, details of the observations and the data reduction are elaborated. An optimized procedure for performing MUSE data reduction is developed based on one target analysis which can be adapted to other sampled objects.

2.1 MUSE Observation

Our target, 4C04.11, was observed by ESO Very Large Telescope (VLT) using the instrument, MUSE (Multi-Unit Spectroscopic Explorer), from December 2nd to 15th 2015 under the program run 096.B-0752(F) (PI:Vernet). The observations were divided into 4 observing blocks (OB) where each OB had two exposures of about 30 minutes each. The total integrated time is 4 hours on target. This was carried out in the extended wide-field mode of MUSE without the correction from active adaptive optics (WFM-NOAO-E). The wavelength coverage of MUSE is 4650 - 9300 Å and the field of view (FOV) of 60×60 arcsec^2 with a 0.2×0.2 arcsec^2 spatial sampling and a 1.25 Å wavelength sampling. The spectral resolving power of MUSE is approximately $\lambda/\Delta\lambda = 1700-3400$ which is $\Delta\lambda = 2.82-2.74$ Å or $\Delta v = 180 - 90$ km s^{-1} (blue to red) in terms of resolution (Bacon et al., 2014). The observations were done with seeing around 1.3 arcsec.

2.2 Data Reduction

We explore different data reduction strategies in order to find an optimized method for further analysis. First, we use MUSE Data Reduction Software[1] (MUSE DRS, version 2.6) pipeline (Weilbacher et al., 2012, 2014, 2016) by running EsoRex (a command-line tool can be used for executing VLT/VLTI instrument pipeline) for calibration creation, observation pre-processing and observation post-processing (See Section 2.2.1). These three reduction stages are completed in the same default procedures before we adjusting the reduction,

[1]latest manual:https://www.eso.org/sci/facilities/paranal/instruments/muse/doc.html

namely combining all exposures whether using MUSE DRS pipeline (pipeline) or MUSE Python Data Analysis Framework (MPDAF), doing sky subtraction with pipeline or not (See Section 2.2.2).

2.2.1 Pipeline Reduction

In this subsection, we simply summarize the data reduction procedure accomplished by MUSE DRS. The first step of (image/spectra) reduction is to produce the required calibration data. In this step, bias, flat and dark fields are generated by using raw calibration data obtained along observation in order to compensate for the pixel-to-pixel variation as in reduction of any CCD based data. Note that the flat here is obtained by lamp illumination. Dark current is usually small in MUSE CCD which could be ignored, but we decide take it into account in order to preform a complete reduction. As a IFS, wavelength calibration for MUSE is also necessary and is done by using arc-lamp data with the pipeline. In addition to this, the MUSE line-spread function (LSF) has also been taken into account to calibrate the finite spectral resolution. Finally, twilight flats are used to generate calibration file for illumination correction.

After the calibration preparation process, the files for the observation pre-processing are ready. In the pre-processing, the pipeline removes instrumental effects from the data using calibration files obtained previously and creates pixel tables for following reduction processes.

In the next observation post-processing step, observed flux is first calibrated using the observation of a standard star. Then the instrumental geometry and relative astrometry (See Section 2.2.5) are corrected. There is a mistake in our first run of the pipeline: the static calibration files used in this step, ASTROMETRY_TABLE which is necessary for WCS creation of the target cube, is accidentally missed and GEOMETRY_TABLE which amends the relative positions between slices with wrong date is used. This problem is identified by examining the front star, TYC 62-1194-1, in the final data and fixed accordingly by using the correct file.

The post-processing of the observation can be carried out by executing the muse_scipost recipe using EsoRex. We can obtain the final data cube by using this script. But in order to preform a fine tuning of the data reduction, we test different reduction procedures from this stage of reduction.

2.2.2 Cube Creation

To be more specific, there are 8 different reduction products (data cubes). The simplified summarization is shown in Table 2.1 for easy reference while the details are explained in

Table 2.1: The summarization of the differences in reduction processes of data cubes.

Cube Number	sky subtraction method	exposure combination method	label
1	ZAP	MPDAF, sigma clip	"mpdaf, nosky, sigma clip"
2	ZAP	MPDAF, median	"mpdaf, nosky, median"
3	ZAP	MPDAF, MAD	"mpdaf, nosky, mad"
4	pipeline	MPDAF, sigma clip	"mpdaf, pipesky, sigma clip"
5	pipeline	MPDAF, median	"mpdaf, pipesky, median"
6	pipeline	MPDAF, MAD	"mpdaf, pipesky, mad"
7	ZAP	pipeline	"pipeline, nosky"
8	pipeline	pipeline	"pipeline, pipesky"

text below:

1. First, each exposure has been reduced to a data cube using the standard pipeline without sky subtraction (in the pipeline "-skymethod=none"). Then, 8 data cubes go through Zurich Atmosphere Purge (ZAP, Soto et al., 2016) for fulfilling sky subtraction using principal component analysis (PCA). From the resulting data cubes, each individual white image has been created. The white image is created simply by summing the flux of the cube along wavelength axis. Then, corresponding segment files are produced from the white images with SExtractor (Bertin & Arnouts, 1996) which are used as masks when performing ZAP again on the obtained data cubes for removing sky residuals. Finally, exposure combinations is performed with MPDAF (mpdaf.obj.CubeList.combine) using sigma clip method (nclip = 5, nstop = 6) on the 8 cubes. This cube is marked as "mpdaf, nosky, sigma clip"

2. Similar to the first cube, the only difference is that the second is combined by using the median method (mpdaf.obj.CubeList.median). This cube is marked as "mpdaf, nosky, median".

3. Similar to the first two cubes, the third is combined by the median absolute deviation (MAD) method. This cube is marked as "mpdaf, nosky, mad"[2].

4. First, each exposure has been reduced to a data cube by the pipeline with sky subtraction. Then, 8 data cubes go through ZAP to remove sky residuals with white images, created by pipeline in parallel to cube creation, as masks. The resulting data cubes then combined by mpdaf (mpdaf.obj.CubeList.combine) using sigma clip method (nclip = 5, nstop = 6). This cube is marked as "mpdaf, pipesky, sigma clip".

[2]For an univariate data set $X_1, X_2...X_n$, $MAD = median|X_i - \widetilde{X}|$, where $\widetilde{X} = median(X)$

5. Similar to the reduction procedure of 4th cube, the difference of cube 5th is that it is combined with median method. This cube is marked as "mpdaf, pipesky, median".

6. Similar to the reduction procedure 4th cube, the difference of cube 6th is combined with MAD method. This cube is marked as "mpdaf, pipesky, mad".

7. The 7th cube is first combined directly by the pipeline from PIXTABLE of each exposure without performing sky subtraction. Then, it goes through ZAP for sky subtraction and is performed ZAP again with white image produced mask. This cube is marked as "pipeline, nosky".

8. The 8th cube is combined by pipeline with sky subtraction first and go through ZAP with white image created mask for sky residuals removal. This cube is marked as "pipeline, pipesky".

Note that except for the white images from which masks are created of 4th, 5th and 6th cubes, others are generated by simply summing the corresponding cube along the wavelength axis using MPDAF. Then, all following masks are obtained by SExtractor as mentioned above using saving segment image function. For cubes combined with MPDAF, their world coordinate systems (WCS) are assigned to be the same as the first exposure.

2.2.3 Self-Calibration Check

In MUSE DRS version 2.6, the method *autocalibration* has been implemented to improve the IFU-to-IFU and slice-to-slice flux variations. We adopt this feature during each of our reductions and register (AUTOCAL_FACTORS) the *autocalibration* results by adding "-save = autocal" when performing "muse_scipost" recipe.

It is necessary to perform this verification to make sure that for instance low surface brightness features are not affected or removed in this autocal process. To do this performance check, we compare the broad band images (Figure 2.1) attained from our new cube, "mpdaf, pipesky, mad", with previous cube reduced using old pipeline version (version 1.6.2, reduced by Sthabile Kolwa) in 3 wavelength bands: 5622-6380, 6608-6873 (Lyα) and 8073-8254 Å. Astrometry corrections are preformed on both cubes (see Section 2.2.5). It is clear that the background is more homogeneous after applying *autocalibration*.

In order to check whether the *autocalibration* correction degenerate the flux of our target, mainly Lyα emission line region, the AUTOCAL_FACTORS has been plotted using MPDAF. By examining the field of view visually, 4C04.11 located approximately on IFU

13, 14, 15 and 16 with Lyα seating in the 9th wavelength bin. The figures of correction factors are shown in Appendix A Figure A.1 - A.8.

2.2.4 Performance Comparison

With the eight cubes derived from different reduction methods, we can now evaluate the performance of the different methods and chose the one that maximizes the signal-to-noise for out target. We first extract the spectra from an aperture with a radius of 1" around the target. The aperture position is chosen in the 1st cube manually by approximately putting the center near the pixel with highest flux at Lyα peak. In order to compare the different methods, it is crucial to use exactly the same aperture center when extracting the flux from each of the 8 data cubes. For cubes 1st to 6th which are reduced using the same WCS system, this is can be fulfilled. The WCSs for 7th and 8th cubes are different to the other 6 which may cause additional uncertainties. To minimize the differences caused by the two set of WCSs in aperture positions, we manually use DS9 to locate the two apertures as close as possible. The positioning error here is estimated be $\sim$ 0.99 pixel (0.2 arcsec). The MPDAF method which we used for this spectrum extraction approximates a circular aperture around the offered center on the squared pixel field. A minor shift around 0.2 arcsec (considering the 1.3 arcsec seeing) could not arise severe problem.

Then we plot the eight spectra and their signal to noise ratios (S/N) together to perform a straight visual comparison. The noises used here are propagated by the reduction pipeline. Note that the ZAP dose not add any change to the variance extension of the resulting cube which we use as the noise. Its influence we consider could be neglected for now. The exposure combination method, median, does not have a defined way for variance propagation. Hence, there is no variance extension for the 2nd and 5th cubes. We choose to assign the variance from the 1st and 4th cubes to 2nd and 5th respectively to solve this problem. Because the sigma clipping method used for 1st and 4th cubes is an average method whose resulting variance can be used for approximating the ones of median cut method. The results from this comparison are shown in Figure 2.2. At the full wavelength range, it is difficult for us to detect any minor difference because their performances are relatively similar in terms of S/N. Hence, the more detailed analysis is necessary for deciding the most satisfying one.

In order to accomplish this, four wavelength bands are determined (shown between the vertical dotted lines):

- band 1: 5400-6000 Å, blue part of the spectrum without strong emission lines
- band 2: 6567-6864 Å, wavelength range of Lyα emission line
- band 3: 7225-8074 Å, red part of the spectrum without strong emission lines, noisy seen from the spectrum (Figure 2.2)

- band 4: 8278-9210 Å, wavelength range of CIV and HeII lines

We compare the spectra and their associated S/N between 8 reduction methods in these 4 bands. To make an effective comparison, we first choose to plot the spectra and S/N in pairs: 1st cube with the 4th cube, 2nd cube with the 5th cube, 3rd cube with the 6th and 7th with the 8th. Two spectra in any one of the pair have only one difference, e.g. the only difference between cube 1 and 4 is the sky subtraction method (pipeline vs. ZAP). The description and results for this qualitative comparison are shown in Appidenx B.

Table 2.2: The quantitative S/N check for the spectra extract from the 8 data cubes.

Cube Number	Mean	Standard Deviation	Median
$5600-5900$Å			
1	2.21	2.29	2.11
2	1.83	2.36	1.69
3	2.06	2.24	1.94
4	2.53	2.17	2.41
5	2.13	2.18	2.02
6	2.41	2.16	2.46
7	2.07	2.01	1.93
8	2.26	2.03	2.04
$7400-8000$Å			
1	5.44	3.52	5.86
2	4.96	3.26	5.50
3	5.09	3.32	5.52
4	6.77	3.07	6.98
5	6.42	3.05	6.73
6	6.62	3.06	6.93
7	5.58	2.89	5.87
8	5.52	2.57	5.78

From these preliminary qualitative examinations, we conclude in Appidenx B that the best reduction method is the one using pipeline doing the sky subtraction and using CubeList to combine with MAD method, namely the 6th cube "mpdaf, pipesky, mad".

To quantify this comparison, we calculate mean, median and standard deviation of the S/N for these 8 spectra in two continuum wavelength region ($5600-5900$Å and $7400-8000$Å which are part of the band 1 and 3 respectively). The results are shown in Table 2.2 which clearly shows that the 4th and 6th cube perform better than other 6 (much higher mean and median while relatively lower standard deviation). The performances of these two

cubes are similar and the differences between the mean and median are minor. We decide to use the 6th cube, "mpdaf, pipesky, mad", for its slightly lower standard deviation than the 4th cube in this two wavelength ranges. This is reasonable given that the 4th cube is combined using sigma clip method which is more prone to extreme values than the cube combined with MAD method.

2.2.5 Astrometry Correction

In the pipeline running, the relative astrometric calibration for the purpose of WCS creation in which an astrometric reference catalog containing 11 fields of 6 globular clusters has been used. This calibration only corrects the relative positions between the telescope pointing and reference star which depends on many factors, e.g. mechanical flexures, accuracy of the reference star astrometry and calibration errors of the guide probes. The resulting WCS is only an approximation, and the absolute correction is needed. Hence, we preform the WCS correction on our own by using SAOimage DS9 (DS9) (Joye & Mandel, 2003) based on the second Gaia (Gaia Collaboration et al., 2016, 2018) Data Release (GDR 2). The initial concept is correlating the targets in our MUSE FOV with the GDR 2 data base to identify their Gaia registered WCSs and calculate shifts. Then we subtract the averaged WCS shifts from reference MUSE WCSs RA and Dec respectively. Fortunately, one field star, the TYC 62-1194-1 (RA: 47.952584 deg, DEC: +5.1255053 deg), has been registered by Gaia in the FOV. This is a common situation considering our target located far from the galactic plane. Therefore, the correction is implemented by using this unique object. The pipeline corrected coordinates of the target star are obtained by preforming a simple 2D Gaussian fit. This position error estimated in this astrometry correction is 0.007 arcsec for which a large fraction ($> 98\%$) comes from the Gaussian fit. The astrometry correction is done in the wavelength at 6607 Å around the Lyα peak.

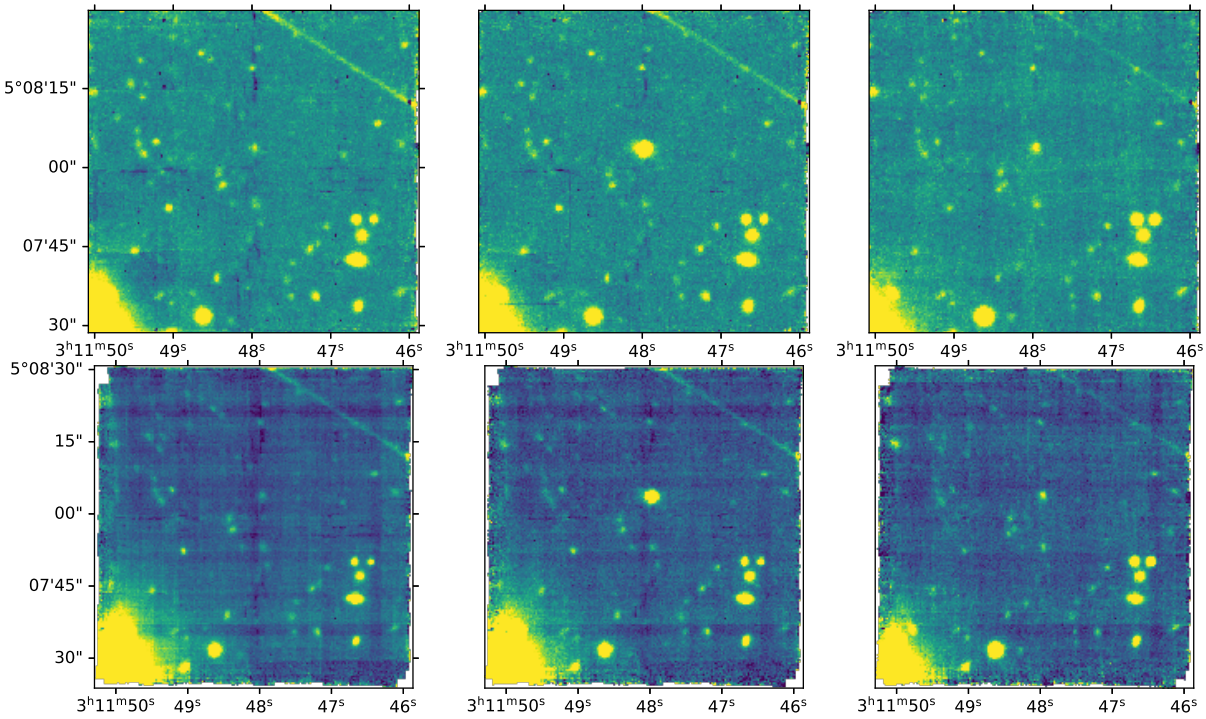

Figure 2.1: The broad band images of the whole FOV for *autocalibration* performance checking. The three plots in first row are the broad band images derived from the cube produced using *autocalibration* (See text). The three plots in the second row are reduced using version 1.6.2. The first, second, and third column are broad band images derived in wavelength 5622-6380, 6608-6873 (Lyα), and 8073-8254 Å respectively. The effect of *autocalibration* is obvious comparing the first with second plot in a same column. In every column, the first plot always looks more homogeneous and has less dark line structures due to IFU edges. The bright line at the top right corner of each plot is the result of cosmic ray in the first exposure. It is noticed that there is a slightly difference in the WCS of the images bwtween the newly and the previously produced cubes. This is caused by two reasons: 1) the pipeline performs differently between these two versions which can also be seen from the pixel size difference (not obvious by visually checking); 2) the astrometry correction could add extra error because it is a step highly dependent on manual operation (Section 2.2.5).

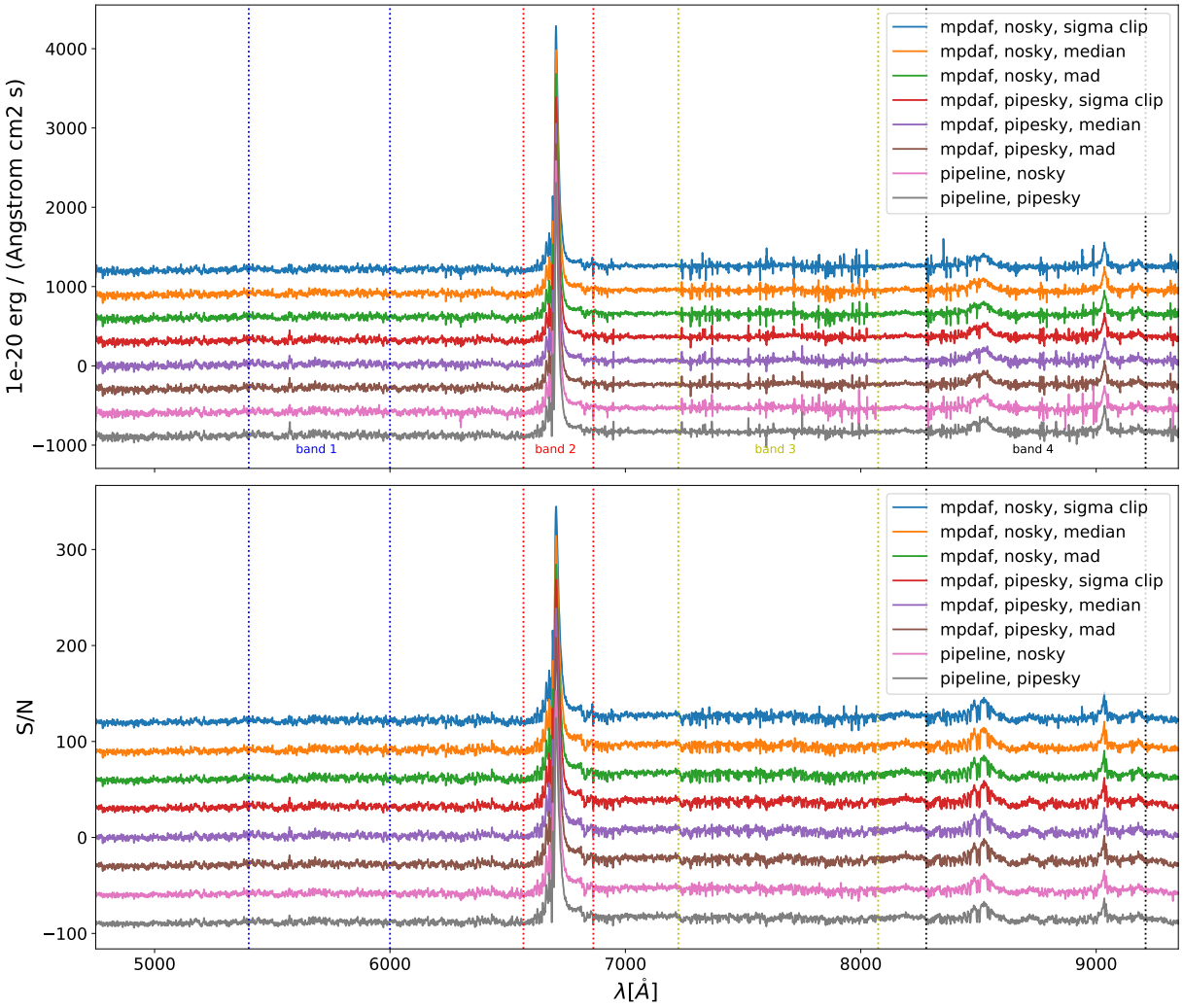

Figure 2.2: Spectra extracted from the eight cubes and associated signal to noise ratios. Each spectrum is extracted from an aperture around the target region with radius of 1 arc. The four marked wavelength bands are used to go scrutiny for the reduction performance. **Upper panel**: spectra of the eight cubes. Each spectrum is shifted by 300 of the unit value from the adjacent one. The 5th spectrum, "mpdaf, pipesky, median", is unshifted. **Lower panel**: Signal to noise ratio from the eight cubes. Each is shifted by 30 from the adjacent one. The 5th S/N is unshifted.

Chapter 3

Spectrum Extraction and Line Fitting

In this chapter, the details of the extraction and fitting of the 1D spectrum of 4C04.11 will be reported. In the MUSE observation of 4C04.11, the Lyα, CIV and HeII lines are clearly detected. The other fainter typical UV emission lines of HzRGs whose rest frame wavelength shorter than $\sim$ 1688 Å, e.g. NV and SiIV/OIV] (See McCarthy, 1993), are not detected.

3.1 Spectrum Extraction

With the derived data cube from the most optimized procedure (Section 2.2.4), we first implement a test through which the radius for the spectral extraction is determined. The center of the extraction aperture is chosen manually near the pixel with the highest flux. Then three spectra are extracted from apertures with radii 0.5, 1 and 1.5 arcsec (See Figure 3.2 top panel). By comparing the three spectra, we find that: the line flux ratio for the 0.5 arcsec to 1 arcsec is proportional to their area ratio which means that the background does not dominate. But the line flux ratio for the 1 arcsec to 1.5 arcsec spectrum is larger than their area ratio. Based on this test, we think the spectrum extracted from the 1 arcsec aperture is best choice for our following fitting. The extracted spectrum from the 1 arcsec aperture (Figure 3.1 green circle) is shown in the middle panel for emission lines and in the bottom panel for continuum of Figure 3.2.

3.2 Emission Line Fitting

3.2.1 Fitting Procedure

We fit models to the emission lines to study the physical properties of the gaseous halos of 4C04.11, e.g. the emitted flux and absorber column density. To do this task properly, we use the Gaussian model to describe the emission and Voigt profile (e.g. Tepper-García,

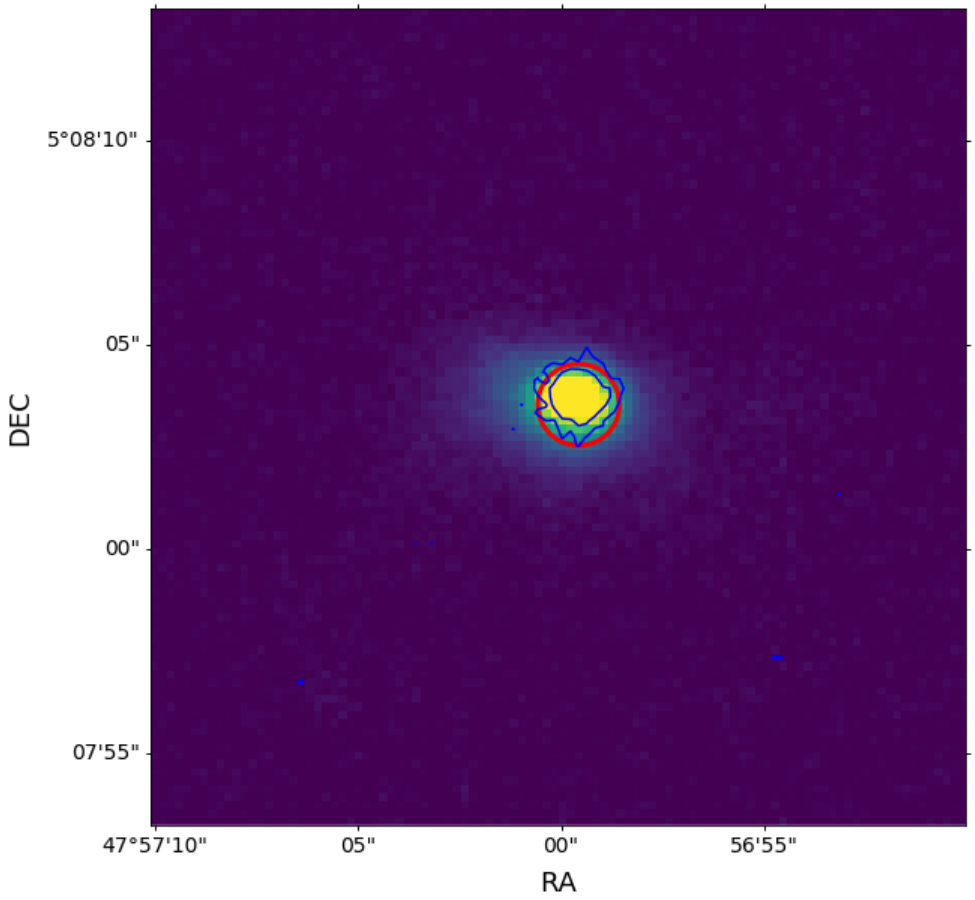

Figure 3.1: The Lyα narrow band image of 4C04.11 derived from 6704-6710 Å in observed frame. The blue contour indicates the HeII emission region. The overlaid red circle with 1 arcsec radius marks the aperture over which the spectrum is extracted.

2006) for the absorption. The Gaussian model is expressed as

$$\mathrm{F}_{\lambda,\mathrm{G}} = \frac{\mathrm{F}}{\sigma_\lambda\sqrt{2\pi}}\exp[-\frac{1}{2}(\frac{\lambda-\lambda_0}{\sigma_\lambda})^2], \tag{3.1}$$

where the F is the integrated emission flux of the line, σ_λ is the line width, λ_0 is the line center and λ is the wavelength at which the flux density, $\mathrm{F}_{\lambda,\mathrm{G}}$, is calculated. The absorption can be described as $\mathrm{e}^{-\tau_\lambda}$ by the radiation transfer theory. The parameter, optical depth τ_λ, is approximated by the Voigt-Hjerting (Voigt for shorter) function,

$$\tau_\lambda = \frac{\sqrt{\pi}\mathrm{e}^2\mathrm{f_i}\lambda_0^2}{\Delta\lambda_\mathrm{D}\mathrm{m_e}\mathrm{c}^2} \times \mathrm{N} \times \mathrm{H(a,x)}, \tag{3.2}$$

where N is the column density, e is the electron charge, $\mathrm{m_e}$ is the electron mass, c is the speed of light and $\mathrm{f_i}$ is the oscillator strength. The $\Delta\lambda_\mathrm{D} = \frac{\mathrm{b}}{\mathrm{c}}\lambda_0$, where b is the Doppler

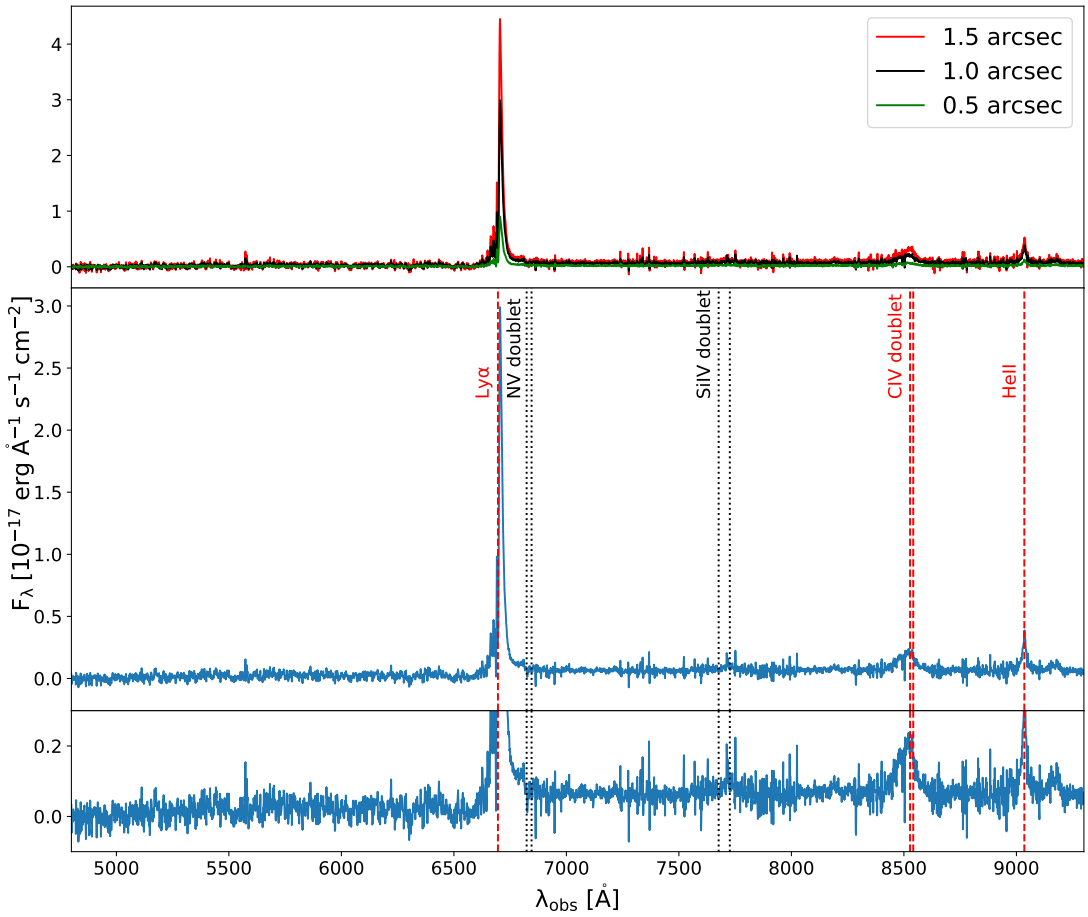

Figure 3.2: **Top panel**: the full spectra extracted from apertures with radii 0.5, 1 and 1.5 arcsec. **Middle panel**: the full MUSE spectrum extracted from the central 1 arcsec aperture region. The detected UV lines (Lyα, CIV and HeII) are marked with red dashed lines while two typical UV lines (NV and SiIV) without confident detection are marked with black dotted lines. **Bottom panel**: the same plot to the middle panel but zoomed-in to show the continuum. Note the skyline residuals seen as regions with higher noise.

parameter. H(a,x) is the Hjerting function defined as

$$\mathrm{H(a,x)} \equiv \frac{\mathrm{a}}{\pi} \int_{-\infty}^{+\infty} \frac{\exp(-\mathrm{y}^2)}{(\mathrm{x}-\mathrm{y})^2 + \mathrm{a}^2} \mathrm{dy}, \tag{3.3}$$

where $\mathrm{x} \equiv \frac{(\lambda - \lambda_0)}{\Delta\lambda_\mathrm{D}}$ The constant a is defined as

$$\mathrm{a} \equiv \frac{\lambda_0^2 \Gamma_\mathrm{i}}{4\pi \mathrm{c} \Delta\lambda_\mathrm{D}}, \tag{3.4}$$

where Γ is the Lorentzian width. Tepper-García (2006) approximate the H(a,x) for system whose column density $< 10^{22}$ cm^{-2} as

$$\mathrm{H(a,x)} = \mathrm{H_0} - \frac{\mathrm{a}}{\sqrt{\pi}\mathrm{x}^2} \times (\mathrm{H_0} \times \mathrm{H_0} \times (4\mathrm{x}^4 + 7\mathrm{x}^2 + 4 + \mathrm{Q}) - \mathrm{Q} - 1), \tag{3.5}$$

where $\mathrm{H_0} = \exp(-\mathrm{x}^2)$ and $\mathrm{Q} = 1.5\mathrm{x}^2$. The calculated Voigt profile by the aforementioned equations, $e^{-\tau_\lambda}$, is then convolved with the line spread function (LSF) of MUSE to match the observed resolution,

$$\mathrm{CV} = \mathrm{e}^{-\tau_\lambda} \circledast \mathrm{LSF}(\lambda). \tag{3.6}$$

The LSF is described by a Gaussian model with a full width of half maximum (FWHM) of 2.55 Å. The fitting procedure is implemented in PYTHON by the package LMFIT with the guidance from S. Kolwa (private communication). The convolution is realised through the fast-Fourier transform method in the package SciPy (Virtanen et al., 2019) similar to Krogager (2018). The final fitted function is

$$\mathrm{F}_\lambda = (\sum_{\mathrm{j=1}}^{\mathrm{m}} \mathrm{F}_{\lambda,\mathrm{G}}) \times \prod_{\mathrm{i=1}}^{\mathrm{n}} \mathrm{CV_i}(\lambda), \tag{3.7}$$

where n is the number of absorbers and m is the number of Gaussian components. The underlying assumption made when fitting the Voigt profile to the absorption is that each of the absorbing cloud gas has a covering factor close to unity to simplify the situation (C $\simeq$ 1.0).

The continuum underneath each line is subtracted with baseline before going into the fitting process. The baseline is estimated by a polynomial model to the first order with the emission part masked. When fitting each of the emission line, the fitting is first carried out by using the non-linear least-squares (least-squares for short) algorithm (Newville et al., 2016). In its process, the χ^2-minimisation is adopted to fulfill the fitting. We register and report the reduced $\chi^2_\nu = \frac{\chi^2}{\mathrm{N}-\mathrm{N_i}}$, where N is the number of inputted data points and $\mathrm{N_i}$ being the free parameter number. It is a complicated task when fitting the Gaussian(s) and Voigt(s) profiles simultaneously. Without any prior-knowledge for our spectrum, it is difficult to fit the line leaving parameters free. Hence, we first fit only the Gaussian part (details are elaborated in Section 3.2.3) and then adding the Voigt function to constrain the absorbers if there are any (e.g. only emission is needed for HeII fitting). When fitting the absorption, we follow Kolwa et al. (2019) to initially constrain the column density to be within $10^{13} - 10^{20}$ cm^2 and fit with least-square method. There are some problems when running the least-square with a large number of parameters, e.g. the covariance matrix from which uncertainties of the fitting are derived cannot be produced. Therefore, we apply a more sophisticated method, namely the Monte-Carlo Markov Chain (MCMC) which realises the fitting through maximizing the likely-hood using the package *emcee* (Foreman-Mackey et al., 2013), to obtain accurate fitting result with the output from the least-square method as input (See Section 3.2.3). During the process of implementing the MCMC fitting, several problems show up indicating that the previous coding of Voigt profile using

the approximation by Tepper-García (2006) may be divergent at some values when exploring the parameter space. We test the possibility that using a more sophisticated function, Faddeeva function[1], to approximate the Voigt function following Bolmer et al. (2019). But it fails to produce the expected result probably because the resolution of MUSE does not allow such a delicate function to work. Hence, we keep the Tepper-García (2006) approximation which has proved to be successful on MUSE data(Kolwa et al., 2019) and change the function such that it will replace the extreme values by the average of the adjacent to circumpass the divergence.

3.2.2 HeII

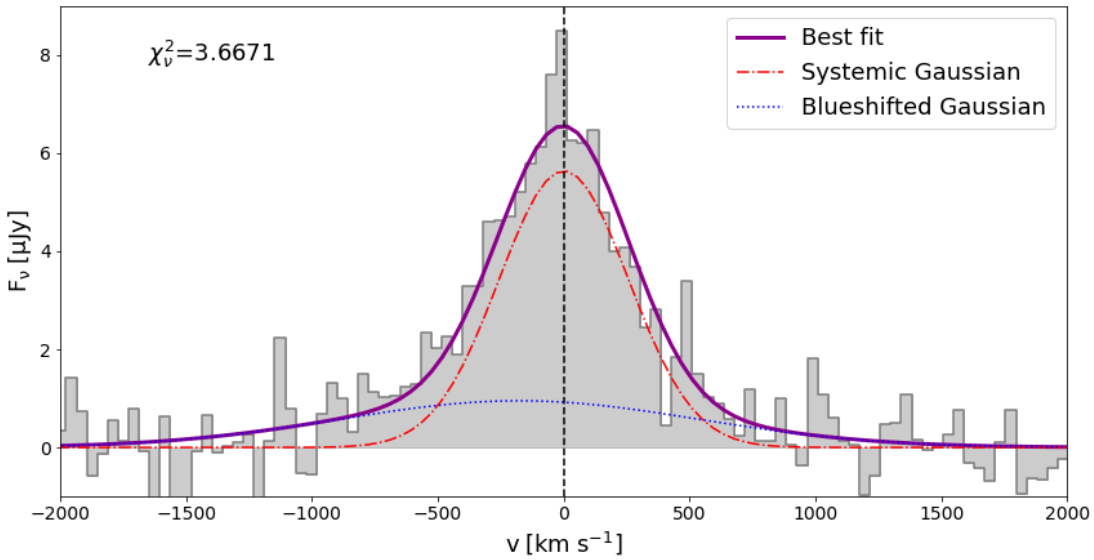

Figure 3.3: The best fitted model of the HeII line with two Gaussian. The dark magenta line represents the best fit while the red dotted-dashed line and the blue dotted line trace the intrinsic and blueshifted emissions respectively. The velocity zero is adopted according to the systemic HeII emission.

The first line we focus on is the HeII which is the brightest non-resonant line often used for determination of the systemic redshift of HzRGs (e.g. Swinbank et al., 2015; Kolwa et al., 2019). The non-resonant photons are produced through cascade recombination of He^{++} which are not energetic enough to induce other transitions and suffer less from scattering than resonant lines (e.g. Lyα). Previous work which determines the redshift of 4C04.11, e.g. Kopylov et al. (2006), based on the Lyα line which is a resonant line and heavily suffered from absorption (See Section 3.2.3). Hence, our fitting of the HeII will improve the fitting and increase the accuracy of the systemic redshift determination.

[1]https://docs.scipy.org/doc/scipy/reference/generated/scipy.special.wofz.html

The fitting procedure is first carried out following Section 3.2.1 using a simple one Gaussian model. The initial guess for the redsfhit (line center), 4.514, is from Kopylov et al. (2006), the line flux and width are given as random values. The fitting limitation for the line center is chosen to be ± 2 Å, and the limitation for line flux and width are leaving free. The quality of this primary fitting is not too far from the truth. But it could be improved by adding a Gaussian to describe the excessive broadness of the line.

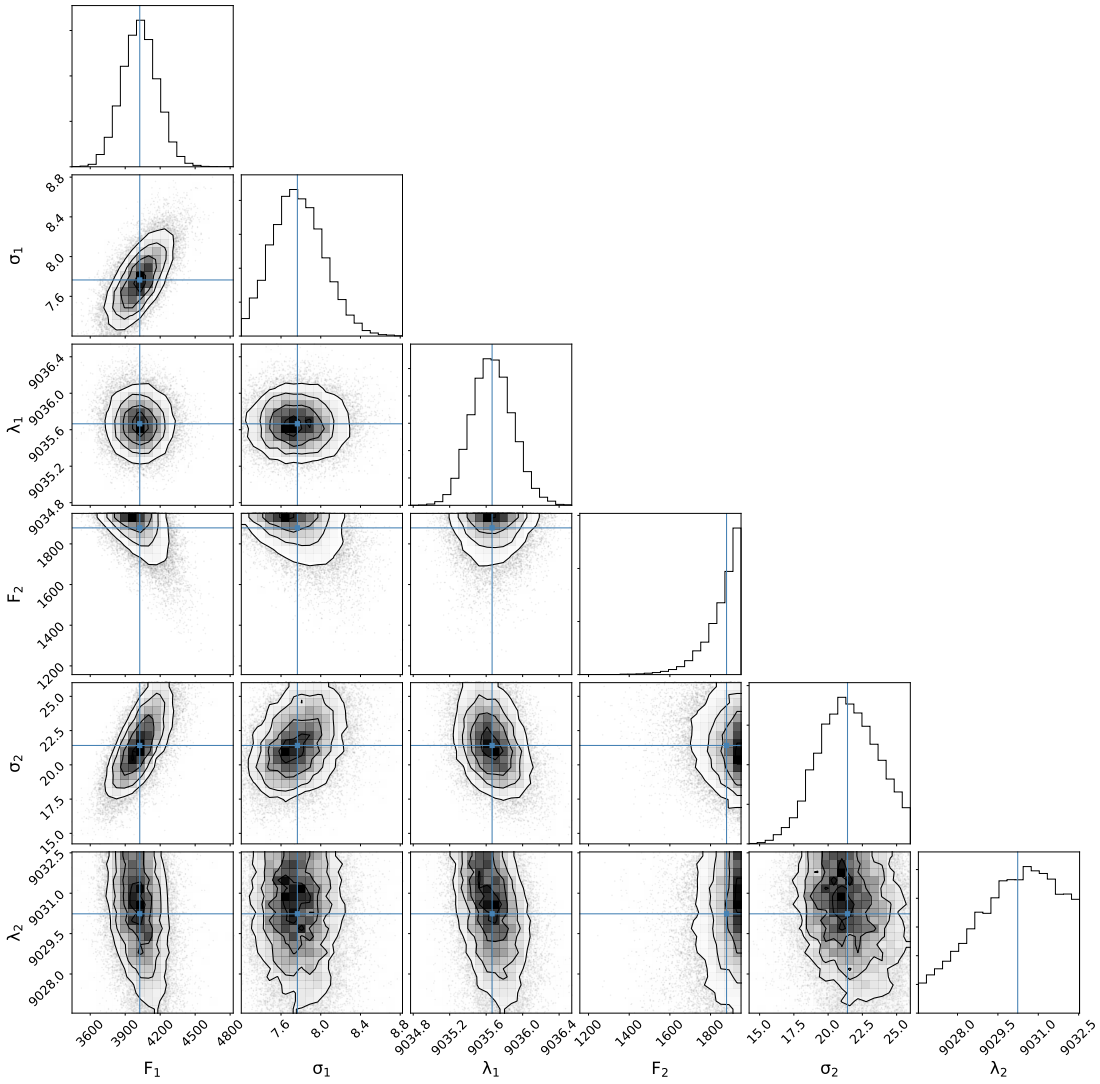

Figure 3.4: The corner plot derived from fitting the HeII line using MCMC method. The F, σ and λ are line flux (10^{-20} erg s^{-1} cm^{-2}), line width (Å) and line center (Å) respectively. The footnote 1 and 2 mark the intrinsic Gaussian and blueshifted Gaussian. As shown in this figure, the probability distribution between each pair of fitted parameters are well defined, i.e. no degeneracy showing in this fitting.

Therefore, an additional Gaussian model is included for the second fitting. Following Section 3.2.1, a least-square fitting is carried out first to constrain the parameters to a satisfied extend then followed by the MCMC fitting to increase the accuracy. The results is reported in Table 3.1 and the best fitted models are plotted in Figure 3.3. With MCMC method doing the fitting, we can obtain the corner plot which tracing the correlations between each of fitted parameters (Figure 3.4). The blueshifted (b.l.) component is at -180 ± 54km s^{-1} relative to the systemic redshift. It is noticed that the detected HeII line profile is not as asymmetric as compared to other HzRGs, (e.g. MRC 0943-242, Jarvis et al., 2003; Kolwa et al., 2019). We include the second Gaussian here to improve the fitting which is applied by many other works (e.g. Mullaney et al., 2013; Perna et al., 2019). The physical interpretation behind is that there could be an additional component of the emitting gas with different velocity. Though the fit improvement by the second component is minor, this decision is not unrealistic given the fact that the asymmetric profile towards the blue wing is seen in Lyα and the implementation of a blueshifted emission component also improves the fitting of Lyα line (See Section 3.2.3).

The systemic redshift calculated from the intrinsic HeII emission is $z = 4.5079 \pm 0.0001$ which is a significant improvement compared to Kopylov et al. (2006) (~ 10 Å difference of the HeII center wavelength). In Nesvadba et al. (2017), the observation by Spectrograph for INtegral Field Observations in the Near Infrared (Eisenhauer et al., 2003; Bonnet et al., 2004, SINFONI) of our source is reported and the [OII]$\lambda\lambda 3726, 3729$ ([OII]), a non-resonant line, is detected to good S/N. The redshifts reported in Nesvadba et al. (2017) based on [OII] fitting are 4.5100 ± 0.0001 and 4.5040 ± 0.0002 for the two narrow Gaussian components used, respectively. Our fitted systemic redshift is in between these two values which is considered to be reasonable and consistent with the near infrared observation. In addition, the authors also detect and include a broad blueshifted component ($\Delta v \simeq -240$ km s^{-1}, FWHM $\simeq 1400$ km s^{-1} consistent with our HeII blueshifted component). This independent detection of a consistent blueshifted line supports our interpretation from the HeII fitting that there is a separate velocity component in the line-emitting gas.

Table 3.1: Best fitted emission results using MCMC method.

Ion	Line center (rest) λ_0 [Å]	Line center (obs.) λ [Å]	Line flux F [10^{-17} erg s^{-1} cm^{-2}]	Line width FWHM [km s^{-1}]
Lyα	1215.67	6693.98 ± 0.59	117.13 ± 4.73	1482 ± 22
Lyα (b.l.)	1215.67	6690.62 ± 0.45	51.62 ± 0.91	3168 ± 39
HeII	1640.47	9035.66 ± 0.22	4.0 ± 0.1	606 ± 20
HeII (b.l.)	1640.47	9030.23 ± 1.64	1.87 ± 0.08	1673 ± 175

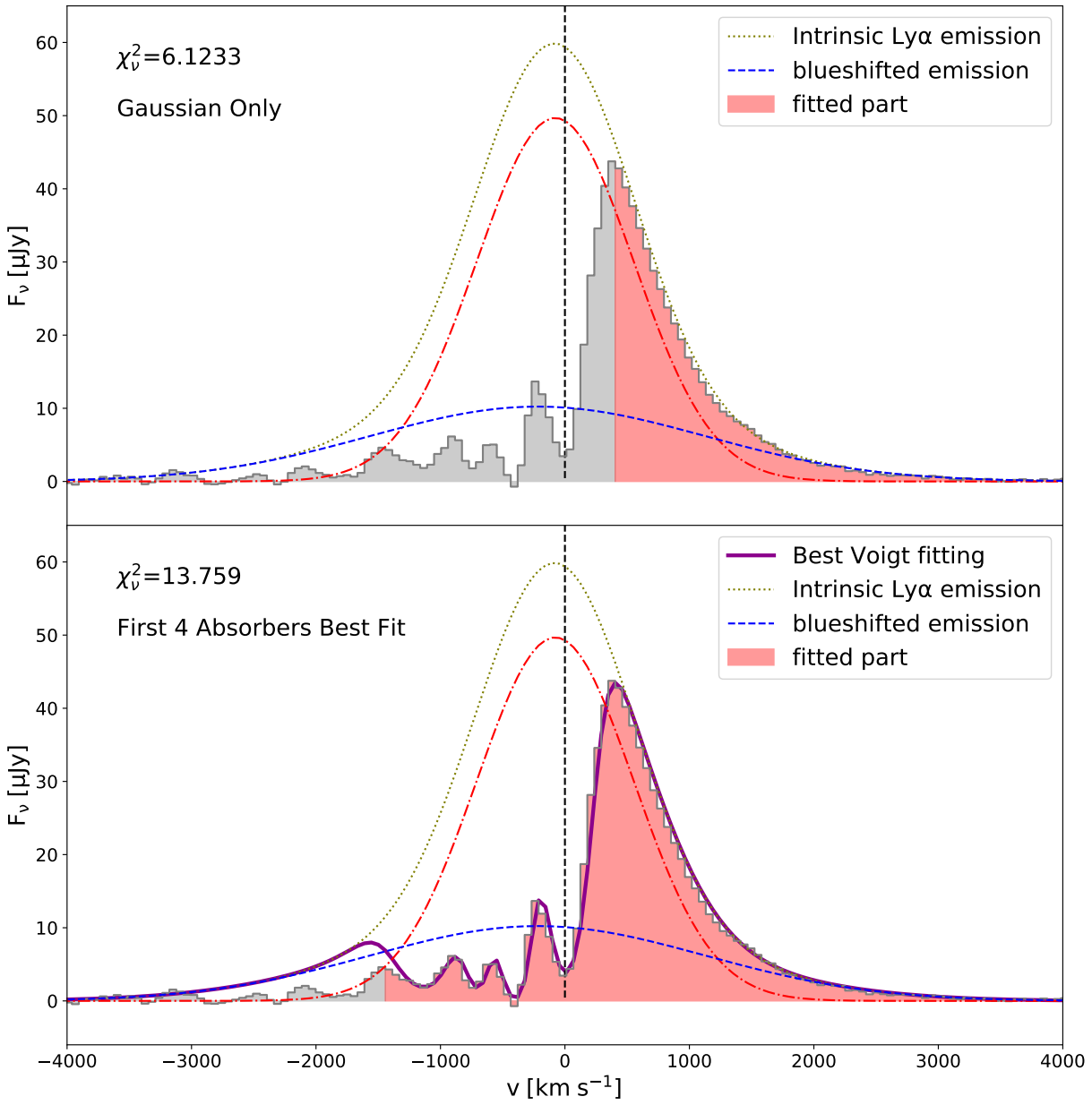

Figure 3.5: This figure presents the individual procedures to fulfill the task of Lyα fitting (See text). The velocity zero marked by the dashed vertical black line is derived from the HeII systemic redshift. **Top Panel**: The Lyα line fitted with only the Gaussian model. This fit is done by given the red wing of Lyα line as input (shown as red filled part in the figure). The dotted olive line traces the Gaussian emission while the blueshifted emission is marked by blue dashed line. **Bottom Panel**: The best Voigt fitting result to the first 4 absorbers. The dark magenta line shows the best fit while the fitting input is filled with red.

Table 3.2: Parameter constraints implemented to fitting Lyα for the final results.

Fit parameters	Lower boundary	Upper boundary
Gaussian emission:		
Line center, λ_0 [Å]	$\lambda_{\rm initial}$ - 5	$\lambda_{\rm initial}$ +3
Line center (b.l.), $\lambda_{0,\rm blue}$ [Å]	$\lambda_{\rm initial}$ - 8.93	$\lambda_{\rm initial}$
Line flux, F [erg s^{-1} cm^{-2}]	90%$\rm F_{1\ or\ 2,initial}$	120%$\rm F_{1\ or\ 2,initial}$
Line width, σ [Å]	80%$\sigma_{\rm 1\ or\ 2,initial}$	120%$\sigma_{\rm 1\ or\ 2,initial}$
Voigt absorption:		
Column density log($\rm N_H$ /cm^{-2}) (absorber 1-8),	90%$\rm N^*_{H,initial}$	110%$\rm N^*_{H,initial}$
Doppler parameter b (absorber 1-8),	90%$\rm b^*_{initial}$	110%$\rm b^*_{initial}$
Absorber redshift z (absorber 1,2,5),	$\rm z^*_{initial} - 0.002$	$\rm z^*_{initial} - 0.001$
Absorber redshift z (absorber 3),	$\rm z^*_{initial} - 0.001$	$\rm z^*_{initial} - 0.002$
Absorber redshift z (absorber 4,6-8),	$\rm z^*_{initial} - 0.0025$	$\rm z^*_{initial} - 0.0025$

$\lambda_{\rm initial}$ is the observed Lyα wavelength calculated using systemic redshift derived from HeII fitting (See Section 3.2.2). The $\rm F_{1\ or\ 2,initial}$ and $\sigma_{\rm 1\ or\ 2,initial}$ are derived from primary Gaussian fitting (see text).
The * in the Vogit parameters indicate that the initial values used are corresponding to each of the absorber listed in front. The determination of the initial values are stated in the text.

3.2.3 Lyα

The Lyα line can be fitted next with the systemic redshift determined from HeII. As shown in Figure 3.5, the Lyα line is asymmetric and highly absorbed. With primary visual identification, we can detect at least eight absorbers. To fit the Voigt profile to this complicated line without any prior-knowledge is challenging (unlike Kolwa et al., 2019, which has previous high spectral resolution UV spectrum analysis as guidance). Hence, the first step is to determine the underlying emission using only Gaussian model. All the absorbers are located on the blue wing (one near the v = 0 km s^{-1}) of the Lyα line. Therefore, the red wing could be used to fit Gaussian model to the un-absorbed emission (See Figure 3.5 upper panel). When starting the fitting, it is obvious to find that only one Gaussian is not adequate to describe the profile. The broadness of the line exceeds the scope of one Gaussian with any line width (See Figure 3.5 that the excessive flux of the line beyond $\sim$ 1500 km s^{-1} is dominated by a broader component than the flux within). In addition, two-Gaussian fitting is implemented in the HeII fit procedure and proved to be effective (Section 3.2.2). Following the fitting procedure presented in Section 3.2.1, we fit the red wing of the Lyα line with two-Gaussian model. The line center of the intrinsic Gaussian is limited to the systemic redshift while the blue component is confined to the blueshifted region but not extending beyond -400 km s^{-1} (See the boundary of the line center in Table 3.2). With line widths and line fluxes having the initial values from guess and leaving boundary condition free, we obtain the fit result of the Gaussian emission shown in Figure

3.5. It is noticed that the fit results of line widths and line fluxes from this Gaussian fitting acts as the initial values in Table 3.2 for further Voigt fitting.

Table 3.3: The absorber fitting results of Lyα line using MCMC method.

Abs. #	Redshift z	Absorber wav. λ (Å)	Velocity Δ v (km s^{-1})	Column density log(N / cm^{-2})	Doppler b (km s^{-1})
1	4.50746 ± 0.00001	6695.26 ± 0.02	-23.4 ± 0.9	14.881 ± 0.006	187 ± 2
2	4.50002 ± 0.00002	6686.21 ± 0.02	-428 ± 1	15.25 ± 0.05	109 ± 3
3	4.49457 ± 0.00002	6679.58 ± 0.03	-725 ± 1	14.81 ± 0.01	128 ± 4
4	4.48693 ± 0.00005	6670.33 ± 0.06	-1139 ± 2	14.94 ± 0.02	261 ± 6
5	4.47483 ± 0.00007	6655.59 ± 0.09	-1799± 4	14.93 ± 0.02	239 ± 9
6	4.46539 ± 0.00006	6644.12 ± 0.08	-2313 ± 3	15.9 ± 0.1	64 ± 3
7	4.45738 ± 0.00009	6634.3 ± 0.1	-2749 ± 5	15.4 ± 0.1	133 ± 9
8	4.4461 ± 0.0002	6620.7 ± 0.2	-3361 ± 12	14.6 ± 0.1	78 ±21

With the underlying emission settled, the Voigt profile can be applied to fit the HI absorbers. However, it is still impossible to fit all eight absorbers simultaneously without the initial values of N_H and b confined to an accurate range. Hence, we first fit the first 4 aborbers with the data input just covered them and add more absorbers (Voigt functions) when we satisfied with the current fitting. The initial values for this crude fitting are chosen to be 15 for log(N_H /cm^{-2}) with the range 13-19 and 100 km s^{-1} for Doppler parameter, b, with the range of $40 - 400$ km s^{-1} according to Kolwa et al. (2019). The initial values for absorber redshifts are visually chosen with the boundaries shown in Table 3.2. The Gaussian parameters initial values and boundaries used are the ones shown in Table 3.2. Using least-square method, the derived fit is plotted in Figure 3.5 bottom panel with the registered χ^2_ν value. Then, we can move on to fit the 5th absorber. When doing this (similar to adding the 6th, 7th and 8th latter), we use the resulted N_H and b values from the previous fit (first 4 absorbers) as initials and limit them according to Table 3.2 while the initials and limitations for the newly added absorbers are still chosen as 15 for log(N_H /cm^{-2}) with the range 13-19 and 100 km s^{-1} for Doppler parameter, b, with the range of $40-400$ km s^{-1}. The individual fits with absorber 5 - 8 are not shown in the figures.

As discussed in Section 3.2.1, the primary fit is done with least-square method and changed to MCMC latter using the results from least-square as initial inputs. This fit procedure is determined first when fitting the Lyα line with no error output. The MCMC method is applied then for accurate results and uncertainties. Using the resulted values from previous least-square method with 8 absorbers as initials and boundaries shown in Table 3.2, we fit the Lyα line with MCMC method. The best fitting result is plotted in Figure 3.6 top panel and shown in Table 3.1 (for emissions) and Table 3.2 (for absorption). The blueshifted Gaussian component is at -231 ± 20 km s^{-1} which is coincident with the result of HeII fit within uncertainty in Section3.2.2 indicating these two may originate from

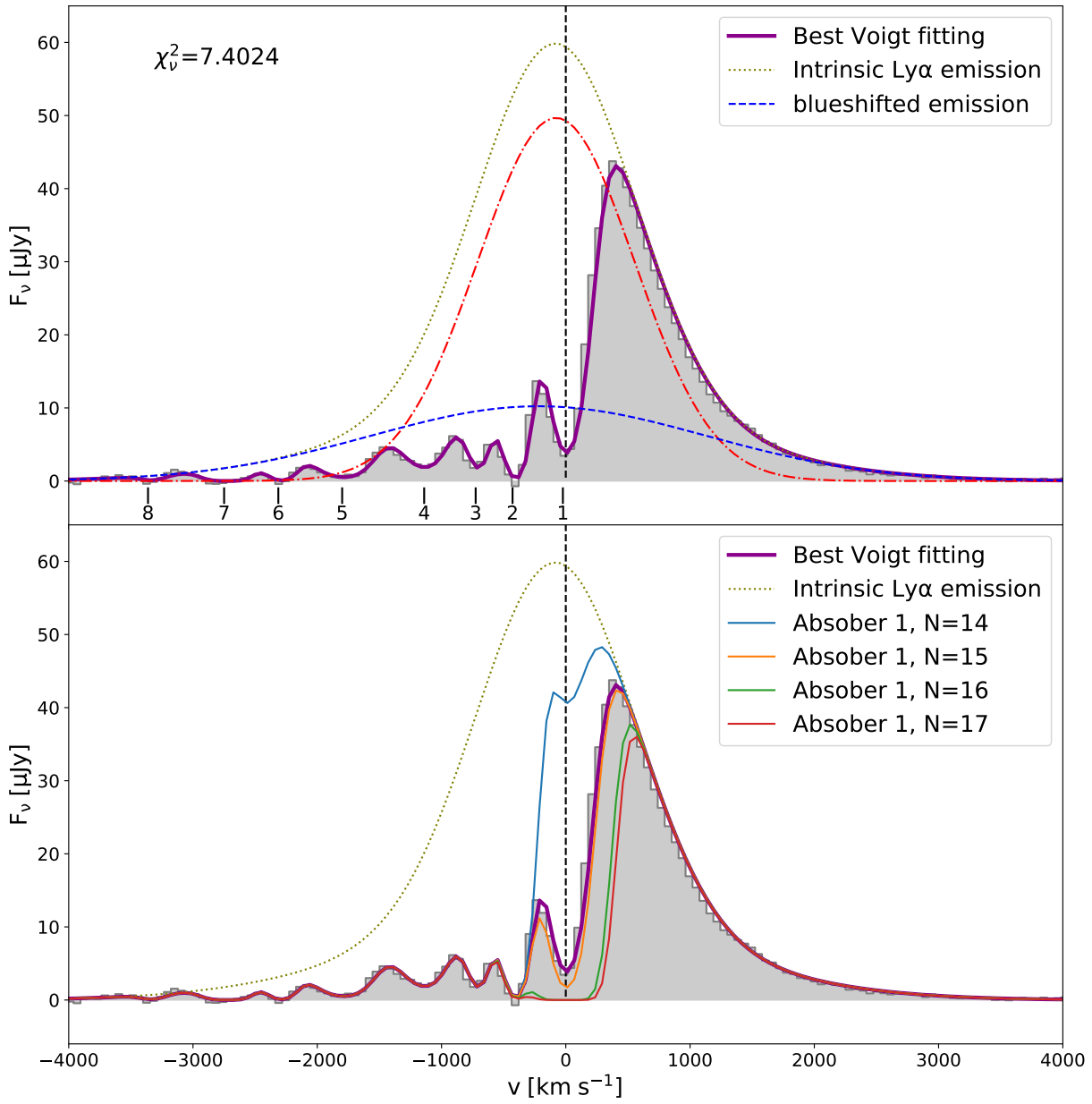

Figure 3.6: **Top Panel**: The best Voigt fitting results of Lyα line using MCMC method. The dark magenta line represents the best fitting while the dotted olive line traces the Gaussian emission. The blueshifted emission is marked by blue dashed line. The positions of all 8 absorbers are shown in this panel. **Bottom Panel**: The intrinsic Gaussian and Voigt fitting are the same with top panel. The other lines show how the Voigt fitting results will change by only adjusting the column density of the absorber 1 to $\log(N_{H1}/cm^2)$ =14, 15, 16 and 17. These lines demonstrate that this fitting is sensitive to the N_H value only around the best fitting result.

the same component.

In Figure 3.6 bottom panel, the N_H sensitive test for the model of the absorber 1 is shown. We vary the column density from 10^{14} cm^{-2} to 10^{17} cm^{-2} with all other parameters fixed to the best fitted values and find that the profile is only sensitive to the N_H near the best fit value (dark magenta line shown in the figure). Besides, the column density variations of one absorber has little influence on the others unless it is saturated.

It is worth noticing that the Voigt profile fitting done in this work with only MUSE data is just a primary result for two reasons:

- **The degeneracy between the column density and Doppler parameter.** It is a well known problem that different combinations of N and b can result the similar Voigt profile (e.g. Silva et al., 2018). The $N_H - b$ degeneracy check is done (See Figure 3.7) for absorber 1 and 2 following Silva et al. (2018). In each our cases, there is only one χ^2_ν minimum and one reasonable χ^2_ν value which is obtained around the N_H resulted from previous fit when leaving every parameter free. However, in Silva et al. (2018), the similar test give two local minima and several reasonable χ^2_ν values. These may indicate that the degeneracy is not presented in our analysis, but further investigation is needed.

- **Incompleteness of absorber identification.** The low spectral resolution of MUSE may raise some problem when resolving the absorbers. For instance, Figure 4 in Kolwa et al. (2019) shows that the narrow absorber of MRC 0943-242 is not able to be identified by MUSE with confidence but can be resolved by Ultraviolet Echelle Spectrograph (UVES, D'Odorico et al., 2000; Dekker et al., 2000). In some cases (e.g. MRC 0200+015, Jarvis et al., 2003), the deep absorber seen with low resolution spectrograph may split into two or more with lower column density.

Therefore, we need to be cautious when we interpret the results derived from MUSE line fitting alone.

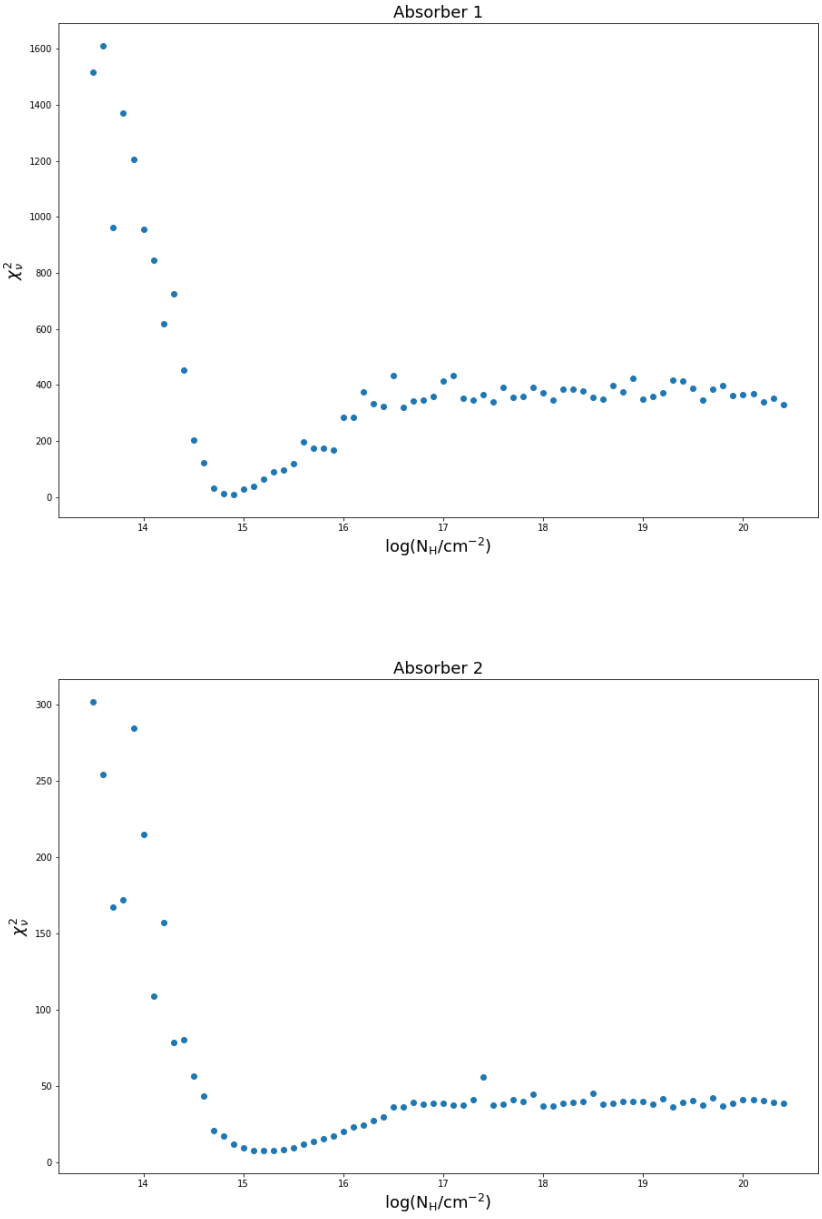

Figure 3.7: The figure of the $N_H - b$ degeneracy check following Silva et al. (2018). The figure shows how the fit quality (described by the χ^2_ν) changes with the column density for absorber 1 (Top Panel) and absorber 2 (Bottom Panel). For each of the absorbers, the fit is carried out by limiting the N_H value and leaving other parameters free.

Chapter 4

Spatial Mapping

In last section, we state the fitting of 1D emission lines of the aperture extracted spectrum. However, as a IFS, the capability of MUSE is far beyond, and we can use its data to spatially map the emission and absorption of HzRGs (e.g. Swinbank et al., 2015), i.e. fit spectra at each spatial positions using the procedure described in Chapter 3.

4.1 Spatial Tessellation

4.1.1 Voronoi Bin

To fulfill the task of spatial mapping, the first step is to do the spatial tessellation (binning) of region around our target to increase and homogenize the S/N. Voronoi binning (Vorbin) (Cappellari & Copin, 2003) is a commonly used method to bin the 2D data given a target S/N threshold. Hence, we first do the tessellation using the Vorbin package[1]. The spatial distributions of Lyα emission and associated HI absorbers are the most interesting features to explore. So, we focus on the Lyα first and use the Lyα flux measured from a velocity window of [-5000, +5000] km/s as signal value for each spatial pixel (spaxel) and the corresponding variance extension created by data reduction (See Chapter 2) as noise value. The region over which we run the tessellation method is chosen, by testing, to be 120×120 pixel^2 (24×24 arcsec^2 or 161×161 kpc^2) around the radio galaxy which is large enough to cover the brightest emission of the Lyα without leaving much low signal background. However, the Voronoi binning method is not ideal. It results in binning units split into multiple disconnected subregions independent of our choice of a the target S/N. The explanation behind this failure is reported in Cappellari & Copin (2003) to be the sharp S/N gradient. In our case, the S/N changes from ~ 120 to $\sim$ 10s in only 15 spaxels.

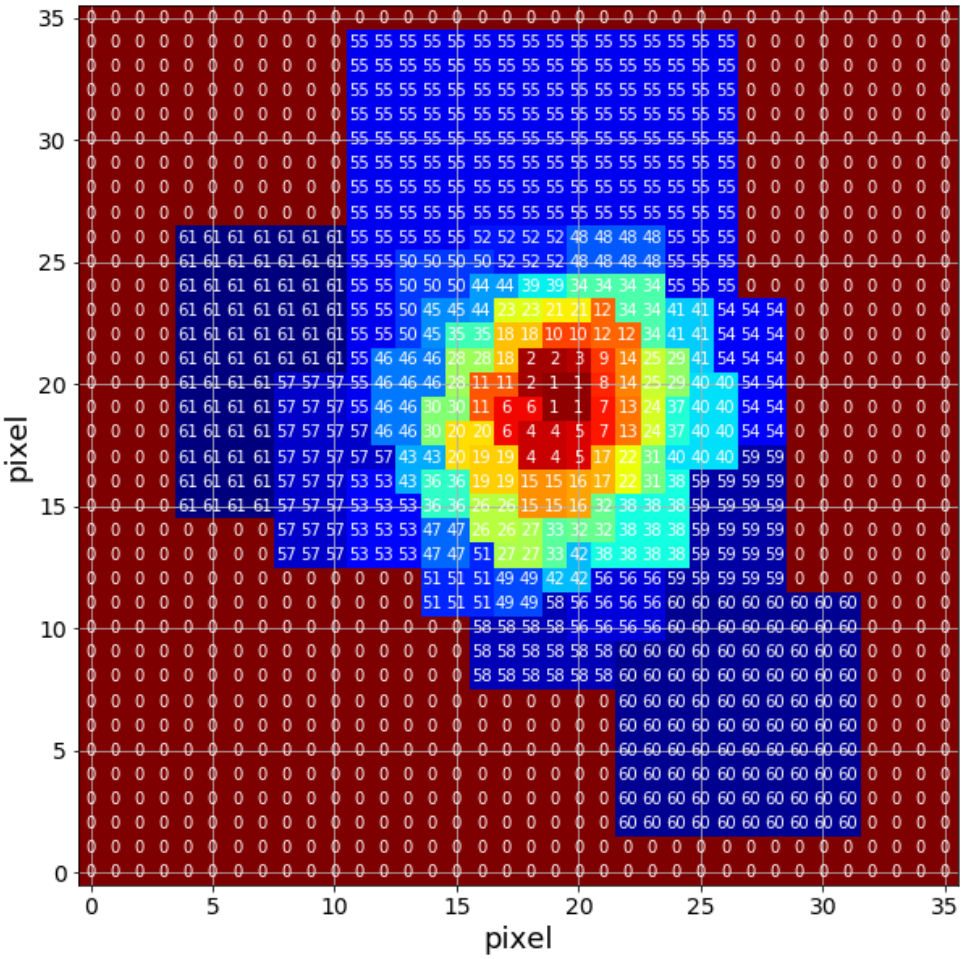

Figure 4.1: The tessellation map for 4C04.11 following Swinbank et al. (2015). The numbers indicate which bin each spaxels belongs to. The spaxels marked with 0 is the unbinned background. The field of view is zoomed into the central part.

4.1.2 Swinbank et al. (2015) Tessellation

Due to the unsuccessful binning using Voronoi method, we apply the tessellation method implemented in Swinbank et al. (2015). The idea behind this technique is simply that the algorithm will bin the spaxels around the brightest one until the given S/N threshold or the largest spaxel number in one bin is reached. Then, the algorithm moves do the second brightest spaxel and the same procedure is repeated. The wavelength range over which the signal and noise values for each spaxels are calculated is chosen to be 6672-6695 Å. This is not the same range previously used which covers the Lyα peak. Because we are more interested in absorbers, the wavelength range is decided accordingly to cover the first 4 absorbers. The FOV over which the Swinbank et al. tessellation is applied is the same

[1]https://pypi.org/project/vorbin/

stated in Section 4.1.1. The minimum and maximum bin sizes are chosen to be 2×2 and 25×25 pixel^2 while the S/N limitation is 15. The threshold is chosen by plotting the S/N distribution for each spaxels in the tessellation region and selecting a reasonable cut. After running the algorithm, we manually select a few bins which contain 1 or a few spaxels and merge them with their adjacent bins to make the resulted S/N map more homogeneous. The final result of the tessellation is shown in Figure 4.1 zoomed into the central region where binning is successful. The numbers in the figure indicate which bin (in the total of 61 bins) the spaxel belongs to while the 0 marks the unbinned background.

4.2 Fitting Procedure

After having determined the spatial binning regions, we stack the individual spectra in each spatial bin and extract. The first step of the fitting procedure, like Section 3.2.1, is to do the baseline fitting with the emission line region, 6561-6807 Å same for all resulting 61 spectra.

Secondly, following the 1D spectrum fit procedure in Section 3.2.1, we use the red wing of the Lyα profile to fit the Gaussian emission. The red wing is chosen individually for each spectrum depending on the wavelength at which the observed flux peaks. We previously set a two-Gaussian model for every spectra. However, this setup causes some problem as the blue (broad) component in several bins cannot be fitted. Hence, we develop an automatic way to choose the number of Gaussian by comparing the quality of fitting results (χ^2_ν) for each spectrum for the one- and two-Gaussian fit. This method works well for most spectra expect for a few single cases, e.g. some spectra are set to be described by two Gaussian are spatially isolated with one-Gaussian-fit bins in-between which is an un-physical situation. This may due to the fact that the χ^2_ν values for using one or two Gaussian are similar which leads the random selection of the automatic method. To improve this, we manually change the number of Gaussian will be used after the previous automatic selection by examining the plots of the fit and their spatial positions. The final result of this step is that two-Gaussian-fit bins are connected in the center with one-Gaussian-fit bins located in the outskirts. The fit is carried out in iteration (in ascending order of the bin number, roughly inside-out) such that the initial values of the next spectrum are taken as the resulted values of the previous one. The initial guess for the fitting parameters of the first spectrum (number 1 in Figure 4.1) are randomly chosen with some constraints added ($[70\%, 130\%]$ of the initial guess for amplitude and line width). The resulted Gaussian parameters are recorded and act as the initial inputs for following steps.

With the Gaussian emission settled, the next step is to decide the number of Voigt profiles used. In the first attempts, only absorber 1 and 2 are fitted given their extended spatial distribution. We then improve the method by dynamically determining the number of Voigt profiles that are used in each individual bin. This is accomplished by visually checking the number of appearing absorbers in each individual spectrum. The underlying

assumption here is that no strong velocity gradient is seen for absorbers which may cause them to shift significantly in velocity space raising identification problems.

After determining the number of Gaussian and Voigt profiles used for fitting each spectrum, the preliminary least-square fit can be carried out. In this procedure, the boundary condition differences, compared to Table 3.2, are: i) Line flux lower limit is $80\%F_{1\text{ or }2,\text{initial}}$, ii) Column density lower and upper limits (absorber 1-8) are 10^{13} and 10^{20} cm^{-2} respectively, iii) Doppler parameter b (absorber 1-8) lower and upper limits are 40 and 400 km s^{-1} respectively. For the initial values, Gaussian parameters for each spectrum are determined in the previous red wing fit. The Voigt parameters are chosen differently such that the results from the 1D spectrum fit (See Section 3.2.3) are adopted as initial values of the first spectrum (number 1 in Figure 4.1). As the fitting procedure progresses in the way described above , the initial values of the next spectrum are taken as the resulted values of the previous one. We obtain the preliminary results of the absorption spatial mapping in this least-square fit.

Finally, the MCMC fit can be implemented in parallel for each spectrum by using their individual least-square results as inputs. The boundary conditions for N_H and b are set according to Table 3.2 in this step to get accurate results.

4.3 Mapping Results

In this section, we present the mapping results of emissions and absorption of 4C04.11 following the fitting procedures in Section 4.2. The difference is that after the first attempt, we identify the N_H map and b map for each absorber are strongly correlated, i.e. the bin with higher (lower) column density has lower (higher) b value. This is the degeneracy we mentioned in Section 3.2.3. To reduce the fitting uncertainty caused by this degeneracy, we freeze the b parameters for each absorber in each bin when performing the spatial mapping using the values obtained in Section 3.2.3. The results are shown in Figure 4.2 to 4.5.

In Figure 4.2, the morphological and kinematical features of the Lyα nebula are presented. In Panel (a), the surface brightness of Lyα is shown. This is the fitted result of the Gaussian model which traces the un-absorbed emission. In Panel (b), the W_{80} parameters from the fitting are mapped. This parameter is calculated by using the cumulative un-absorbed flux as a function of velocity,

$$\phi(v) = \int_{-\infty}^{v} F_{v'}(v')dv'. \tag{4.1}$$

The $W_{80} = v_{90} - v_{10}$, where $\phi(v_{90}) = 0.9\phi(\infty)$ and $\phi(v_{10}) = 0.1\phi(\infty)$. The $\phi(\infty)$ represents the total flux of the line. In this work, the total flux is calculated in the range

[-10000,10000] km s^{-1}. W_{80} is a non-parametric way of measuring the line width which gives a more reliable result here given the fact that our Lyα may contain two or more Gaussian broadening the line. Panel (c) and (d) provide the velocity shifts of narrow and broad Gaussian component respectively.

In Figure 4.3, the maps of column density and velocity shift of absorber 1 (panel a and b) and 2 (panel c and d) are shown. The similar maps for absorber 3 and 4 are presented in Figure 4.4. For absorber 5-8, only the column density maps are offered in Figure 4.5 due to their limited spatial distributions and noisy velocity structures.

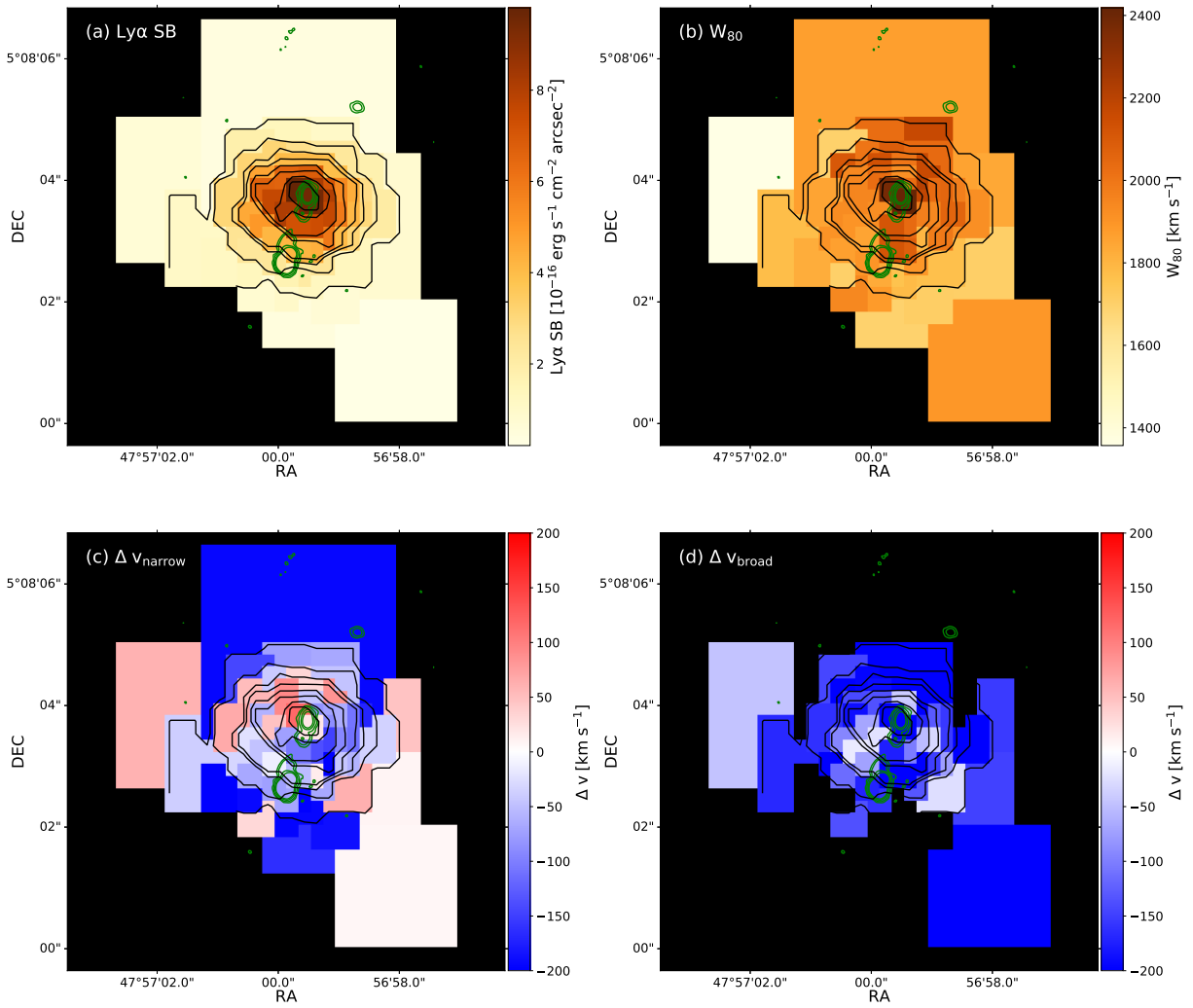

Figure 4.2: The figure presents: (a) the Lyα surface brightness(SB), (b) W_{80} parameters, (c) velocity shift of the narrow Gaussian component, (d) velocity shift of the broad component. The black contours illustrate the SB of Lyα emission while the green trace the position of radio jets observed by MERLIN (See Section 1.5).

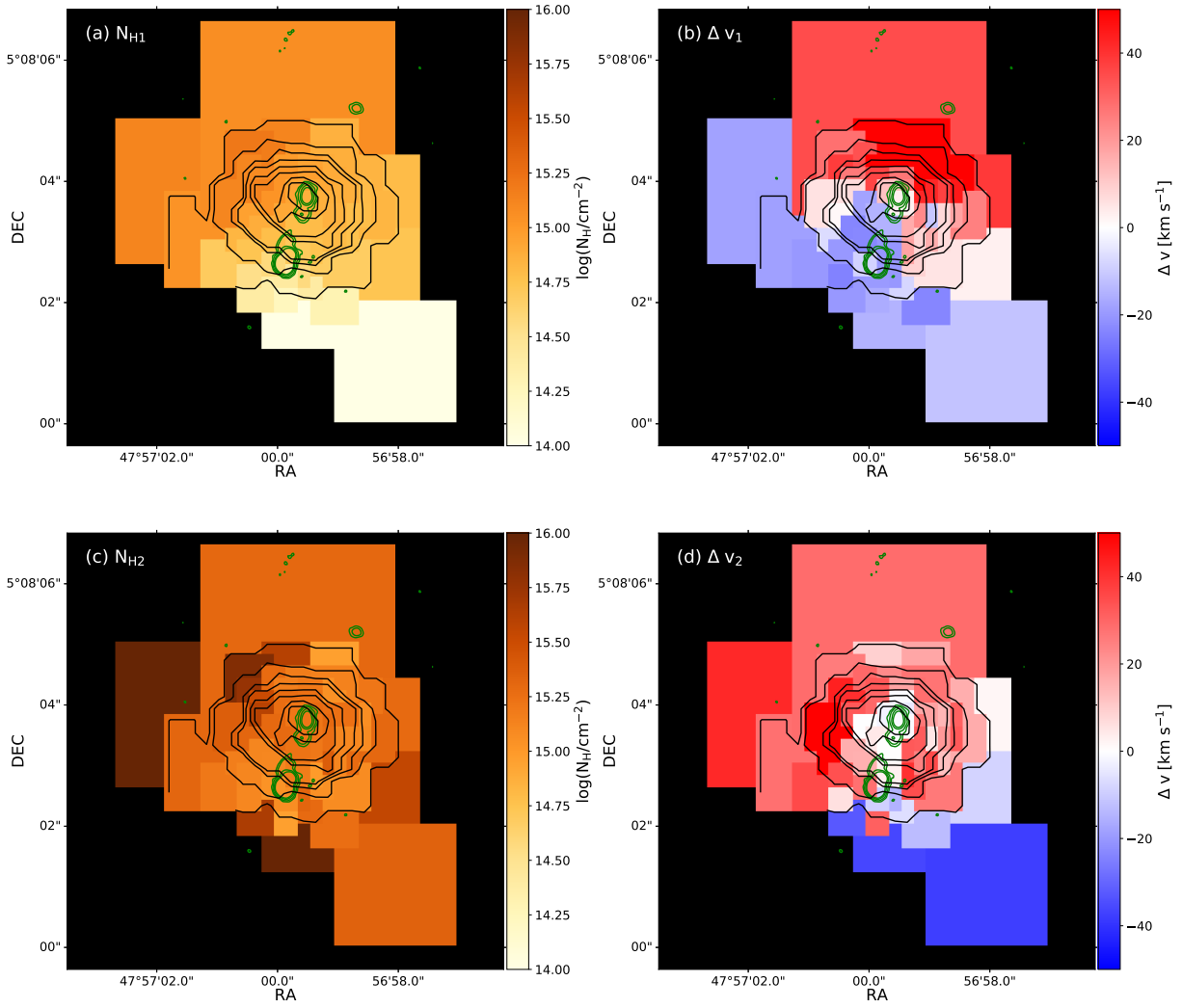

Figure 4.3: The figure presents: the fitted column density distributions of absorber 1 (a) and 2 (c) and velocity shifts of absorber 1 (b) and 2 (d). Counters in this figre are the same as Figure 4.2.

4.4 Interpretation

In Figure 4.2 panel (a), the surface brightness center of Lyα emission coincides with the radio center which marks that the energy source could be the central AGN. The W_{80} parameters in panel (b) have higher values in the center which indicates that the gas is more disturbed but the driving mechanism is unknown yet. The velocity shift map of narrow component is noisy not showing strong gradient difference. Given the spectral resolution of MUSE ($\Delta v \sim 100$ km s^{-1}), the panel (c) may imply the emission gas belonging to the narrow component does not show a gradient. The velocity shift of the broad component

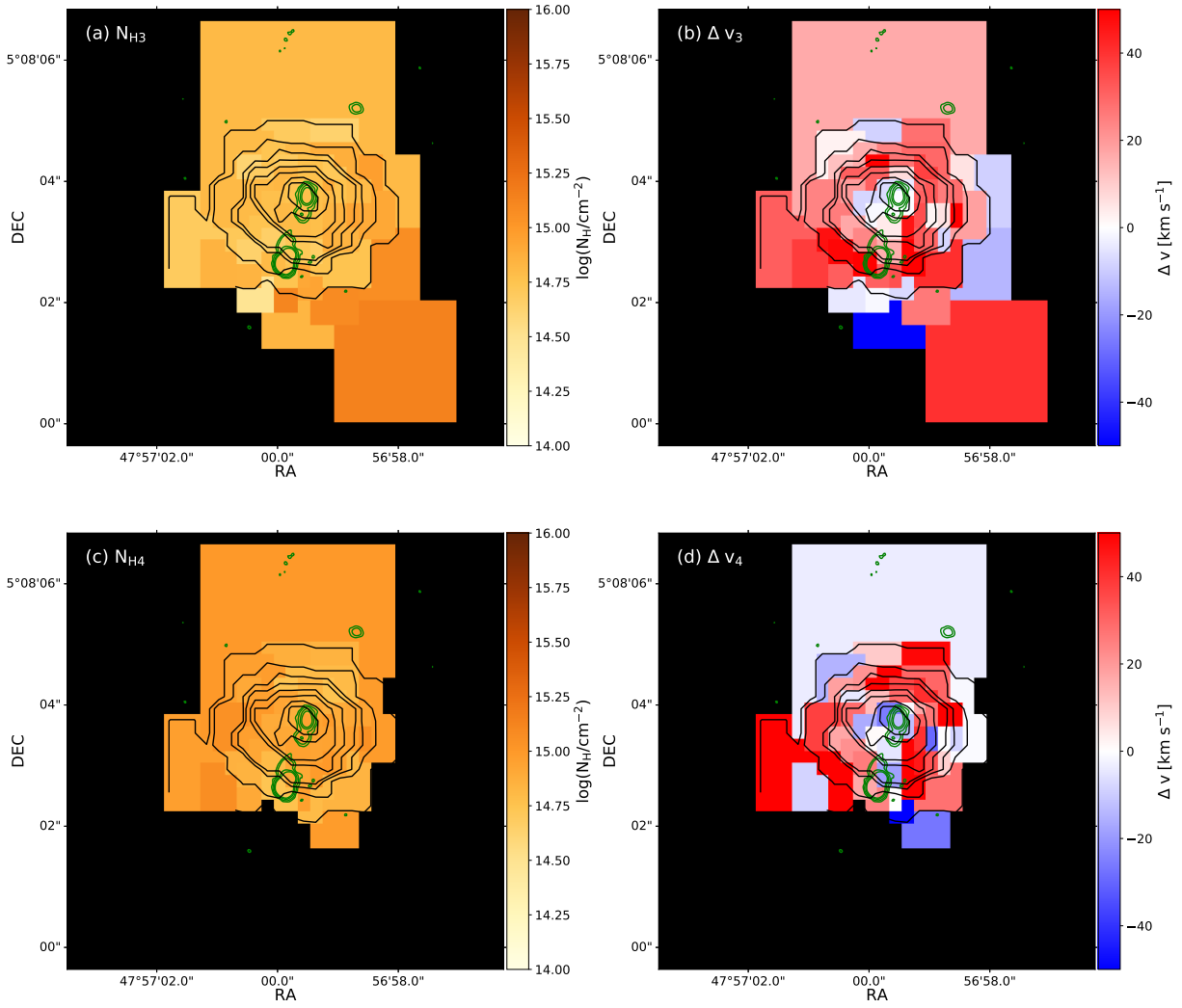

Figure 4.4: The figure presents: the fitted column density distributions of absorber 3 (a) and 4 (c) and velocity shifts of absorber 3 (b) and 4 (d).Counters in this figre are the same as Figure 4.2.

in panel (d) has a relative homogeneous morphology compact to the center and all values around $\sim -200\ km\ s^{-1}$. This suggests that the broad component mab be driven by the central source of the galaxy. It needs to be stressed that the number of emission components we used in the fitting is arbitrary and motivated by the fit quality not by physical reasons. Due to the resolution of MUSE, it is not clear how many Gaussian models should be included. Hence, this emission result interpretation is only preliminary.

The most interesting mapping results is the column density and velocity shift maps of absorber 1 (Figure 4.3 panel (a) and (b)). There is a clear column density gradient from northeast to southwest. The velocity gradient is in the perpendicular direction. To

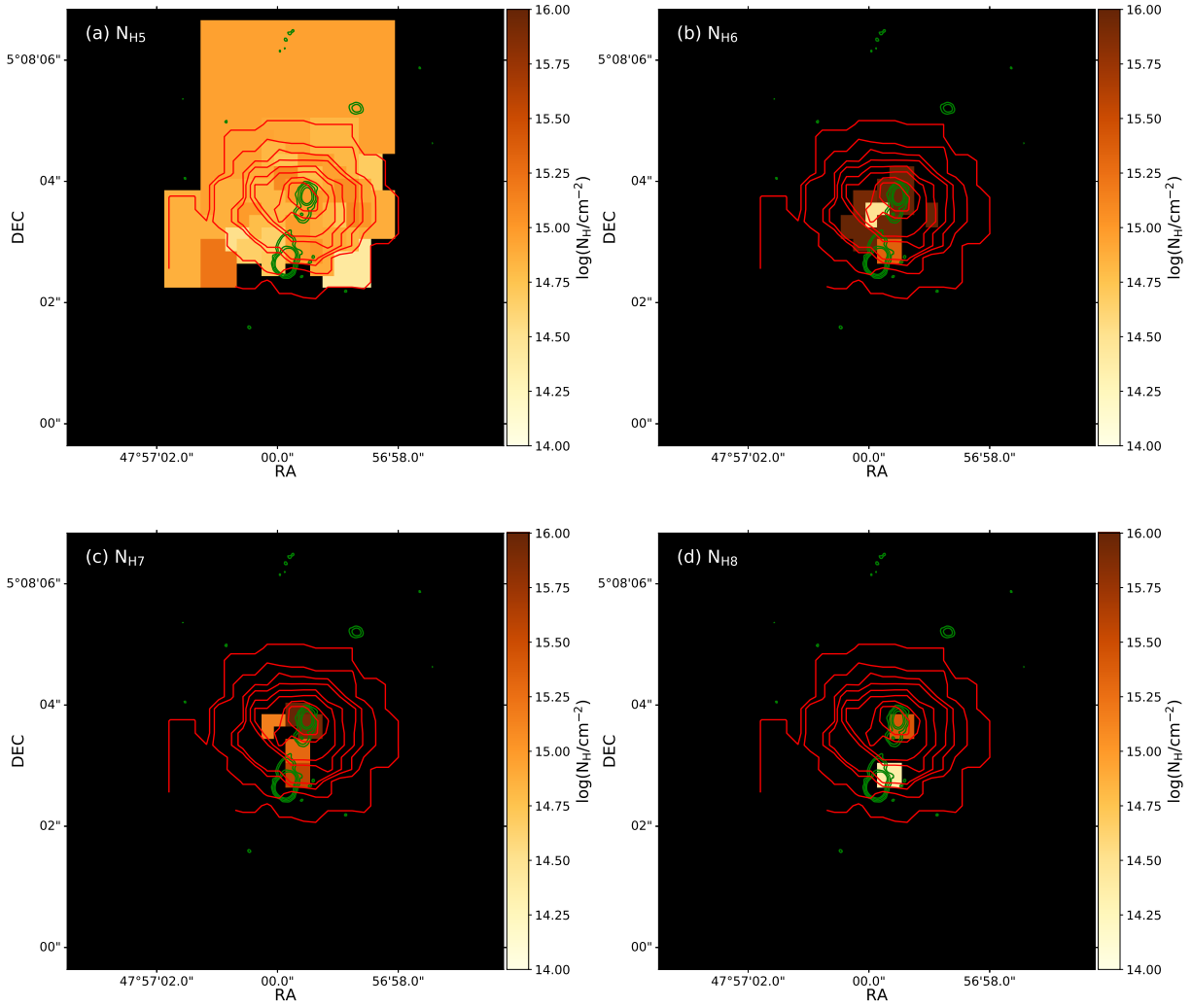

Figure 4.5: The figure presents the fitted column density distributions of absorber 5 (a), 6 (b), 7 (c) and 8 (d). Counters in this figre are the same as Figure 4.2 except the Lyα is shown in red.

interpret the N_H gradient, modeling is needed. For the gradient of Δv_1, we can naively propose that it could be due to rotation or outflows which is aligned with the jet direction. For other absorbers, the column density results are more homogeneous (too little coverage of $6-8$) and the associated velocity maps are noisy.

Chapter 5

Summary and Outlook

5.1 Summary

The objective of this thesis work is to study the morphology and kinematics of the gaseous CGM surrounding HzRGs using MUSE observations to understand the its role and associated mechanisms in galaxy evolution.

In Chapter 1, the theory of galaxy formation and evolution is summarized while the CGM (Section 1.2) and HzRGs (Section 1.3) are introduced to present the motivation of this work. The gaseous medium is accreted to the host galaxy to fuel its star formation and SMBH growth. AGN/star formation activities regulates the evolution of host galaxy through feedback mechanisms. By acting as the source of gas and venue of feedback, CGM draws more and more attentions recently in improving the theory of galaxy evolution. The HzRGs are basically the only type of object where quasar mode and radio mode feedback and host galaxy can be studied simultaneously. Given the aforementioned reasons, we use our HzRGs sample (Section 1.4) to reveal the tip of iceberg of galaxy evolution by focusing the analysis of 4C04.11 (Section 1.5) as a pilot study.

Data observation (Section 2.1) and reduction (Section 2.2) are presented in the Chapter 2. In this Chapter, the details of the data reduction procedure which optimizes the MUSE data reduction and the processes through which the procedure is achieved are presented. We also register the problems encountered in the data reduction in this Chapter as a reminder.

In Chapter 3, we elaborate the fitting procedure (Section 3.2.1) by which we fit the HeII (Section 3.2.2) and Lyα (Section 3.2.3). In this procedure, Gaussian model is used to fit the emission while Voigt is employed to describe the absorption. Unlike many previous work of line fitting, we apply the MCMC method to optimise the result. The fitting results are presented: (i) we obtain the systemic redshift, 4.5079 $\pm$0.0001, from HeII fitting, (ii) a blueshifted broad and an intrinsic narrow emission profiles are identified in each line indi-

cating two gas components with different velocities, (iii) eight absorbers are fitted in Lyα line (Table 3.3). There is degeneracy existing in the preformed fit, high spectral resolution data could eliminate it.

Using an IFS instrument like MUSE, it has the potential to spatially map the emission and absorption properties of 4C04.11. In Chapter 4, we first explain the tessellation method used to improve and homogenize the S/N (Section 4.1). Then, the fitting procedure by which each individual Lyα spectrum is fitted is presented (Section 4.2). The mapping results are shown in Figure 4.2 − 4.5 while primary interpretations are given in Section 4.4. One of the more remarkable results is that we identify column density gradient of the absorber 1 (Δv ~ 0 km s^{-1}, Figure 4.3) for which the physical interpretation is unclear yet.

5.2 Outlook

As elaborated at several occasions throughout, this master thesis work studies the galaxy formation and evolution in general and has many potential aspects to follow.

For our source, 4C04.11, the MUSE data analysis is incomplete. CIV lines will be fitted with the same procedure (Section 3.2.1). Given its S/N, the spatial mapping could also be possible for CIV which will be a valuable result of CGM enrichment study.

The similar tasks described in this work can also be applied to all of our eight targets to produce a statistic study of HzRGs absorption. For all our sources, ALMA data is also available (PI: De Breuck) through which the muli-phase properties of CGM could be studied.

With the results of observation obtained, we can compare them to cosmological simulations to investigate whether the observation can be reproduced by simulation or more theoretical works needed to complete the simulation.

The Lyα halos are not unique around HzRGs (= Type II AGN). They are common features in high-z Universe (e.g. Cantalupo et al., 2012; Wisotzki et al., 2018). We can link our analysis to the study of gaseous CGM around other objects (e.g. Type I AGN) to obtain a complete picture of galaxy evolution.

For my PhD thesis, I will continue working on the topic about galaxy evolution and feedback effects. The aforementioned aspects will be studied and be parts of it.

Appendix A

AUTOCAL_FACTORS Individual Exposure Checking

In this Appendix, the AUTOCAL_FACTORS which are the products of the Self-Calibration procedure described in Section 2.2.3 are presented to check whether there is some unusual correction. The following figures (Figure A.1 - Figure A.8) are plotted by plot_autocal_factors function in *mpdaf*. In each of the figures, the correct factors of each wavelength segments and each IFUs are shown. By examining the field of view visually, 4C04.11 located approximately on IFU 13, 14, 15 and 16 with Lyα seats in the 9th wavelength segment (marked as vertical red dash line). It can be seen from examining the 8 figures that the correction factors of the target location and Lyα wavelength are relatively small which indicates the Self-Calibration in the reduction process is satisfied. These plots are derived in the production process of the 6th CUBE which is determined to be the one with the most satisfied performance.

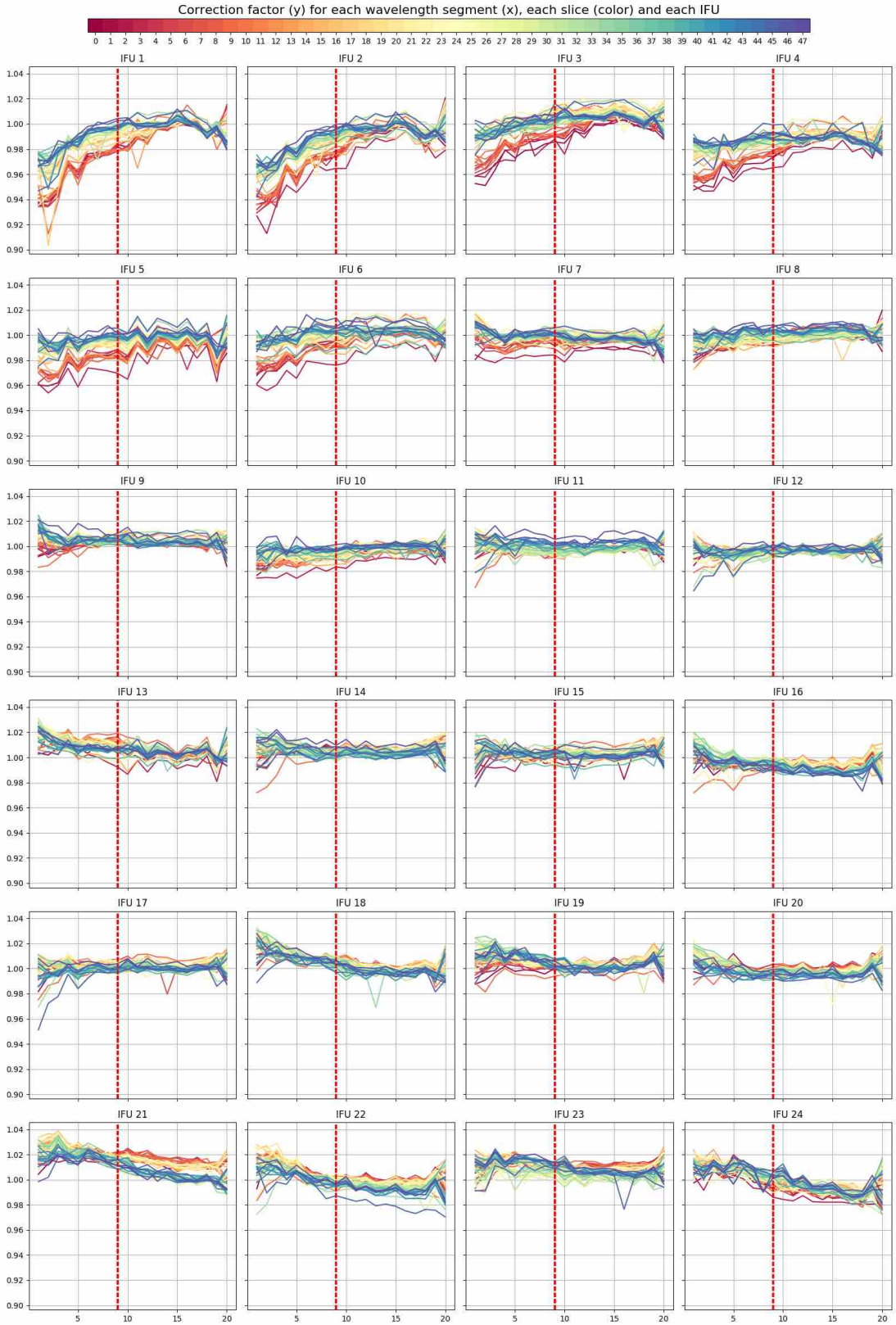

Figure A.1: The AUTOCAL_FACTORS (correction factors) for each IFUs and wavelength sections of exposure 1.

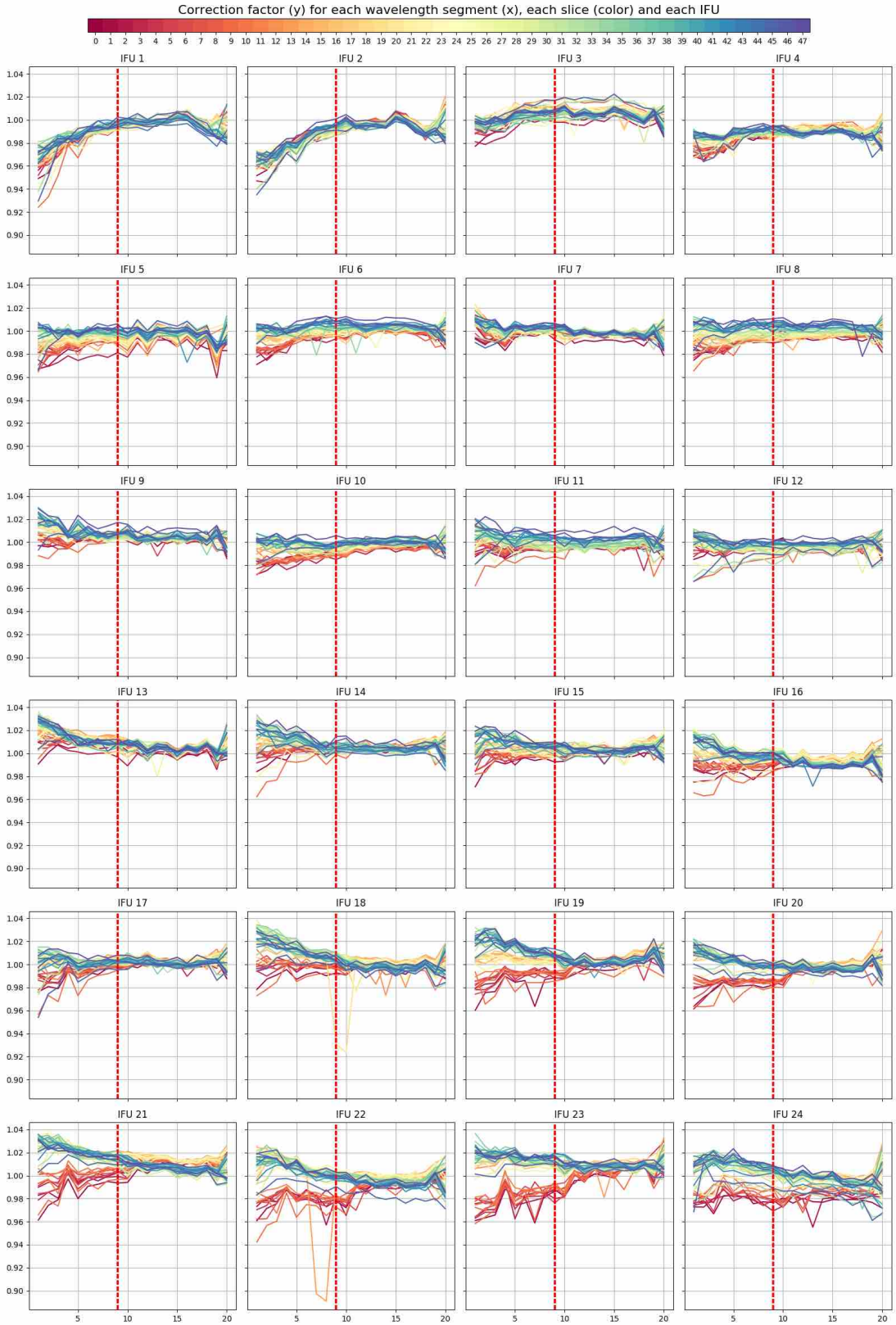

Figure A.2: The correction factor for exposure 2.

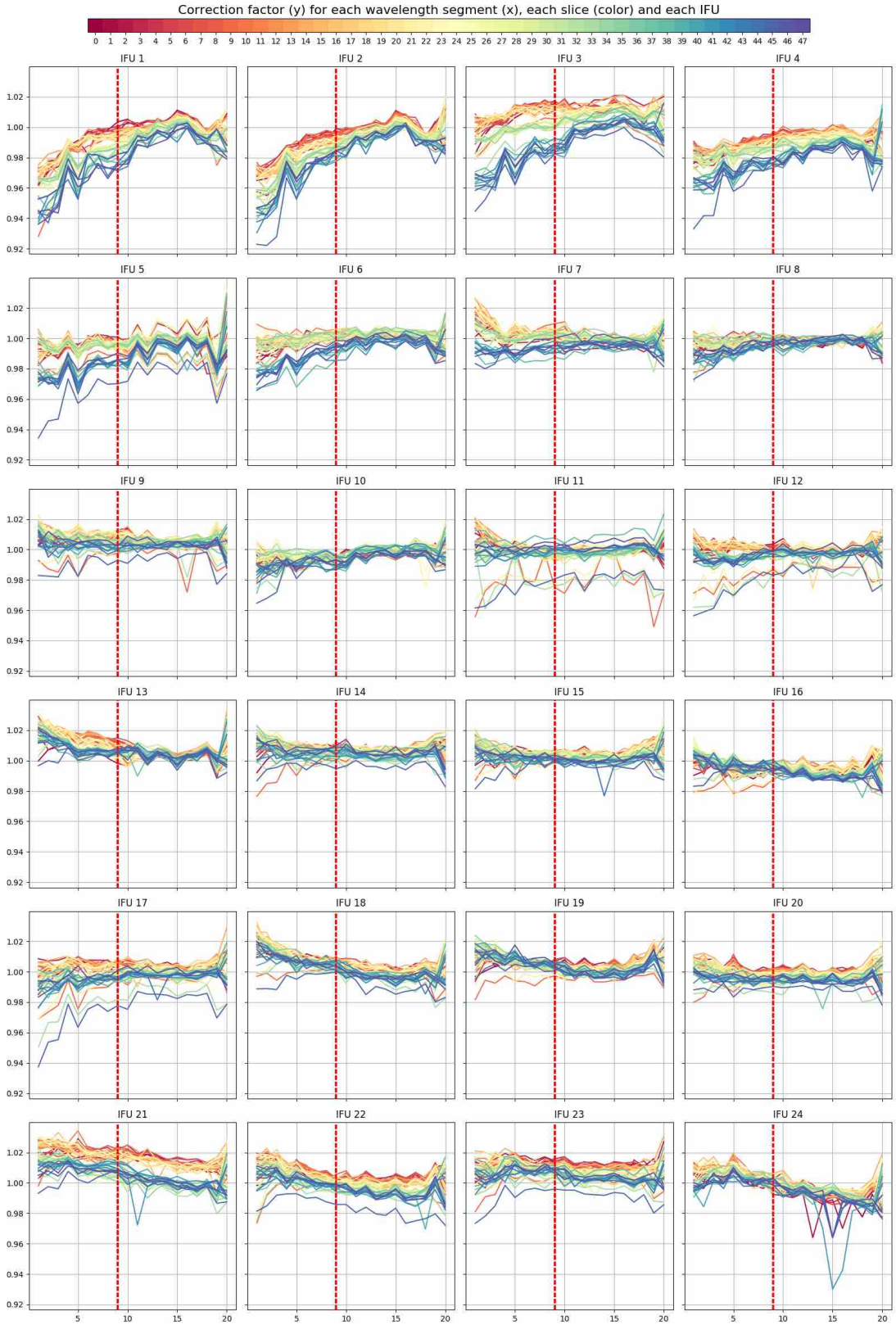

Figure A.3: The correction factor for exposure 3.

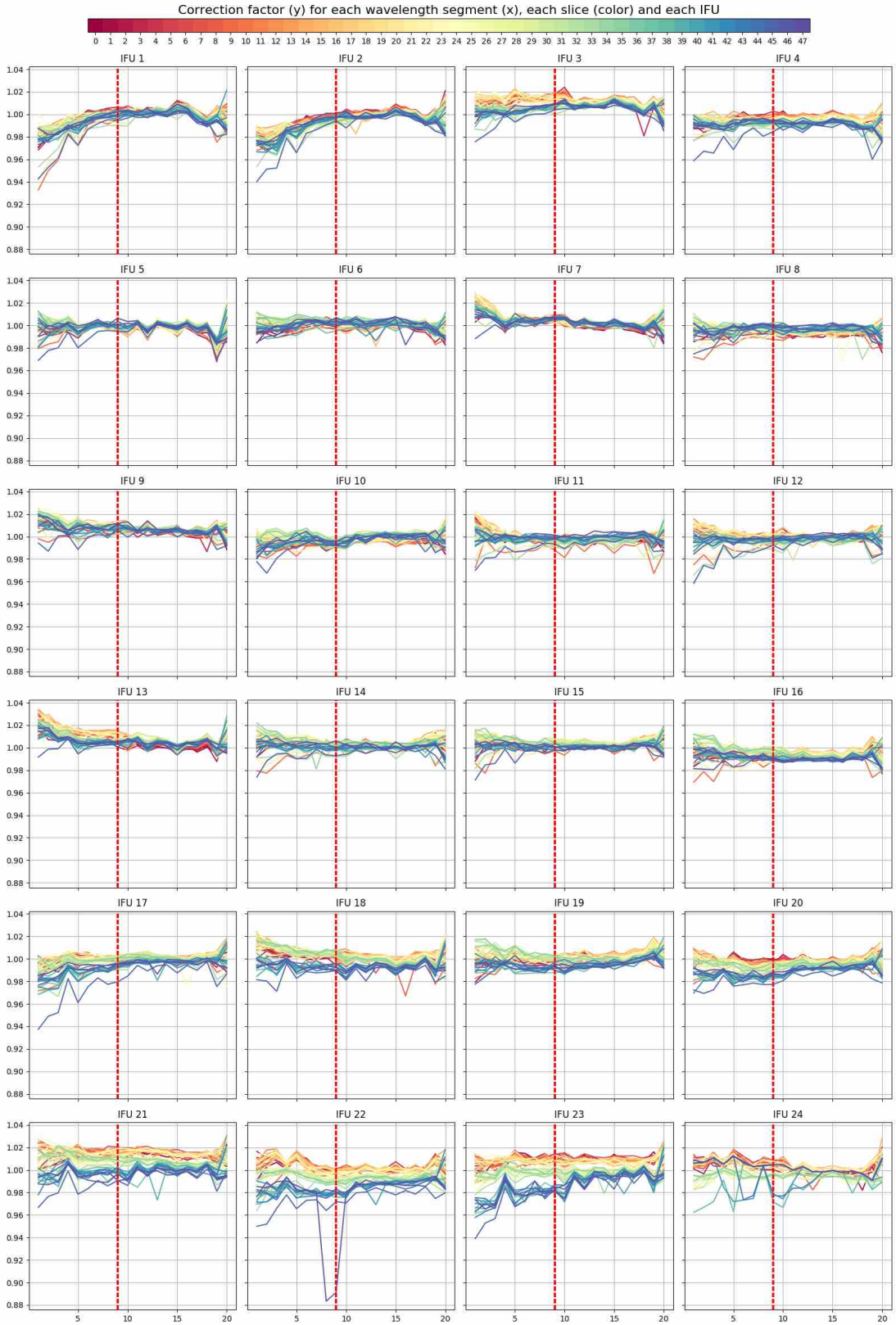

Figure A.4: The correction factor for exposure 4.

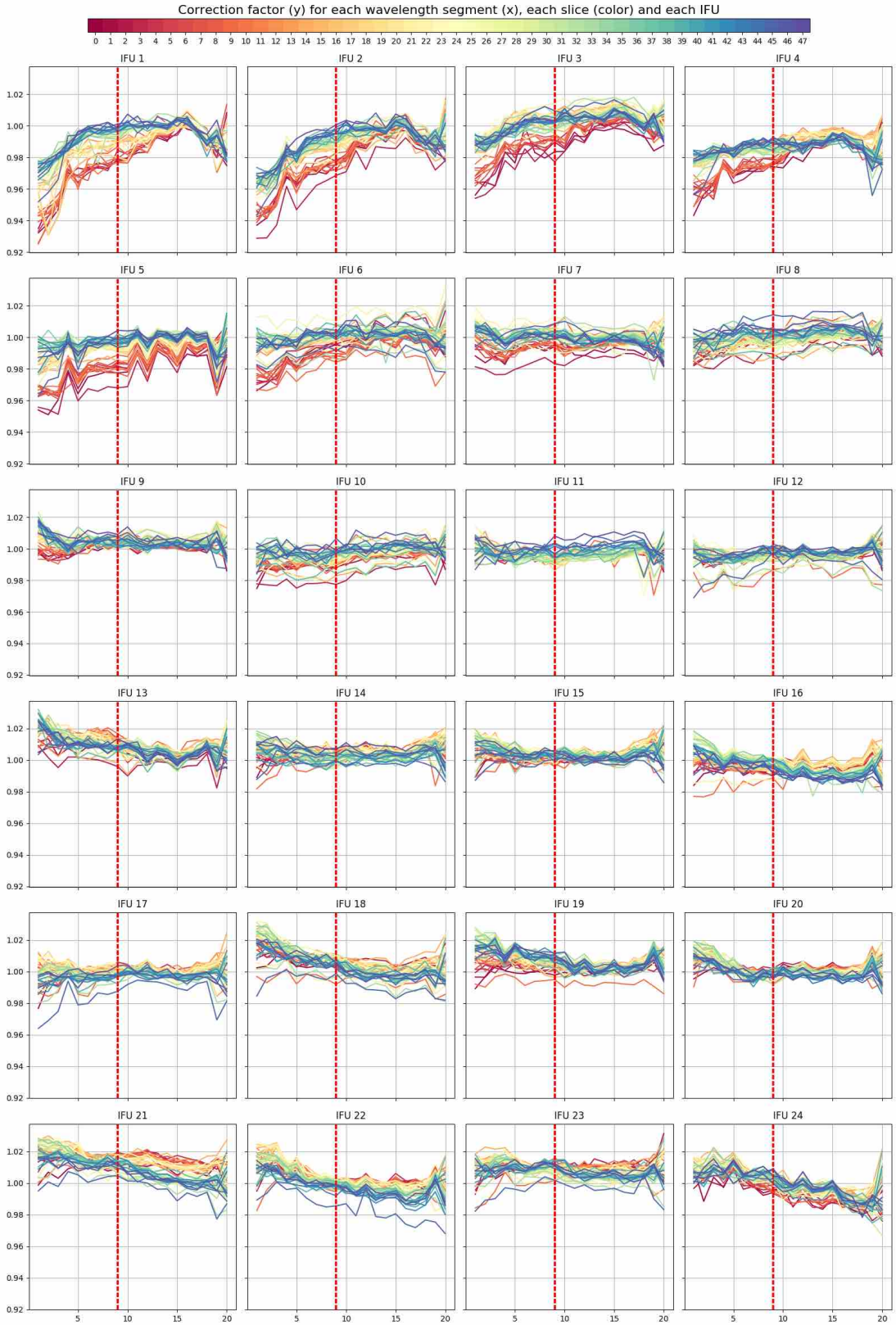

Figure A.5: The correction factor for exposure 5.

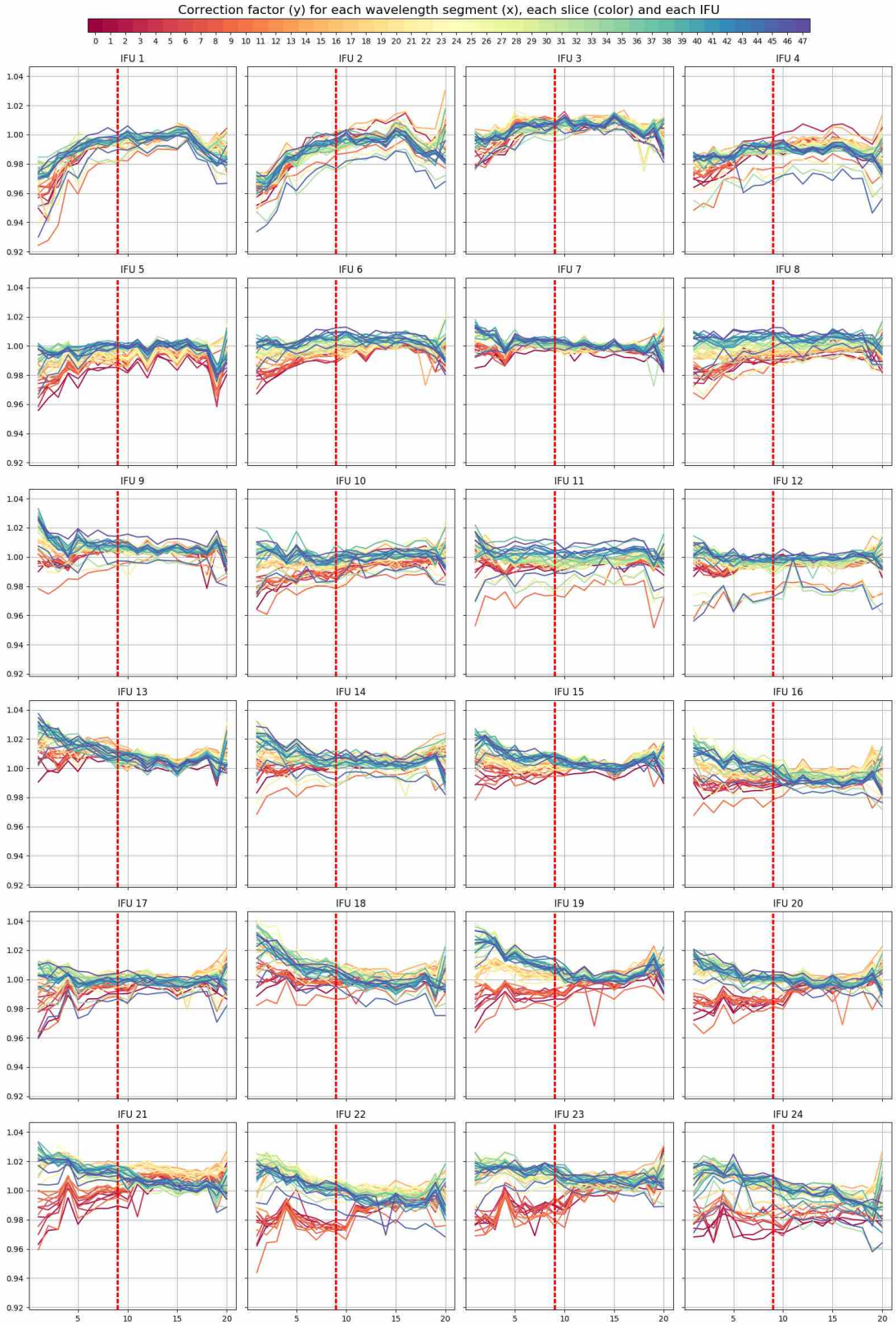

Figure A.6: The correction factor for exposure 6.

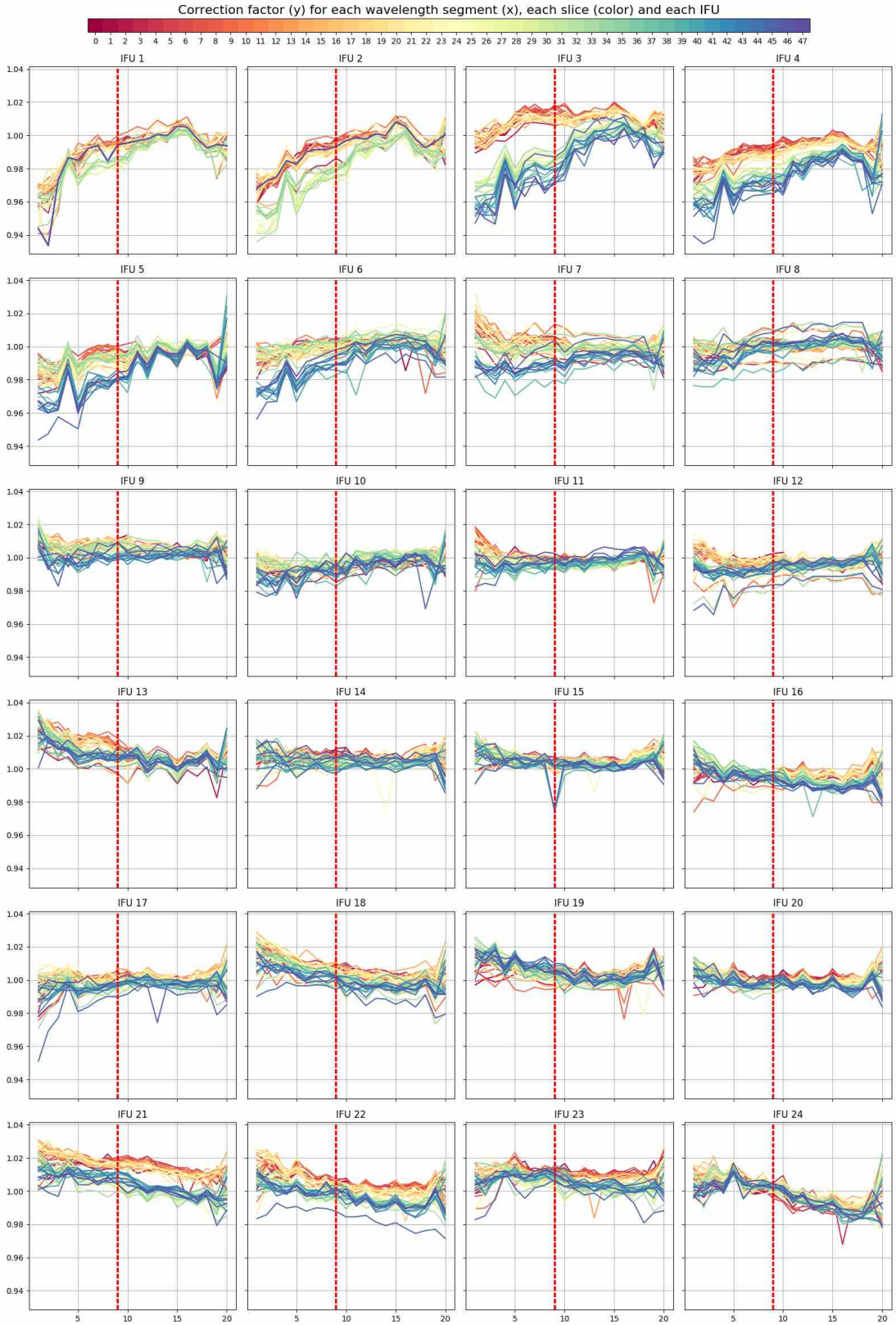

Figure A.7: The correction factor for exposure 7.

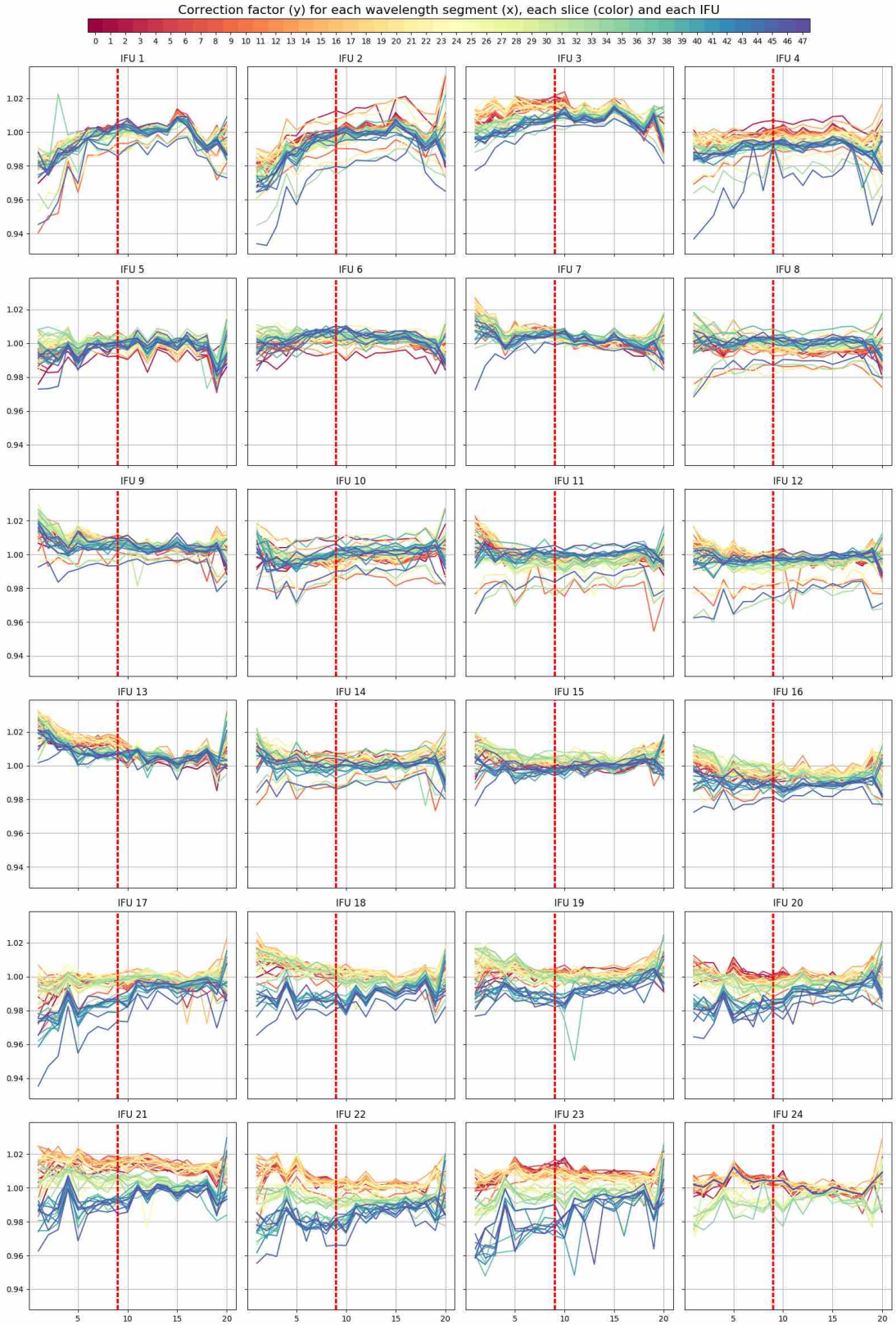

Figure A.8: The correction factor for exposure 8.

Appendix B

Spectra and S/N Comparison Between Eight Reduction Methods

In this appendix, we present the results of the performance comparison among the 8 CUBEs. The description of the CUBE production and naming is demonstrated in Section 2.2.2. The wavelength of the 4 bands are described in Section 2.2.4. The pair comparison are shown in Figure B.1 to Figure B.8.

It is shown in Figure B.1 that spectra derived by using pipeline do the sky subtraction are less noisy and have higher flux values in band 1. There is no apparent difference between the spectra shown in Figure B.2 which is the wavelength band of Lyα. This is reasonable considering the flux density at peak of the Lyα line has approximately a factor of 20 higher than the one in the continuum which shows that the 8 production methods perform similarly in high signal region. Similarly, in Figure B.3, the spectra with "pipesky" are less noisy. Finally, in Figure B.4, the spectra from with "pipesky" are less noisy in the continuum while have similar performances at the region of the emission lines.

For the S/N comparison, there is no clear differences in band 1 shown in Figure B.5. In first three panels of Figure B.6, however, the S/N from the spectra with "pipesky" are higher at the peak of the Lyα line. The S/N of the spectra with "pipesky" are higher in Figure B.7 and B.8.

With the above comparison, it is obvious that the 4 CUBEs with pipeline doing the sky subtraction perform well, namely CUBE 4th, 5th, 6th and 8th. Hence, we implement the same exercise to these 4 CUBEs next. This time the 3 spectra namely 4th, 5th and 6th CUBEs combined with CubeList and the 3 corresponding S/N are compared together in each of the 4 wavelength bands. Then the one with the best performance is compared with the spectra from the 8th CUBE in all 4 bands.

In Figure B.9 to B.12, it is obvious that the spectra, "mpdaf, pipesky, median", is the most noisy one while the "mpdaf, pipesky, mad" and "mpdaf, pipesky, sigma clip" perform similarly. To discriminate between the 5th and 6th, we change the plotting order and compare carefully. In band 3 and 4, the spectra of 6th spectra is less noisy than the 5th to a small extend. Furthermore, the MAD and sigma clipling are alike methods despite the MAD uses median value instead of mean value. It is less biased by extreme values comparing to sigma clip. Therefore, we think the 6th CUBE performs the best among the first six despite its spectra are similar to the 5th visually. Then we compare it with the 8th CUBE, it is obvious that in Figure B.14 the S/N is lower for CUBE 8th, and similarly, in other three bands, the S/N for 8th are lower than the 6th. Based on this examination, we conclude that the 6th CUBE produced by using pipeline doing the sky subtraction and combination with CubeList performs the best among the eight.

* Figure B.1 Caption. The performance comparison between spectra extracted from the 8 CUBEs in band 1. The colors used here are identical to those in Figure 2.2. The flux density unit used in the figures appendix is 10^{-17} erg s^{-1} Å cm^{-2}. **First panel**: The spectra from the 1st and 4th CUBEs; **Second panel**: The spectra from the 2nd and the 5th CUBEs; **Third panel**: The spectra from the 3rd and 6th CUBEs; **Forth panel**: The spectra from the 7th and 8th CUBEs.

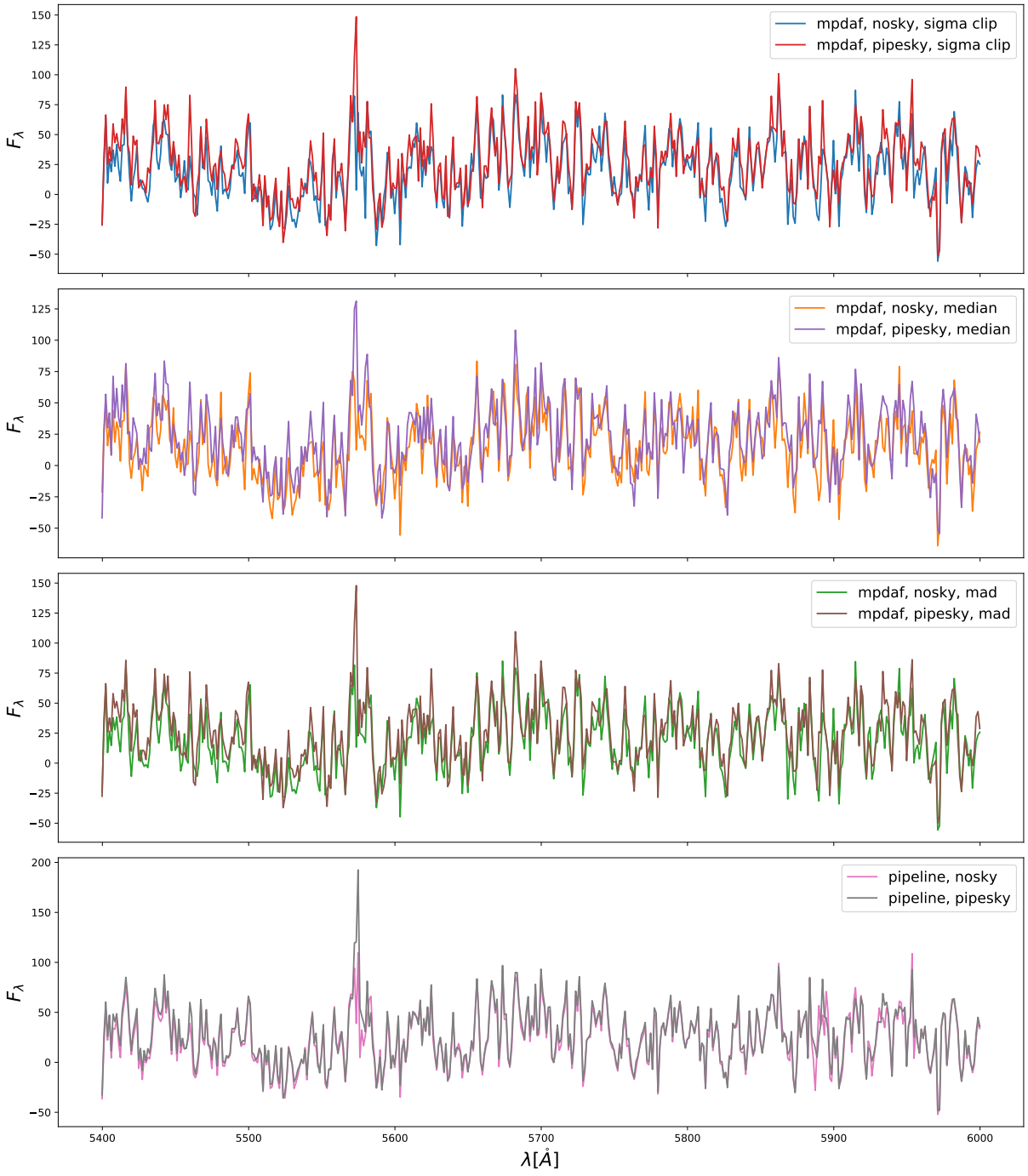

Figure B.1: Caption shown in the text due to the limited space.*

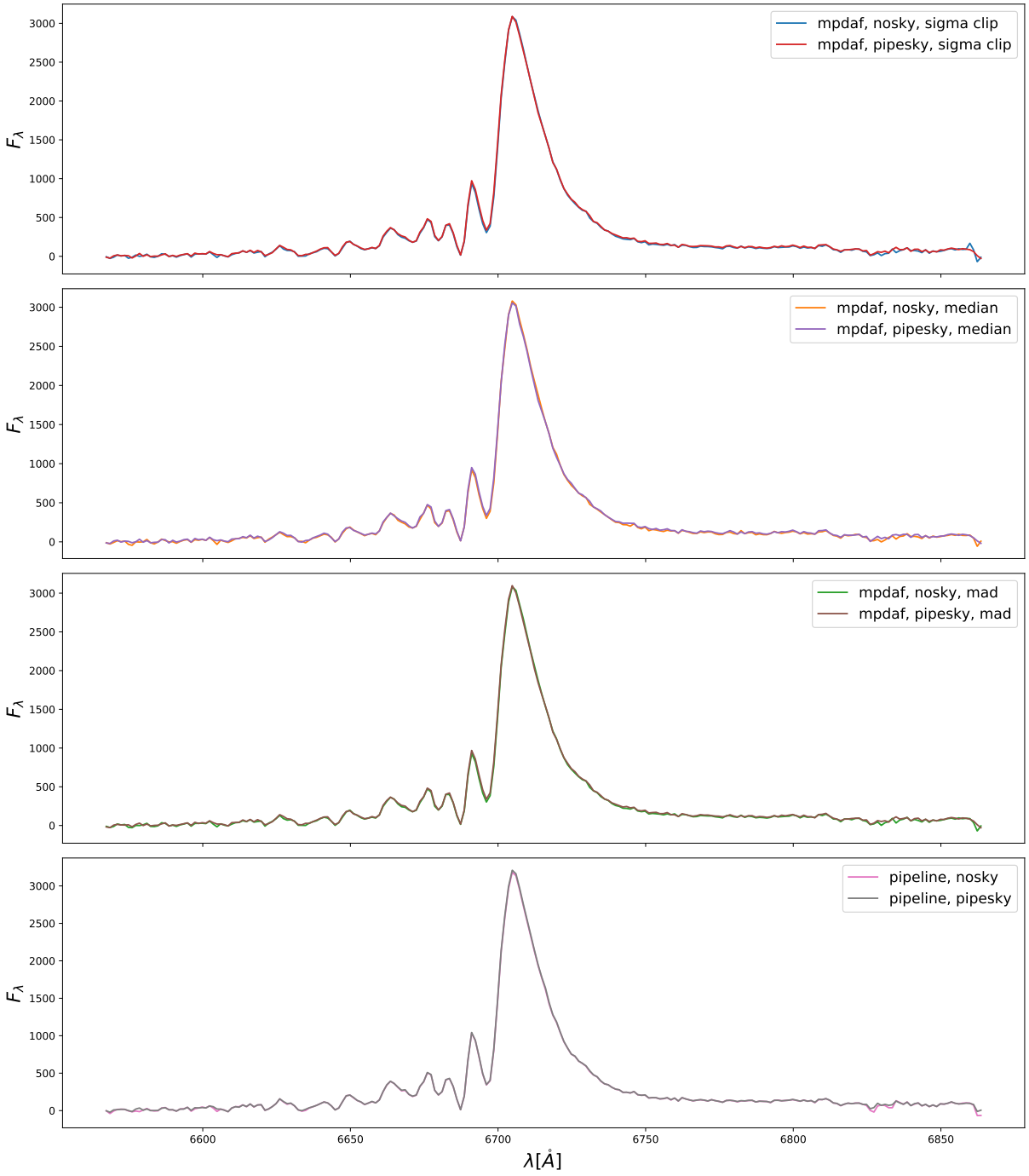

Figure B.2: The performance comparison between spectra extracted from the 8 CUBEs in band 2. Spectra in each panels are from the same CUBEs in the corresponding panels described in Figure B.1.

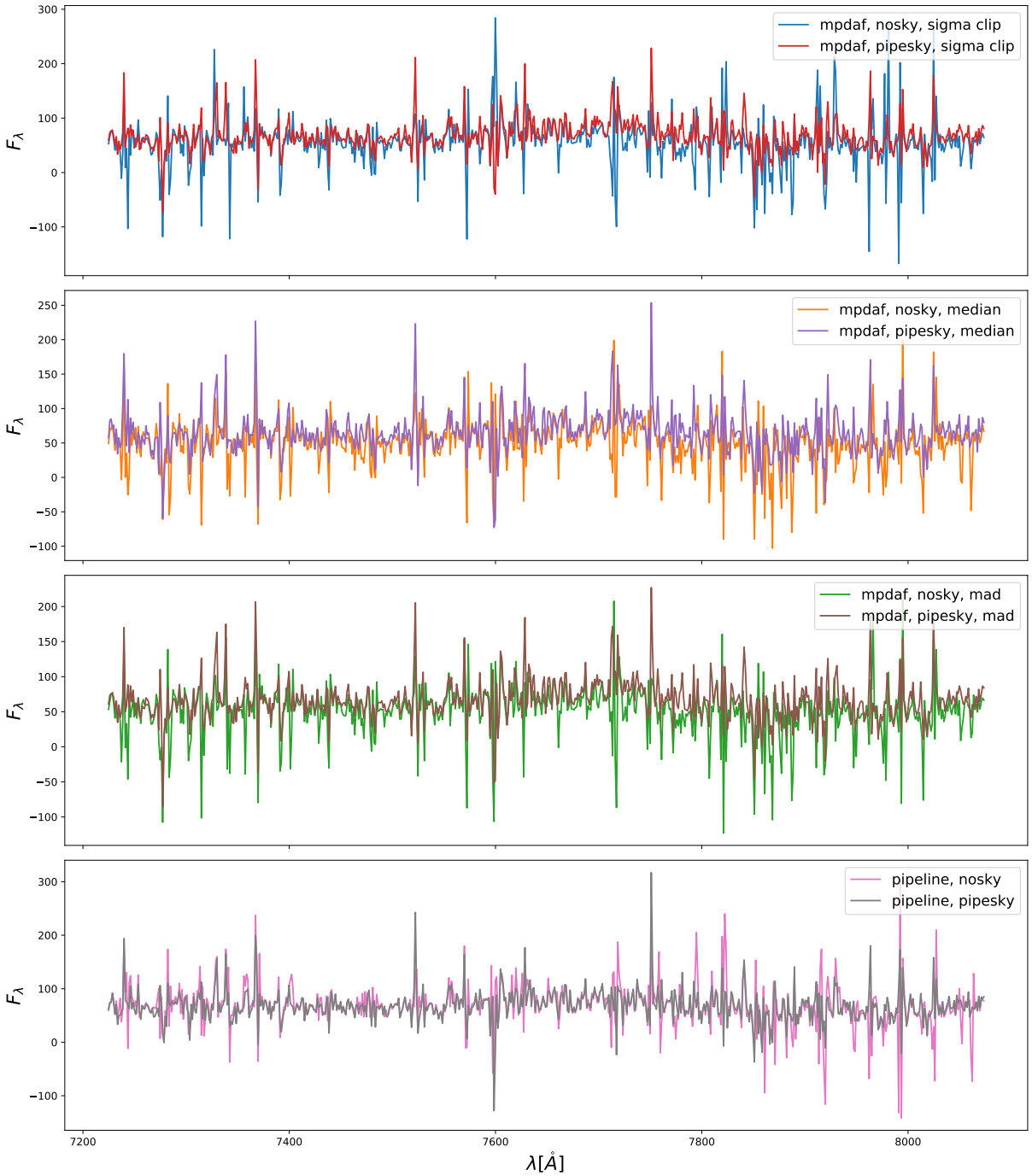

Figure B.3: The performance comparison between spectra extracted from the 8 CUBEs in band 3. Spectra in each panels are from the same CUBEs in the corresponding panels described in Figure B.1.

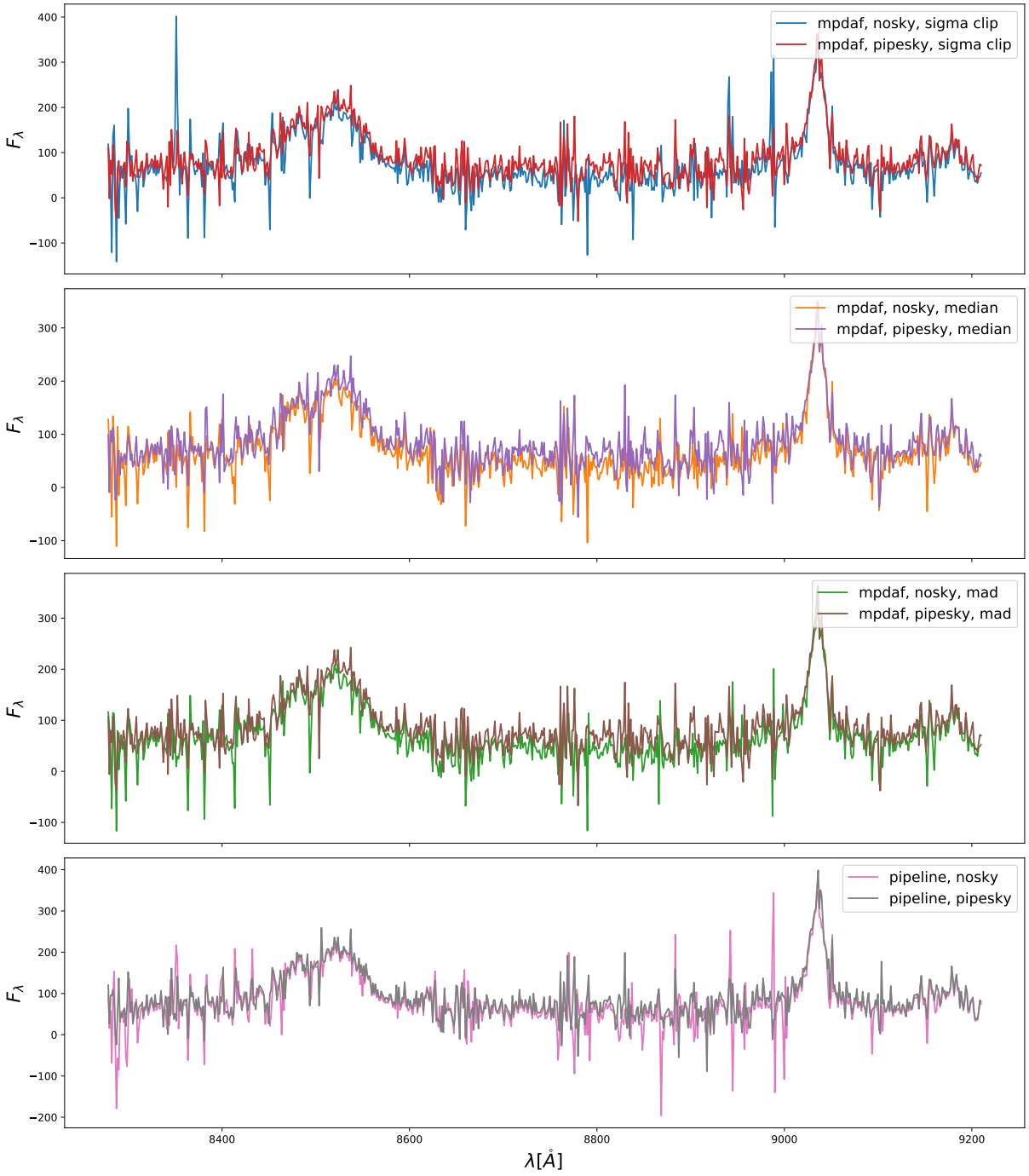

Figure B.4: The performance comparison between spectra extracted from the 8 CUBEs in band 4. Spectra in each panels are from the same CUBEs in the corresponding panels described in Figure B.1.

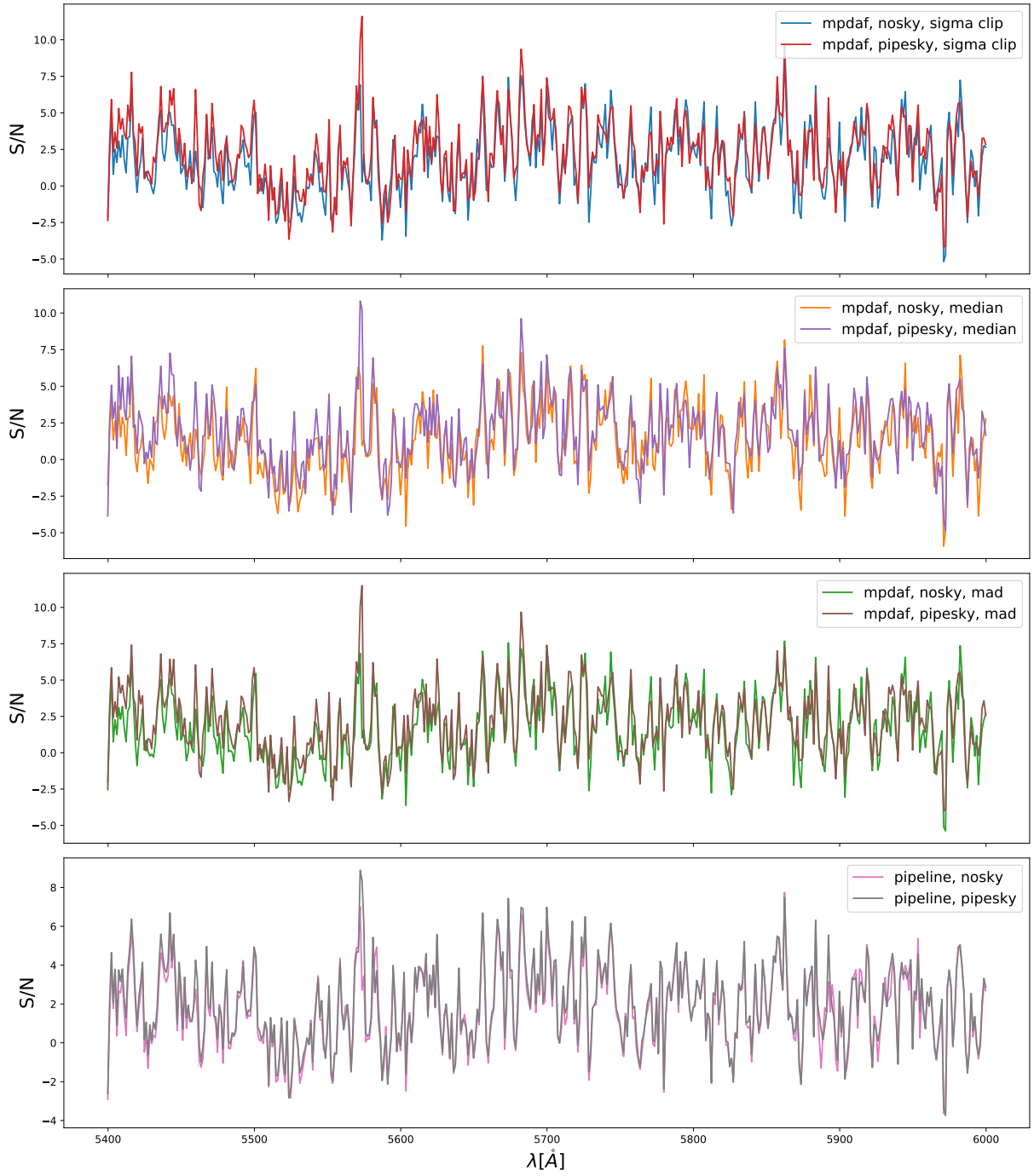

Figure B.5: The performance comparison between the S/N of the spectra extracted from the 8 CUBEs in band 1. S/N in each panels are derived from the spectra in the corresponding panels described in Figure B.1.

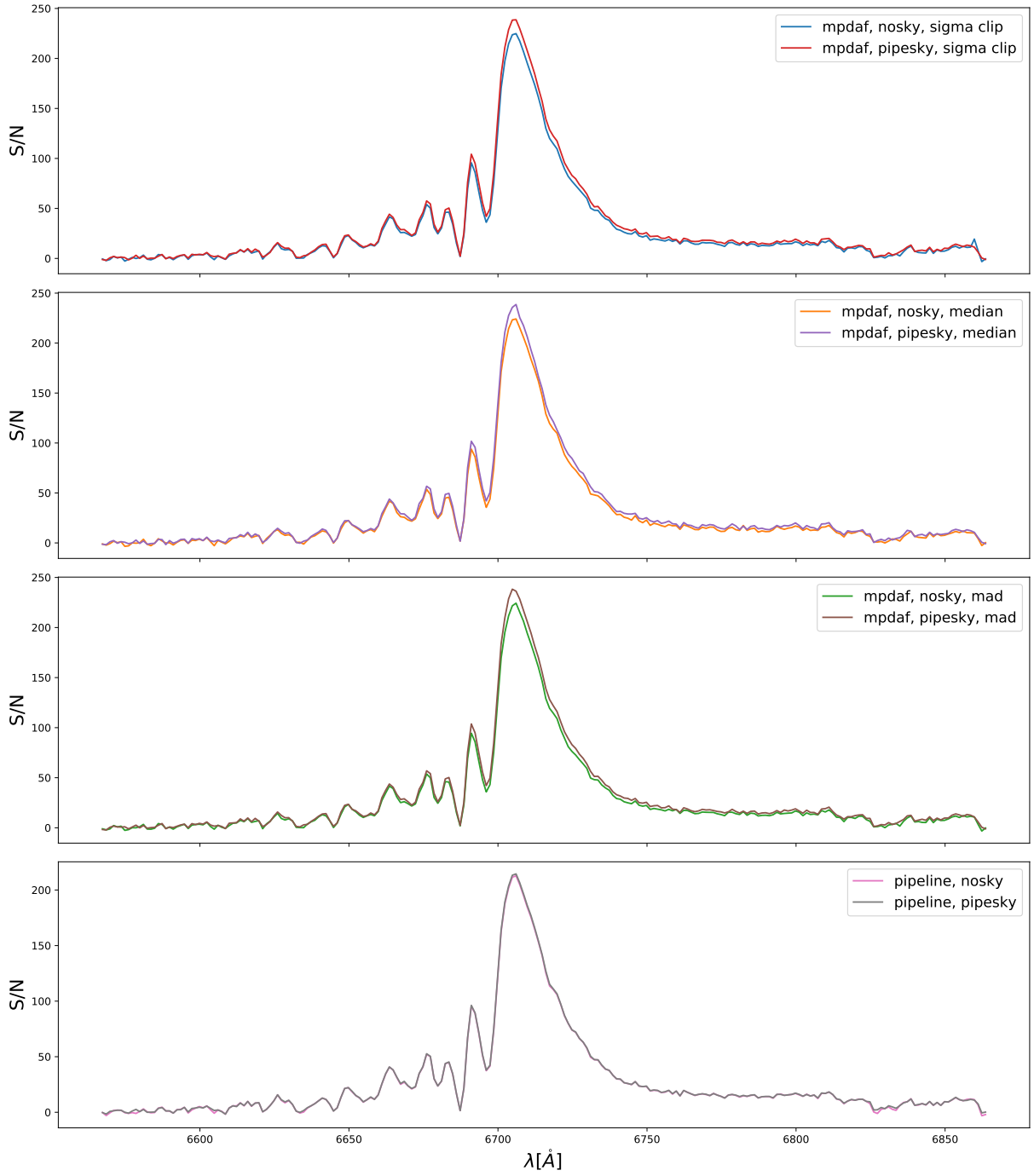

Figure B.6: The performance comparison between the S/N of the spectra extracted from the 8 CUBEs in band 2. S/N in each panels are derived from the spectra in the corresponding panels described in Figure B.2.

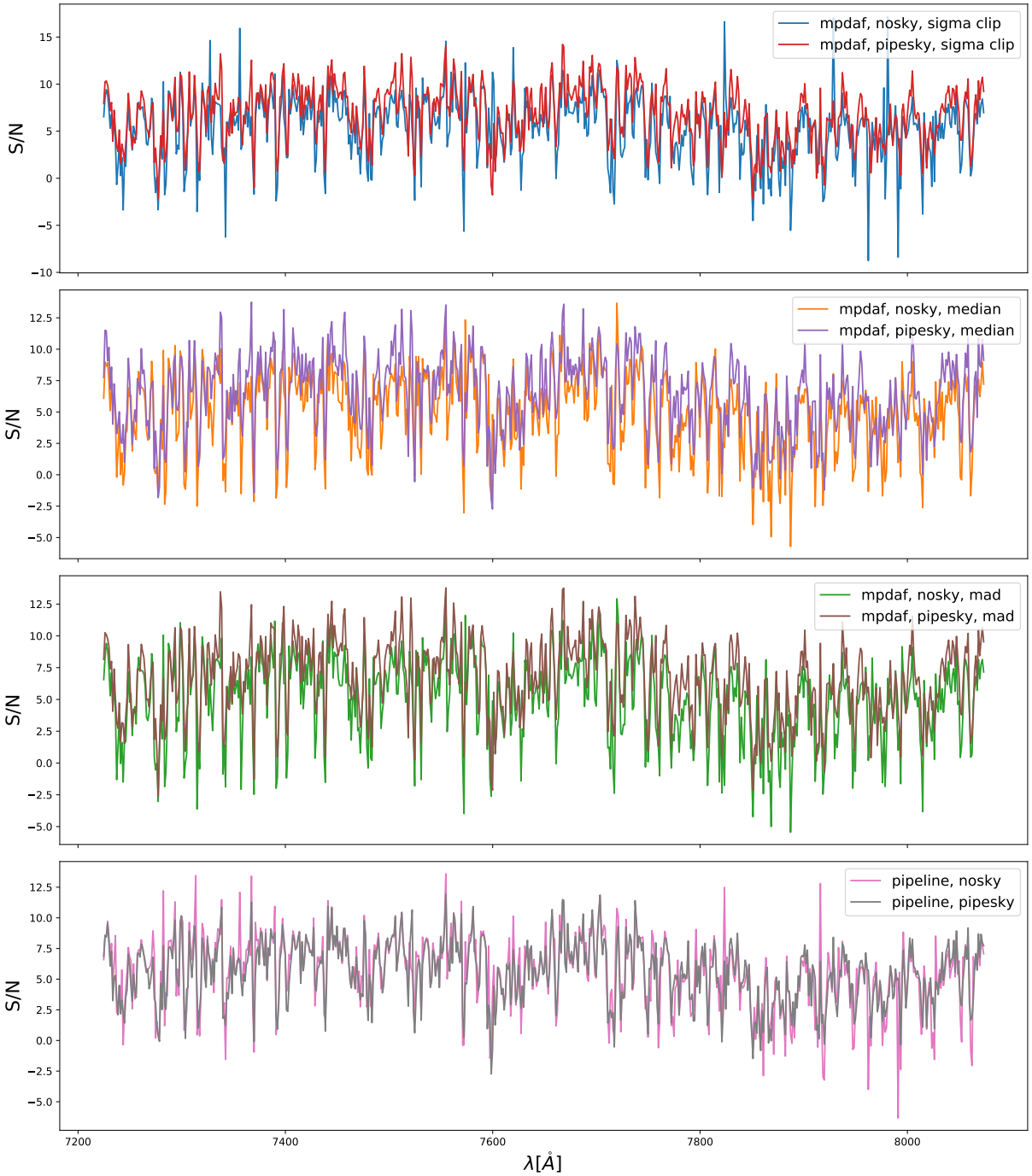

Figure B.7: The performance comparison between the S/N of the spectra extracted from the 8 CUBEs in band 3. S/N in each panels are derived from the spectra in the corresponding panels described in Figure B.3.

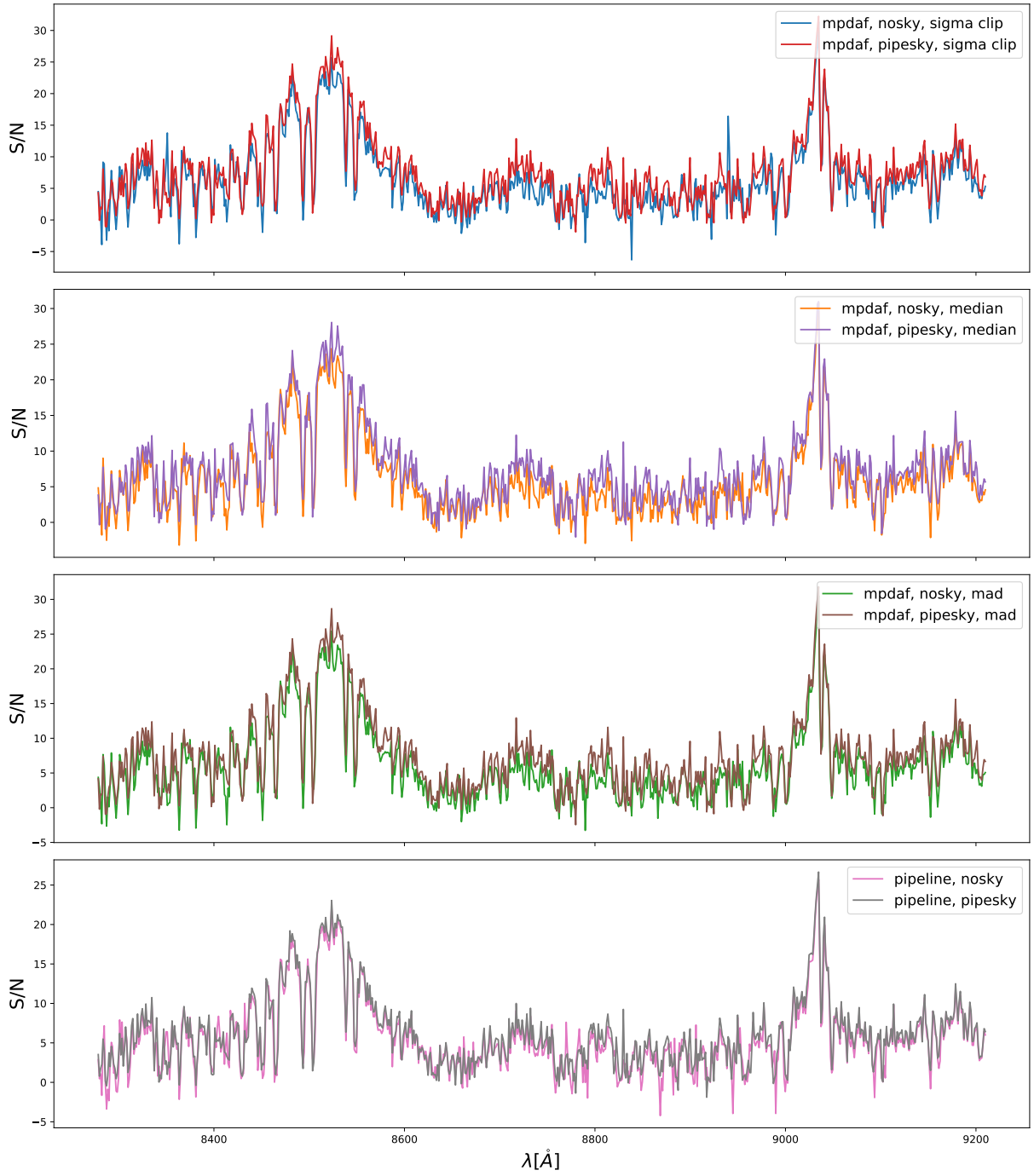

Figure B.8: The performance comparison between the S/N of the spectra extracted from the 8 CUBEs in band 4. S/N in each panels are derived from the spectra in the corresponding panels described in Figure B.4.

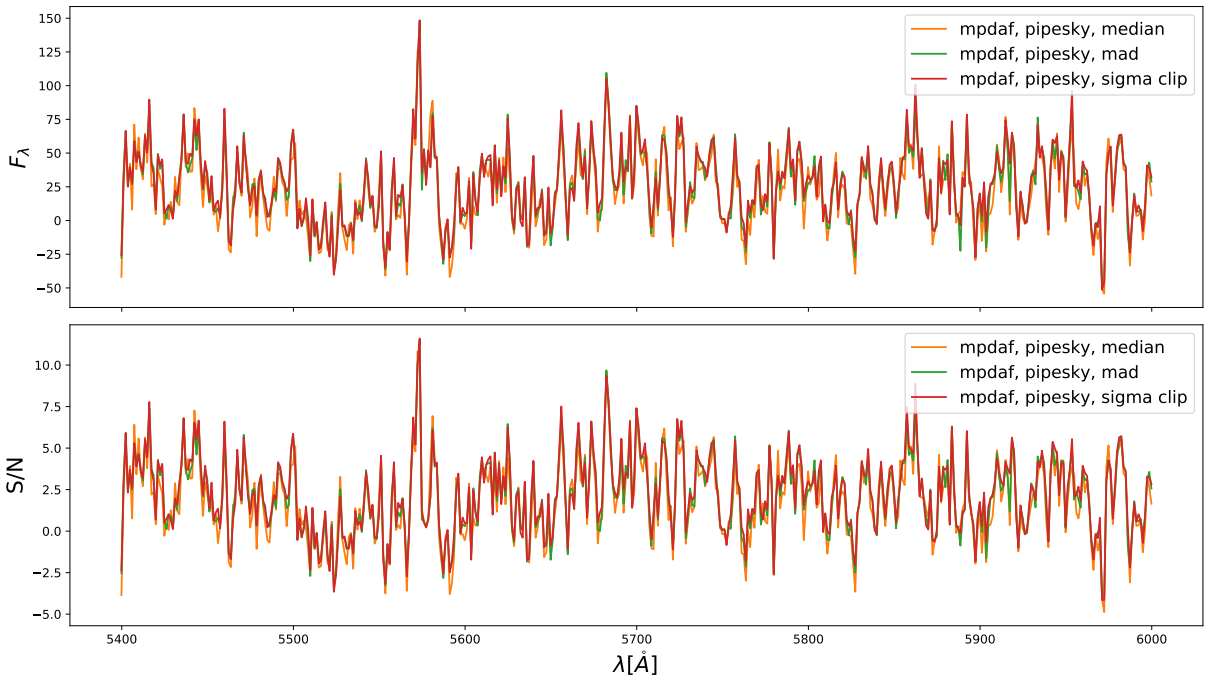

Figure B.9: The spectra and corresponding S/N from CUBEs 4th, 5th and 6th comparison in band 1. The spectra colors used in this figure are *not* the same ones previously used for the reason of discrimination.

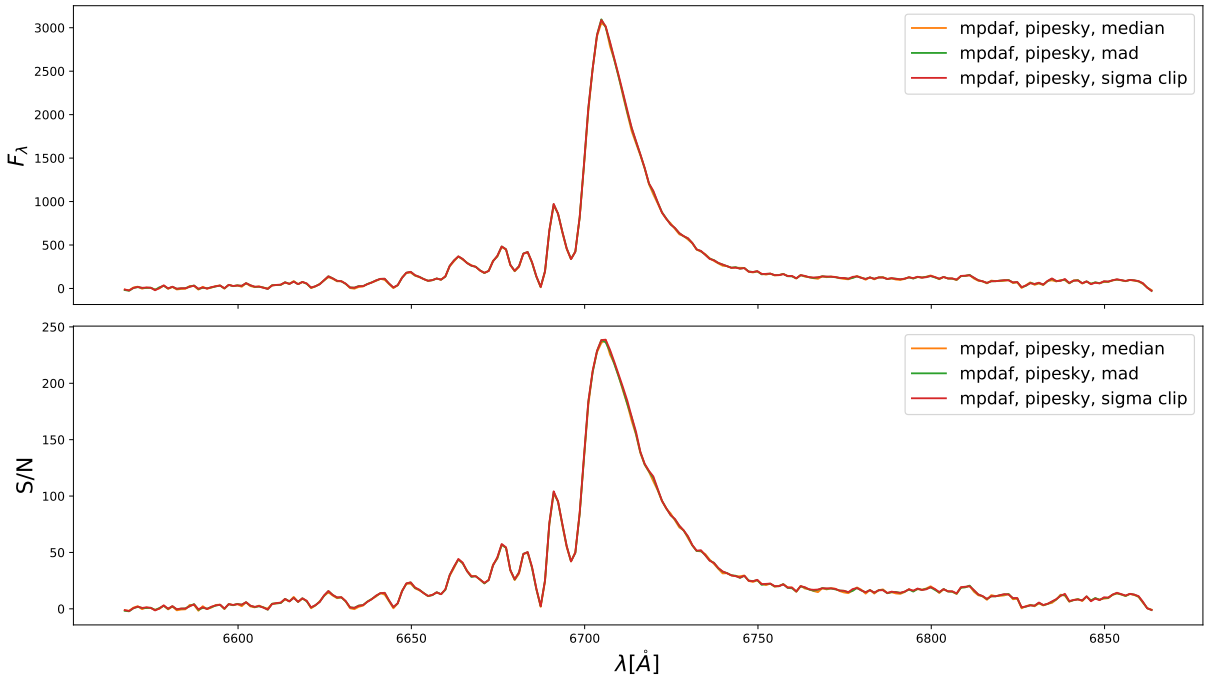

Figure B.10: The spectra and corresponding S/N from CUBEs 4th, 5th and 6th comparison in band 2.

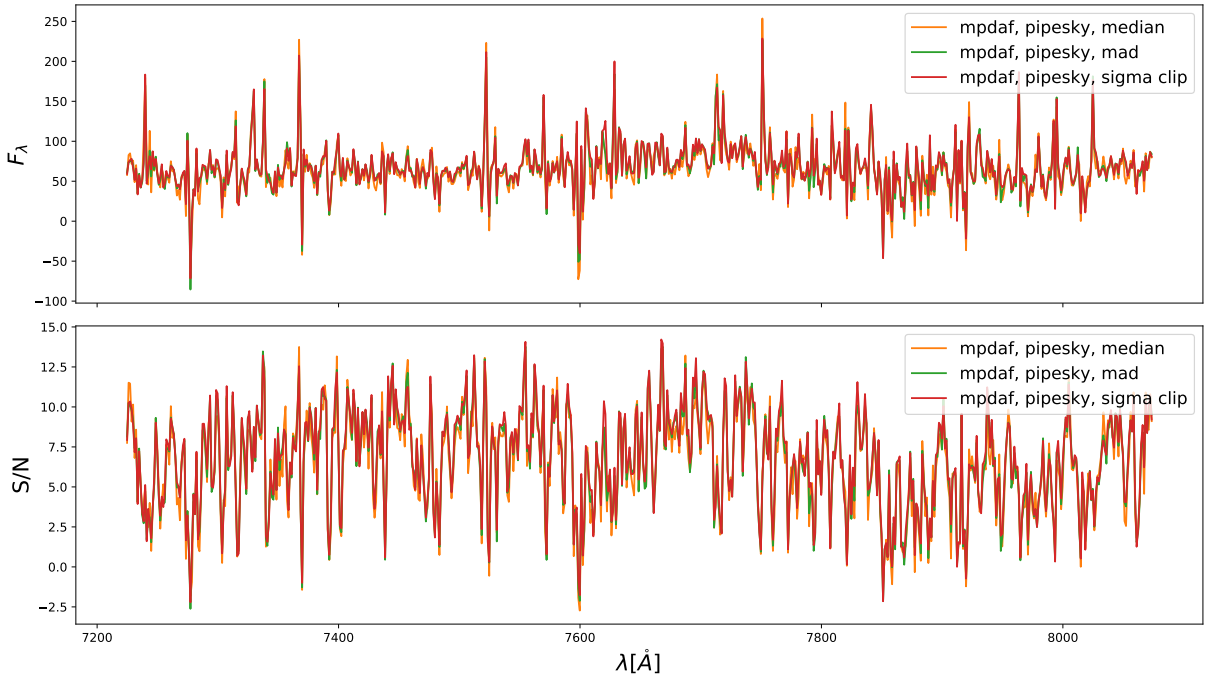

Figure B.11: The spectra and corresponding S/N from CUBEs 4th, 5th and 6th comparison in band 1.

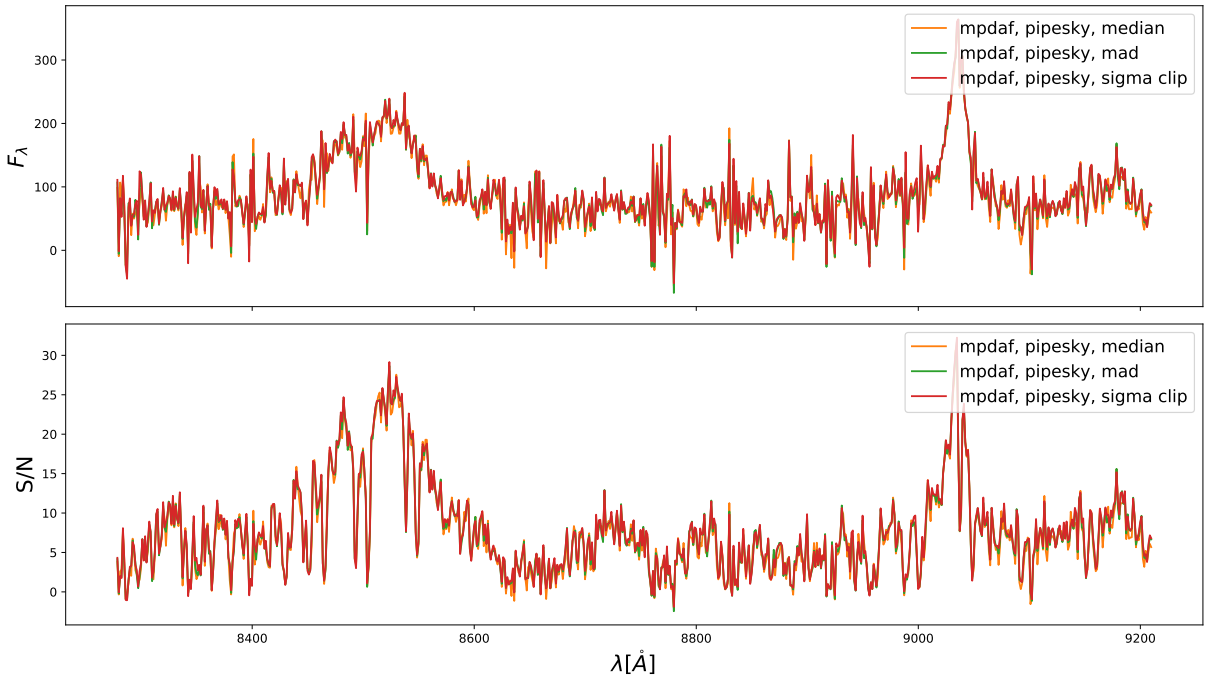

Figure B.12: The spectra and corresponding S/N from CUBEs 4th, 5th and 6th comparison in band 4.

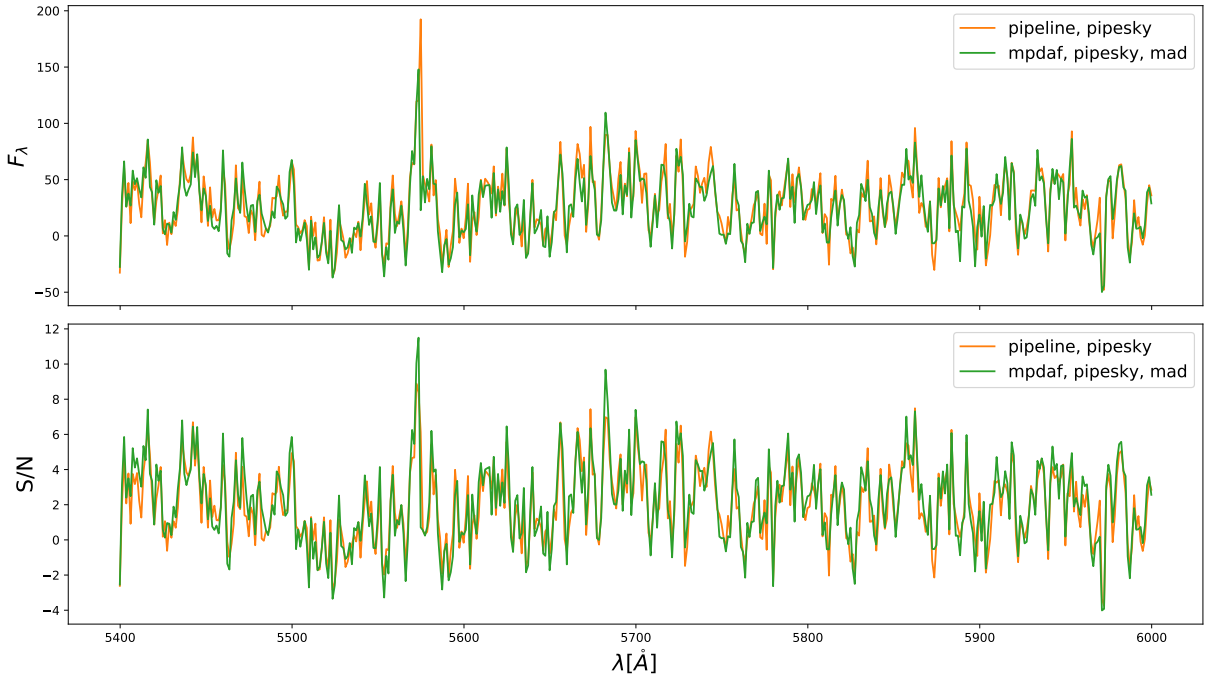

Figure B.13: The spectra and corresponding S/N from CUBEs 6th and 8th comparison in band 1.

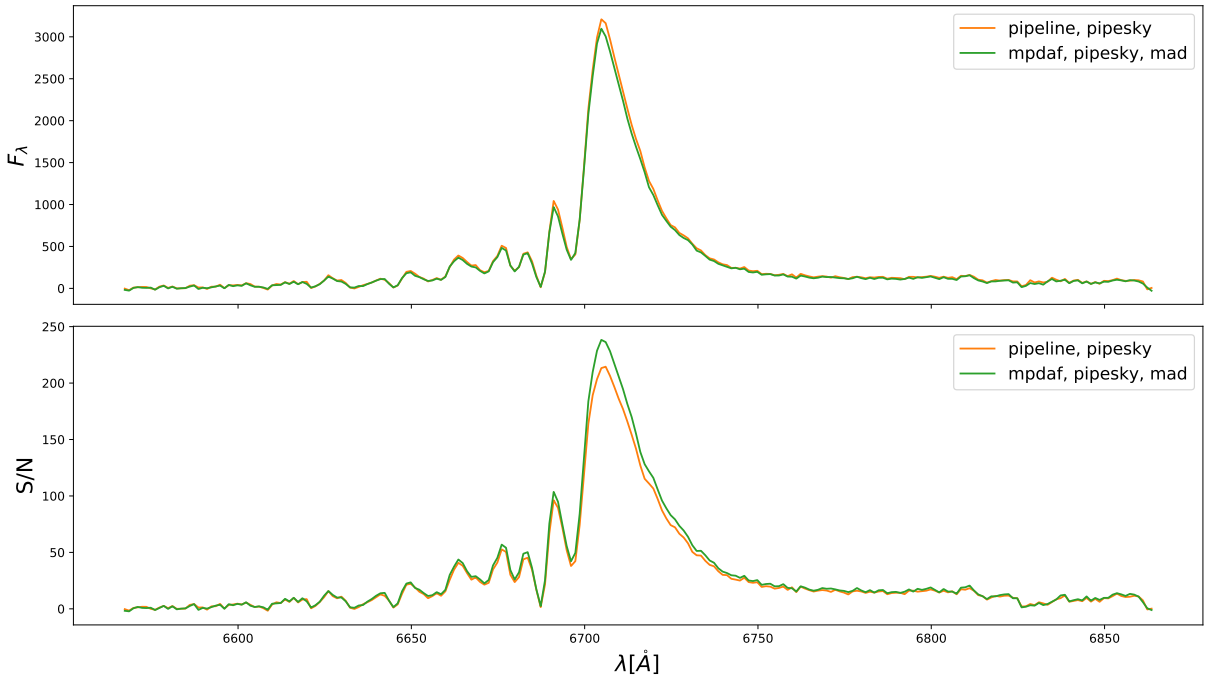

Figure B.14: The spectra and corresponding S/N from CUBEs 6th and 8th comparison in band 2.

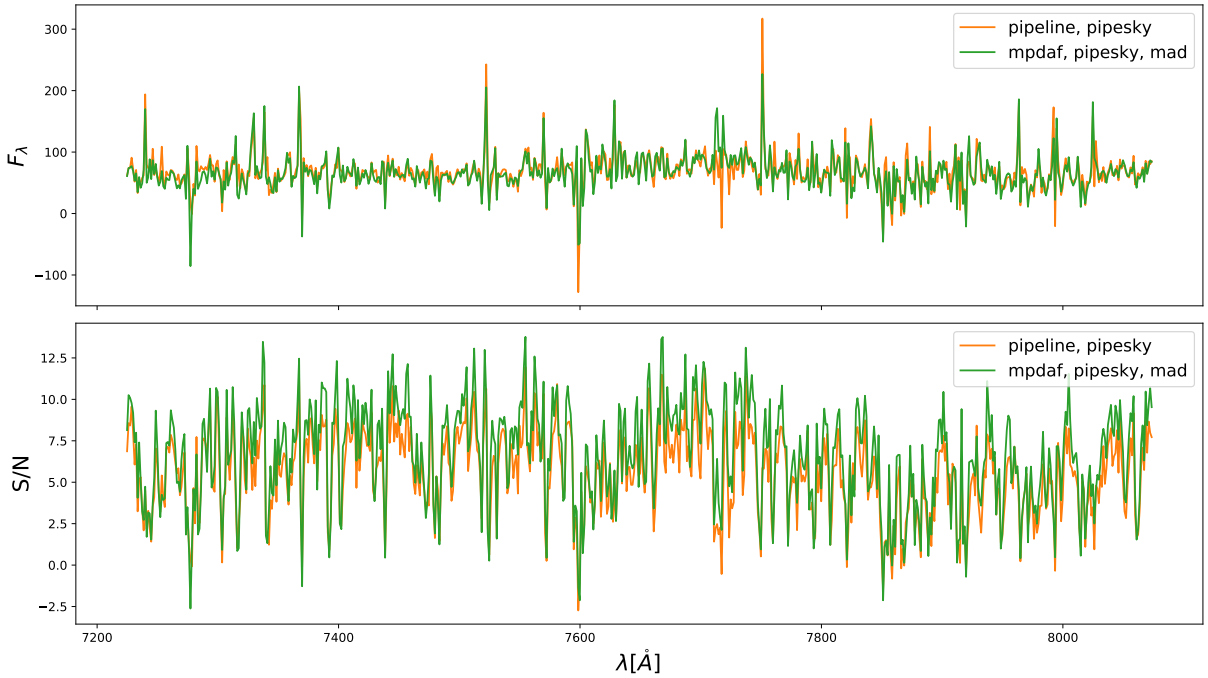

Figure B.15: The spectra and corresponding S/N from CUBEs 6th and 8th comparison in band 3.

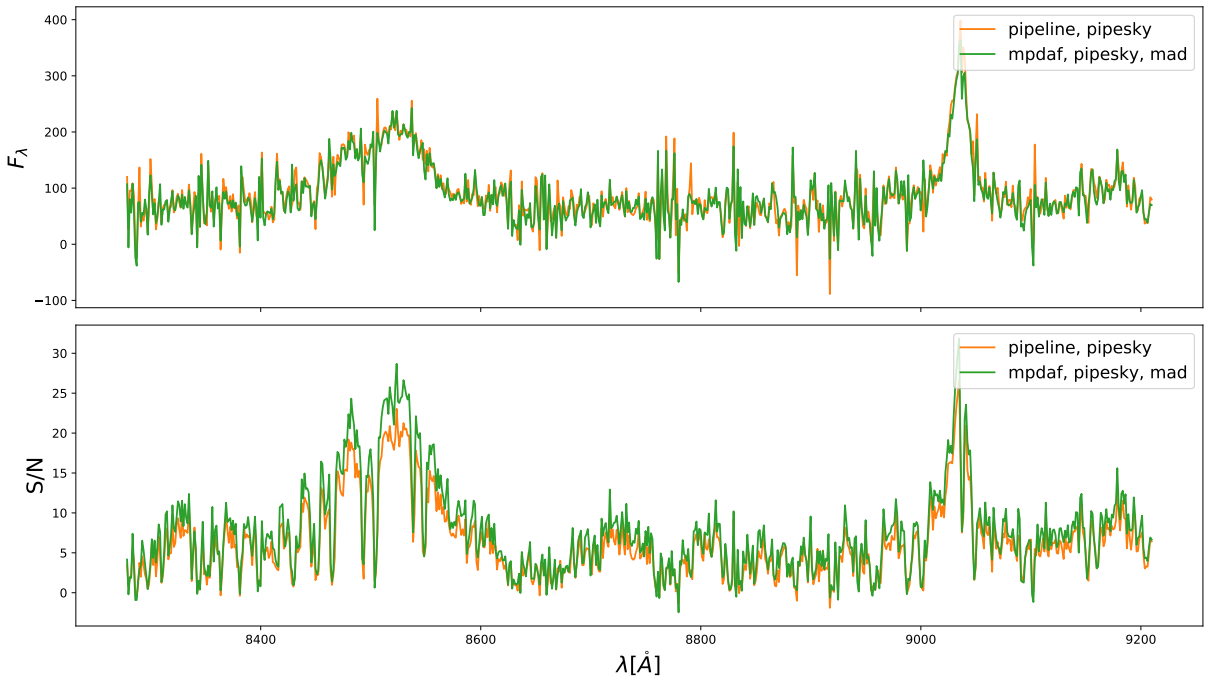

Figure B.16: The spectra and corresponding S/N from CUBEs 6th and 8th comparison in band 4.

Bibliography

Anderson M. E., Churazov E., Bregman J. N., 2016, MNRAS, 455, 227

Arrigoni Battaia F., Prochaska J. X., Hennawi J. F., Obreja A., Buck T., Cantalupo S., Dutton A. A., Macciò A. V., 2018, MNRAS, 473, 3907

Arrigoni Battaia F., Hennawi J. F., Prochaska J. X., Oñorbe J., Farina E. P., Cantalupo S., Lusso E., 2019, MNRAS, 482, 3162

Bacon R., et al., 2010, The MUSE second-generation VLT instrument. p. 773508, doi:10.1117/12.856027

Bacon R., et al., 2014, The Messenger, 157, 13

Behroozi P. S., Conroy C., Wechsler R. H., 2010, ApJ, 717, 379

Bertin E., Arnouts S., 1996, A&AS, 117, 393

Binette L., Kurk J. D., Villar-Martín M., Röttgering H. J. A., 2000, A&A, 356, 23

Binette L., Wilman R. J., Villar-Martín M., Fosbury R. A. E., Jarvis M. J., Röttgering H. J. A., 2006, A&A, 459, 31

Bolmer J., et al., 2019, A&A, 623, A43

Bond J. R., Kofman L., Pogosyan D., 1996, Nature, 380, 603

Bonnet H., et al., 2004, The Messenger, 117, 17

Bowen D. V., Chelouche D., Jenkins E. B., Tripp T. M., Pettini M., York D. G., Frye B. L., 2016, ApJ, 826, 50

Burchett J. N., Rubin K. H. R., Prochaska J. X., Coil A. L., Rickards Vaught R., Hennawi J. F., 2020, arXiv e-prints, p. arXiv:2005.03017

Cantalupo S., Lilly S. J., Haehnelt M. G., 2012, MNRAS, 425, 1992

Cantalupo S., Arrigoni-Battaia F., Prochaska J. X., Hennawi J. F., Madau P., 2014, Nature, 506, 63

Cappellari M., Copin Y., 2003, MNRAS, 342, 345

Conselice C. J., 2014, ARA&A, 52, 291

D'Odorico S., Cristiani S., Dekker H., Hill V., Kaufer A., Kim T., Primas F., 2000, Performance of UVES, the echelle spectrograph for the ESO VLT and highlights of the first observations of stars and quasars. pp 121–130, doi:10.1117/12.390133

De Breuck C., Röttgering H., Miley G., van Breugel W., Best P., 2000, A&A, 362, 519

De Breuck C., van Breugel W., Stanford S. A., Röttgering H., Miley G., Stern D., 2002, AJ, 123, 637

De Breuck C., et al., 2010, ApJ, 725, 36

Dekker H., D'Odorico S., Kaufer A., Delabre B., Kotzlowski H., 2000, Design, construction, and performance of UVES, the echelle spectrograph for the UT2 Kueyen Telescope at the ESO Paranal Observatory. pp 534–545, doi:10.1117/12.395512

Drouart G., et al., 2014, A&A, 566, A53

Eisenhauer F., et al., 2003, SINFONI - Integral field spectroscopy at 50 milli-arcsecond resolution with the ESO VLT. pp 1548–1561, doi:10.1117/12.459468

Emonts B. H. C., et al., 2016, Science, 354, 1128

Emonts B. H. C., et al., 2018, MNRAS, 477, L60

Fanaroff B. L., Riley J. M., 1974, MNRAS, 167, 31P

Foreman-Mackey D., Hogg D. W., Lang D., Goodman J., 2013, PASP, 125, 306

Gaia Collaboration et al., 2016, A&A, 595, A1

Gaia Collaboration et al., 2018, A&A, 616, A1

Goss W. M., Parijskij Y. N., Soboleva N. S., Temirova A. V., Vitkovskij V. V., Zhelenkova O. P., Naugol'Naya M. N., 1992, Azh, 69, 673

Gower J. F. R., Scott P. F., Wills D., 1967, Mem. RAS, 71, 49

Gullberg B., et al., 2016a, A&A, 586, A124

Gullberg B., et al., 2016b, A&A, 591, A73

Heckman T. M., Lehnert M. D., van Breugel W., Miley G. K., 1991a, ApJ, 370, 78

Heckman T. M., Lehnert M. D., Miley G. K., van Breugel W., 1991b, ApJ, 381, 373

Heckman T. M., Alexandroff R. M., Borthakur S., Overzier R., Leitherer C., 2015, ApJ, 809, 147

Humphrey A., Villar-Martín M., Fosbury R., Vernet J., di Serego Alighieri S., 2006, MNRAS, 369, 1103

Humphrey A., Villar-Martín M., Fosbury R., Binette L., Vernet J., De Breuck C., di Serego Alighieri S., 2007, MNRAS, 375, 705

Humphrey A., Villar-Martín M., Vernet J., Fosbury R., di Serego Alighieri S., Binette L., 2008a, MNRAS, 383, 11

Humphrey A., et al., 2008b, MNRAS, 390, 1505

Humphrey A., Binette L., Villar-Martín M., Aretxaga I., Papaderos P., 2013a, MNRAS, 428, 563

Humphrey A., Vernet J., Villar-Martín M., di Serego Alighieri S., Fosbury R. A. E., Cimatti A., 2013b, ApJ, 768, L3

Jarvis M. J., Wilman R. J., Röttgering H. J. A., Binette L., 2003, MNRAS, 338, 263

Joye W. A., Mandel E., 2003, New Features of SAOImage DS9. p. 489

Kolwa S., et al., 2019, A&A, 625, A102

Kopylov A. I., Goss W. M., Pariĭskiĭ Y. N., Soboleva N. S., Verkhodanov O. V., Temirova A. V., Zhelenkova O. P., 2006, Astronomy Letters, 32, 433

Kormendy J., Ho L. C., 2013, ARA&A, 51, 511

Krogager J.-K., 2018, VoigtFit: Absorption line fitting for Voigt profiles (ascl:1811.016)

Madau P., Dickinson M., 2014, ARA&A, 52, 415

McCarthy P. J., 1993, ARA&A, 31, 639

Miley G., 1980, ARA&A, 18, 165

Miley G., De Breuck C., 2008, A&ARv, 15, 67

Mills B. Y., Slee O. B., Hill E. R., 1958, Australian Journal of Physics, 11, 360

Minkowski R., 1960, ApJ, 132, 908

Mo H., van den Bosch F. C., White S., 2010, Galaxy Formation and Evolution

Mullaney J. R., Alexander D. M., Fine S., Goulding A. D., Harrison C. M., Hickox R. C., 2013, MNRAS, 433, 622

Nesvadba N. P. H., Lehnert M. D., Eisenhauer F., Gilbert A., Tecza M., Abuter R., 2006, ApJ, 650, 693

Nesvadba N. P. H., De Breuck C., Lehnert M. D., Best P. N., Collet C., 2017, A&A, 599, A123

Newville M., Stensitzki T., Allen D. B., Rawlik M., Ingargiola A., Nelson A., 2016, Lmfit: Non-Linear Least-Square Minimization and Curve-Fitting for Python (ascl:1606.014)

Oppenheimer B. D., Davé R., Kereš D., Fardal M., Katz N., Kollmeier J. A., Weinberg D. H., 2010, MNRAS, 406, 2325

Oppenheimer B. D., Schaye J., Crain R. A., Werk J. K., Richings A. J., 2018, MNRAS, 481, 835

Parijskij Y. N., Goss W. M., Kopylov A. I., Soboleva N. S., Temirova N. S., Verkhodanov O. V., Zhelenkova O. P., Naugolnaya M. N., 1996, Bulletin of the Special Astrophysics Observatory, 40, 5

Parijskij Y. N., Goss W. M., Kopylov A. I., Soboleva N. S., Temirova A. V., Verkhodanov O. V., Zhelenkova O. P., 2000, Astronomical and Astrophysical Transactions, 19, 297

Parijskij Y. N., Zhelenkova O. P., Thomasson P., Kopylov A. I., Temirova A. V., Sokolov I. V., Komarova V. N., Bravo Calle O. J. A., 2013, in Castro-Tirado A. J., Gorosabel J., Park I. H., eds, EAS Publications Series Vol. 61, EAS Publications Series. pp 439–442, doi:10.1051/eas/1361071

Parijskij Y. N., et al., 2014, MNRAS, 439, 2314

Peek J. E. G., Ménard B., Corrales L., 2015, ApJ, 813, 7

Peeples M. S., Werk J. K., Tumlinson J., Oppenheimer B. D., Prochaska J. X., Katz N., Weinberg D. H., 2014, ApJ, 786, 54

Perna M., Cresci G., Brusa M., Lanzuisi G., Concas A., Mainieri V., Mannucci F., Marconi A., 2019, A&A, 623, A171

Reuland M., et al., 2003, ApJ, 592, 755

Reuland M., et al., 2007, AJ, 133, 2607

Rottgering H. J. A., Hunstead R. W., Miley G. K., van Ojik R., Wieringa M. H., 1995, MNRAS, 277, 389

Rubin K. H. R., Hennawi J. F., Prochaska J. X., Simcoe R. A., Myers A., Lau M. W., 2015, ApJ, 808, 38

Sánchez S. F., Humphrey A., 2009, A&A, 495, 471

Schiminovich D., et al., 2010, MNRAS, 408, 919

Silk J., Mamon G. A., 2012, Research in Astronomy and Astrophysics, 12, 917

Silva M., et al., 2018, MNRAS, 474, 3649

Soto K. T., Lilly S. J., Bacon R., Richard J., Conseil S., 2016, MNRAS, 458, 3210

Steidel C. C., Erb D. K., Shapley A. E., Pettini M., Reddy N., Bogosavljević M., Rudie G. C., Rakic O., 2010, ApJ, 717, 289

Swinbank A. M., et al., 2015, MNRAS, 449, 1298

Tepper-García T., 2006, MNRAS, 369, 2025

Tumlinson J., Peeples M. S., Werk J. K., 2017, ARA&A, 55, 389

Umehata H., et al., 2019, Science, 366, 97

Van Ojik R., Roettgering H. J. A., Miley G. K., Hunstead R. W., 1997, A&A, 317, 358

Vernet J., Fosbury R. A. E., Villar-Martín M., Cohen M. H., Cimatti A., di Serego Alighieri S., Goodrich R. W., 2001, A&A, 366, 7

Vernet J., et al., 2017, A&A, 602, L6

Villar-Martín M., Vernet J., di Serego Alighieri S., Fosbury R., Humphrey A., Pentericci L., 2003, MNRAS, 346, 273

Villar-Martín M., Humphrey A., De Breuck C., Fosbury R., Binette L., Vernet J., 2007, MNRAS, 375, 1299

Virtanen P., et al., 2019, arXiv e-prints, p. arXiv:1907.10121

Weilbacher P. M., Streicher O., Urrutia T., Jarno A., Pécontal-Rousset A., Bacon R., Böhm P., 2012, Design and capabilities of the MUSE data reduction software and pipeline. p. 84510B, doi:10.1117/12.925114

Weilbacher P. M., Streicher O., Urrutia T., Pécontal-Rousset A., Jarno A., Bacon R., 2014, The MUSE Data Reduction Pipeline: Status after Preliminary Acceptance Europe. p. 451

Weilbacher P. M., Streicher O., Palsa R., 2016, MUSE-DRP: MUSE Data Reduction Pipeline (ascl:1610.004)

Wilman R. J., Jarvis M. J., Röttgering H. J. A., Binette L., 2004, MNRAS, 351, 1109

Wisotzki L., et al., 2018, Nature, 562, 229

Wylezalek D., et al., 2013, ApJ, 769, 79

Acknowledgement

It is not possible for me to complete this thesis work without the help and guidance from my three amazing and extremely nice supervisors at European Southern Observatory: **Dominika Wylezalek**, **Carlos De Breuck** and **Joël Vernet** whom I will continue working with in my coming PhD period. It was very lucky for me to meet Dominika at the very beginning of my Master when I decided to do a scientific project. She selflessly offered one to a foreign student who she just met only twice and introduced me to Carlos and Joël later. I could not believe this went very well. They taught me a lot of things which I will be benefit from through my career: IFU data analysing, observational proposal writing, presentation skills... They always believe in me and encourage me to explore. Last but not least, they supported me with my PhD application no matter where I will be in the future (I choose to stay after all. Who would not want to work with them on such an intriguing topic ? :). I am very grateful for the time they spent on me and our project. It is not very easy for them considering I am just a master student and they are busy with other more important works. I still have a lot to learn, but with them I am optimistic!

Big thanks to **Sthabile Kolwa** who taught me the complex procedure of MUSE data reduction and Voigt fitting. Big thanks to **Eduardo Iani** with whom I discussed a lot about the MUSE data reduction.

I also want to thank **Benjamin Moster**, my official supervisor at LMU, who also dedicated time to my thesis work and application recommendation and led me into the fascinating topic of machine learning.

I appreciate **Joseph Mohr** who agreed to be another referee of my application, despite how busy he is (who wrote the recommendation letter on a flight).

I thank the astrophysics master program at **Ludwig-Maximilians-Universität München** which gives me a lot of freedom to do the project I want.

Many thanks to **European Southern Observatory** where I worked mostly on the thesis and listened to a number of amazing talks (Maybe I should not listen to that much and work more on my project...).

I would also like to thank the people I met at ESO with who I had a lot of fun and learned many things (other than science): Jens, JP, Avinash, Aish, Roland, Kshama...

Support from family is always the sweetest thing one can seek for during a hard period. It was not easy for me to live and study abroad over 10,000 km from home. I could not say more to express my feelings of my wife, **Qing Xia** (夏青), who abandoned the cosy life at home and worked hard on the complicated visa application process to reunite with me. She always believes in me especially during the time I doubted myself. She tries very hard to keep our lives cheerful, e.g. coming up with different ideas for dinner and planning amazing trips. Especially in the end of my master study when the whole world encountered the coronavirus pandemic which is still far from recovery, it is the accompany of Qing which makes the time of quarantine less miserable. I consider myself very lucky to have a wife like you when we are still young!

Last but not least, I want to thank my parents who let me pursue what I want in the first place and support (in any aspects) me through all the years.